TECHNISCHE UNIVERSITÄT WIEN
Vienna University of Technology

DISSERTATION

Simulation of the synaptic exocytosis of bipolar cells in the electrically stimulated mammalian retina

Ausgeführt zum Zwecke der Erlangung des akademischen Grades eines Doktors der technischen Wissenschaften

unter der Leitung von
Prof. DDDr. Frank Rattay
Institut für Analysis und Scientific Computing (E101)

eingereicht an der Technischen Universität Wien
Fakultät für Mathematik und Geoinformation

von
Hassan Bassereh Moosaabadi
Matrikelnummer: 1633395
Lorystrasse 89/5/14, 1110 Wien

April 2019

Acknowledgements

First of all, I would like to thank Professor Frank Rattay for accepting to be my supervisor and his patient guidance. Professor Maarten Kamermans from Netherlands Institute for Neuroscience has been a precious mentor and we discussed a lot about synchronizations in AII amacrine cells during my visit from his group. I sincerely thank Dr. Günther Zeck from University of Tübingen for letting me the chance visit his group and earn more experience in exteracellular stimulations.I also thank Professor Thomas Euler both for his nice comments regarding my Ph.D thesis and his favor to let me the chance visit his group.

I would also like to thank my former labmate Paul Werginz for sharing his expertise with me and teaching me the multi compartment model.

I would like to express gratitude to the Marie Sklodowska-Curie Actions for financial support of this project.

At the end, I thank my parents for all of their supports.

Abstract

The coming optic light to the eye reaches to the retina after passing from cornea, pupil, lens and vitreous body. Retina is made of photoreceptors, horizontal cells, bipolar cells, amacrine cells and ganglion cells. The light is absorbed by photoreceptors and after modulations by horizontal, amacrine, and bipolar cells, it is finally transferred to the brain via spikes generated at the ganglion cells. In patients suffering from 'retinitis pigmentosa' and 'age-related macular degeneration', around 80 percent of retinal neurons are fairly undamaged except for photoreceptors. Lack of photoreceptors can slightly be compensated by retinal implants. Retinal implants stimulate the retina via an array of microelectrodes.

Moving a microelectrode along the axon of a ganglion and a cortical pyramidal cell enables spike generation for every position and polarity. However, for a spiking bipolar cells this rule is not true and some positions need cathodic pulses and some positions need anodic pulses. There is only a small region for electrode position where extracellular cathodic stimulation generates direct spike initiation in the sodium channel band of the bipolar cell. For all other positions, a sodium spike can only be generated via high membrane voltage at terminals.

Simple models such as single and two compartments are known from literature. We tested accuracy of such models in comparison with results obtained by multi compartment modeling (real morphology) for intra- and extracellular stimulation. Intracellular stimulation is close to natural stimulation of bipolar cells via photoreceptors, and extracellular stimulation is used in retinal implants. Multi compartment method is actually a system of coupled ordinary differential equations. Solving the system leads to find the transmembrane voltage of any arbitrary compartment. Although both single and two compartment models are accurate enough for intracellular stimulation when the cell has a passive membrane (no sodium channel is included), neither single nor two compartment model is able to explain the cell's behavior with active membrane (sodium channels are included). To overcome this problem, we presented a new simple model made of the four compartments dendrite, soma, axon, and terminal. Four compartment model highly improves the deficiencies of single and two compartment models

especially for the case of intracellular stimulation and recording from the soma which is very common in electrophysiological experiments. In extracellular stimulations for both passive and active membranes, neither two compartment nor four compartment model is able to reproduce the transmembrane voltages correctly. Investigations on position of sodium channels on transmembrane voltages for both intra- and extracellular stimulations showed that location of ion channels highly affect the transmembrane voltages of the cell and is also needed to be considered.

The output of the retinal bipolar neurons has two components, i.e., transient and sustained neurotransmitter releases, which is not common at chemical synapses. This uniqueness originates from an extra protein structure called 'ribbon'. Transient outputs take place exactly after a large enough stimulus, while sustained outputs occur at any state with a different rate. We presented two models to simulate both releases from a terminal of a rat rod bipolar cell, but the approach can be applied for any type of bipolar cells. One of the models is based on transmembrane voltage of terminals and the other is based on intracellular calcium concentration of terminals, each of which is explained by two time dependent equations. Intracellular calcium concentration method bring a 0.43 ms signal delay observable in experiments, while the other model has no delay. By comparing responses of spiking and non-spiking bipolar cells stimulated intracellularly, it was proposed that a spike causes the release of all of the available vesicles rapidly (transient releases), while the non-spiking cell release no vesicle at the same stimulus amplitude. Effect of extracellular stimulation generated by a single microelectrode, on transient release almost suggested no difference between responses of active and passive cells in short pulses because terminal membrane of the cells in both cases senses the same potentials originating from the microelectrode. However, spiking-bipolar cells release more transient vesicles in pulses with long duration since spike has enough time to reach to the terminal leading to release of more transient vesicles. Effect of periodic stimulation on ribbon recovery when the cell is stimulated both intra- or extracellularly also suggested that for 5 Hz stimulations, only three transient vesicles are released from a single ribbon per stimulus.

Zusammenfassung

Ins Auge einfallendes Licht gelangt durch die Hornhaut, die Pupille, die Linse und des Glaskörpers auf die Retina. Die Retina besteht aus Fotorezeptoren, horizontalen Zellen, bipolaren Zellen, Amakrinzellen und Ganglienzellen. Das Licht wird von den Fotorezeptoren absorbiert, anschliessend von horizontalen Zellen, Amakrinzellen und bipolaren Zellen moduliert, und schliesslich über in den Ganglienzellen erzeugte Aktionspotentiale in das Gehirn übertragen. Bei Patienten, die an 'Retinitis pigmentosa' und einer 'altersbedingten Makuladegeneration' leiden, sind rund 80 Prozent der retinalen Neuronen mit Ausnahme der Fotorezeptoren unbeschädigt. In diesem Fall können Retina Implantate die fehlende Funktion der Fotorezeptoren übernehmen indem die Netzhaut mittels eines Mikroelektroden-Array elektrisch stimuliert wird.

Sowohl für eine Ganglienzelle als auch für eine Pyramidenzelle kann entlang der Achse des Axons mit einer Mikroelektrode an jeder Position mit beliebiger Polarität ein Aktionspotential ausgelöst werden. Für bipolare Zellen gilt diese Regel jedoch nicht, die Polarität des Stimulus um erfolgreich einen Natrium-Spike auszulösen ist stark abhängig von der Position der Mikroelektrode. Es gibt nur einen kleinen Bereich für die Elektrode, in dem eine extrazelluläre kathodische Stimulation eine direkte Spike-Initiierung im Natriumband der bipolaren Zelle auslöst. Bei allen anderen Positionen kann ein Natrium-Spike nur über eine hohe Membranspannung an den Terminals der Zelle generiert werden.

Bekannte Einfache Modellansätze, die bilden die Zelle mittels einem oder zwei Kompartments abbilden sind in der Literatur zu finden. Wir testeten die Genauigkeit solcher Modelle hinsichtlich intra- und extrazellulärer Stimulation im Vergleich zu Multi-Kompartment-Ansätzen, welche auch die Morphologie der Zelle berücksichtigen. Eine intrazelluläre Stimulation kommt der natürlichen Stimulation bipolarer Zellen über Fotorezeptoren sehr nahe, während eine extrazelluläre Stimulation die Funktionsweise von Retina Implantaten simuliert. Ein Multi-Kompartment-Modell besteht aus miteinander gekoppelten Differentialgleichungen, die es erlauben das die Membranpotential Membranspannungl eines beliebigen Kompartments zu ermitteln. Modelle mit nur einem oder zwei Kompartments sind zwar in der Lage die intrazelluläre Stimulation

einer passiven Zellmembran (Membran ohne Natriumkanäle) relativ genau abzubilden, allerdings können diese Modelle das Verhalten der Zelle mit aktiver Membran (Natriumkanäle sind enthalten) nicht reproduzieren.

Um dieses Problem zu lösen, haben wir ein neues Modell vorgestellt, das aus vier Kompartments (Dendrit, Soma, Axon und Terminal) besteht. Das Vier-Kompartment-Modell ist in der Lage etliche Defizite von Ein- und Zwei-Kompartment-Modellen zu bereinigen, insbesondere können damit Ergebnisse von elektrophysiologischen Versuchen, bei denen das Soma einer Zelle intrazellulär stimuliert wird, nachvollzogen werden. Bei extrazellulären Stimulationen können weder das Zwei- noch das Vier-Kompartment-Modell das die Membranpotential Membranspannung korrekt reproduzieren, weder für passive noch für aktive Zellmembranen. Untersuchungen zeigten, dass die entsprechende Verteilung von Ionenkanälen das die Membranpotential Membranspannung der Zelle stark beeinflusst, sowohl bei intra- als auch extrazellulären Stimulation. Daher muss die Ionenkanalverteilung entlang der Membran berücksichtigt werden.

Im Gegensatz zu anderen chemischen Synapsen setzt sich die Neurotransmitter-Ausschüttung in retinalen bipolaren Zellen aus zwei Komponenten zusammen: eine transiente und eine anhaltende. Diese Einzigartigkeit beruht auf einer zusätzlichen bandartigen Proteinstruktur die als "Ribbon" bezeichnet wird. Eine transiente Freisetzung von Neurotransmittern findet nach einem ausreichend grossen Stimulus statt, während die anhaltende Freisetzung unabhängig vom Status der Zelle mit unterschiedlicher Rate erfolgt. Wir haben zwei Modelle vorgestellt, welche die Neurotransmitter Freisetzung am Terminal einer Stäbchen-gesteuerten Bipolarzelle (einer Ratte) simulieren, dieser Ansatz kann jedoch für jeden Typ von Bipolarzellen angewendet werden.

Eines der Modelle basiert auf der Membranspannung an den Terminals, das andere auf den intrazellulären Kalzium Konzentrationen in den Terminals, welche durch zwei zeitabhängige Gleichungen definiert werden. Das kalziumbasierte Modell zeigt eine Signalverzögerung von 0.43 ms welche experimentell beobachtet wurde, während das spannungsbasierte Modell keine solche Verzögerung aufweist. Durch den Vergleich der Reaktionen intrazellulär stimulierter "spiking" und "non-spiking" bipolarer Zellen wird angenommen, dass ein Spike die schnelle Freisetzung aller verfügbaren Vesikel bewirkt (transiente Freisetzung), während bei "non-spiking" Zellen bei identischer Stimulus Amplitude keinerlei Vesikel freisetzt werden.

Das Antwortverhalten von aktiven und passiven bipolaren Zellen auf einen kurzen extrazellulären Stimulus von einer Mikroelektrode zeigt kaum Unterschiede in der transienten Vesikel Freisetzung da das die Membranpotential Membranspannung an den Terminals ausschliesslich von der Elektrode selbst bestimmt ist. Bei einem längeren Stimulus hingegen werden mehr transiente Vesikel freigesetzt, da der Spike genug Zeit hat, um das Terminal zu erreichen. Die Simulation mit einem periodischen 5 Hz Stimulus legt nahe, dass jeweils drei transiente Vesikel pro Stimulus freigesetzt werden. Dies konnte sowohl intra- auch als extrazellulär beobachtet werden.

Contents

List of abbreviations

AIS	Axon initial segment
BC	Bipolar cell
CP	Cytoplasmic pool
EPSC	Excitatory postsynaptic current
FCM	Fout compartment model
GC	Ganglion cell
GCL	Ganglion cell layer
HCN channels	Hyperpolarization-activated cyclic nucleotide-gated channels
HH	Hodgkin-Huxley
INL	Inner nuclear layer
IPL	Inner plexiform layer
LGN	Lateral geniculate nucleus
LTE	Local truncation error
MCM	Multi compartment model
ODE	Ordinary differential equation
ONL	Outer nuclear layer
OPL	Outer plexiform layer
PR	Photoreceptors
RBC	Rod bipolar cell
RP	Releasable pool
RRP	Readily releasable pool
SCM	Single compartment model
TCM	Two compartment model

Chapter 1

Introduction

1.1 Motivation & background

In the world, around 39 million people suffer from retinal degenerative diseases (Shepherd et al., 2013). The diseases include retinitis pigmentosa, age-related macular degeneration, or even accidents and injuries. Although retinitis pigmentosa is a genetic disorder and age-related macular degeneration is a problem of aging, both of them are of special interests for scientists since in addition to all of physical restrictions, lack of vision ability may cause many psychological disorders such as depression, social isolation, or even may lead to suicide.

Age-related macular degeneration can be prevented by annual check up or even treated in rare cases, but retinitis pigmentosa is so challenging since it affects the neural network of the retina. PRs are the main targets in both of these disorders and different approaches are used to overcome to the diseases such as stem cell transplants, microfabricated PR arrays, and an implantable electronic microsystem. In stem cell transplants, stem cells are used to reconstruct the damaged cells (Ramsden et al., 2013; Chader et al., 2016). Stem cells are able to differentiate into any cell. In microfabricated PR arrays methods, engineered living tissues are used to be replaced with damaged parts of the retina (Chen et al., 2009). Although both of the methods were somehow useful, they need more progress as they are in the starting level of their progress. Another treat method that is highly of interest is implantable electronic microsystem also referred to

the visual prostheses. In this method, the environment is observed by some small cameras and the extracted information analysis by a small micro processor. Then, an electric current is injected to several microelectrodes located in the vicinity of the retina that results in stimulating the retina electrically. Although this method is also at the initial steps, it seems it is helpful since using of the natural visual pathway.

The first usage of electrically stimulation of the human visual systems comes back to the 18th century. In 1755, Le Roy produced visual sensations of light by passing an electrical charge through the eye of a blind man (Le Roy et al., 1755). Afterward, Foerster used electrical stimulation to stimulate visual cortex of the blind (Foerster et al., 1929). Electrically stimulation of the retina was done in the beginning of the present century (Prochazka et al., 2001; Isaacson et al., 2003).

The mentioned biological approaches to restore vision are mainly in the laboratory levels, but stimulation of the visual system via electrodes is the only clinical option. Although this method is also in the first steps, it could produce functional vision for many patients all over the world suffering from blindness (Barnes et al., 2016; da Cruz et al., 2016). In addition to retina, other parts of the vision system can be stimulated, which may lead to vision, such as visual cortex (Lewis et al., 2016), optic nerve (Lane et al., 2016), lateral geniculate nucleus (Nguyen et al., 2016). None of these methods is as good as retina stimulation due to two main reasons: i) the surgical risks associated with the implantation of the electrodes at the retina are strikingly lower than to other visual neurostimulators (Weiland et al., 2005), ii) retinal prosthesis use the natural vision systems, from retina, whether LGN to visual cortex, while other methods losses at least one part.

In addition to tremendous progress in retinal implants in the last two decades, there are many improve-needed aspects to make the prosthesis with higher quality. These aspects include biocompatibility, nano-fabrication of small stimulating electrodes, development of extra-ocular camera systems and surgical procedures, but the main aspect would be the way by which the retina is simulated, from intensity to shape and frequency of the stimulus. In this study, simulation of

spiking and non-spiking BCs have been investigated that may be helpful for the future road map of retinal implants.

1.2 Retina

Retina is part of the central nervous system located behind of the eyeball. Retina consists of two main parts: pigment epithelium and neural part. Pigment epithelium, which is the pigmented cells layer located between PRs and choroid, absorbs the light passed from the PRs. This task is supposed to reduce light scatter and image distortion within the eye. Pigment epithelium also feeds the retinal neurons. Neural part of the retina is made of five layers containing five types of neurons: PRs, horizontal cells, BCs, amacrine cells, and GCs 1.1. The five layers are:

- ONL, consists of PR cell bodies.
- OPL, consists of PRs, BCs and horizontal cells synapse.
- INL, consists of horizontal cell, BC, and amacrine cell bodies.
- IPL, consists of the BCs, amacrine, and GCs synapse.
- GCL, contains the retinal GCs body.

1.2.1 The photoreceptors

The light coming to the eye reaches finally to the light sensitive part of the PRs, after passing through the cornea, lens, vitreous, and different retinal layers. PRs transduce the light energy into electrical signals and send them through chemical signals to the bipolar and horizontal cells. PRs are divided into two types, rods and cones.

The human retina contains of around 130 million rods that are twenty times more than cones with 6 million population (Osterberg et al., 1935). Rods are more sensitive than cones. This feature makes them suitable for detection of tiny light intensity or scotopic vision. Cones are mostly located in the center of the

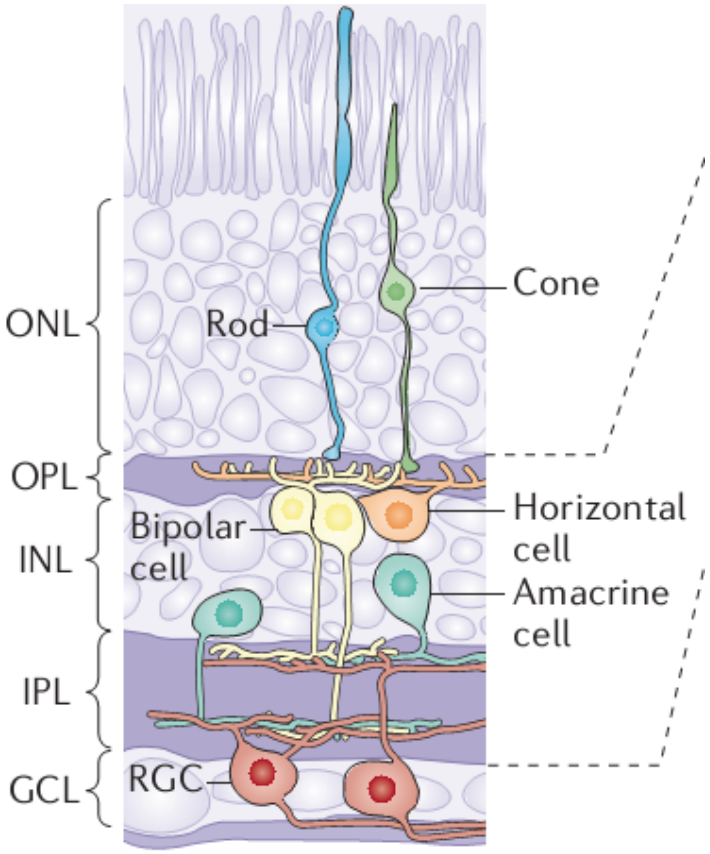

Figure 1.1: **Different layers of retina and involved neurons.** PRs make synapse with bipolar and horizontal cells in the OPL. BCs make synapse with amacrine and GCs in the IPL. PR and GC bodies are respectively in the ONL and GCL. Cell bodies of all bipolar, amacrine, and horizontal cells are on the INL. (picture taken from: Euler et al., 2014).

fovea and responsible for photonic vision, vision on daylight. Cones are actually responsible for perception of shapes and colors.

Opsins are a group of proteins existing on rods and cones and make them light-sensitive. In addition to geometrical differences between rods and cones, the main difference is the opsin configuration of photopigment. Cones themselves have three different opsins leading to response to light with different wavelengths. Blue, green, and red cones respond to light spectrum with respectively maximum wavelength of 420, 530, and 560 nm.

1.2.2 The horizontal cells

Horizontal cells are smaller in number compared to other retinal neurons. Horizontal cells communicate with PRs in both presynaptic and postsynaptic formalism in the OPL. Role of the horizontal cells is to create a sharp image and to maintain a contrast under different illumination condition by modulating the synaptic activity of PRs.

There are typically one, two or three types of horizontal cells in the retina depending on the species (Demb and Singer, 2015). Horizontal cells also make synapses with BCs.

1.2.3 The bipolar cells

Retinal BCs are stimulated through synapses via PRs. Although PRs release only one type of neurotransmitter; glutamate (Ayoub and Copenhagen, 1991), distinct BC types respond differently to the same stimulus. According to their response, BCs are divided into two groups; OFF BCs, the cells that respond to glutamate by depolarization, and ON BCs, the cells that respond to glutamate by hyperpolarization, Fig 1.2. These different responses are because of different postsynaptic glutamate receptor proteins existing mainly on the dendrite of the BCs. In addition to neurotransmitter receptors, ON and OFF BCs differ in other aspects, including cytoskeletal architecture of the cone pedicle, expression of different voltage-gated ion channels, and morphological (geometrical) features. As the main topics of this thesis turn around BCs, each of the terms above will be explained shortly.

- **Neurotransmitter receptors**

  In OFF BCs, the receptors are ionotropic (iGluR), also known as transmitter-gated ion channels, while in ON BCs, they are metabotropic glutamate receptors (mGluR6), also called G-coupled-protein receptors. Metabotropic receptors have also been detected on the axon terminals of PRs (Hirasawa et al., 2002) where they play role of autoreceptors by regulating glutamate release. The role of metabotropic receptors is closing the cation-permeable

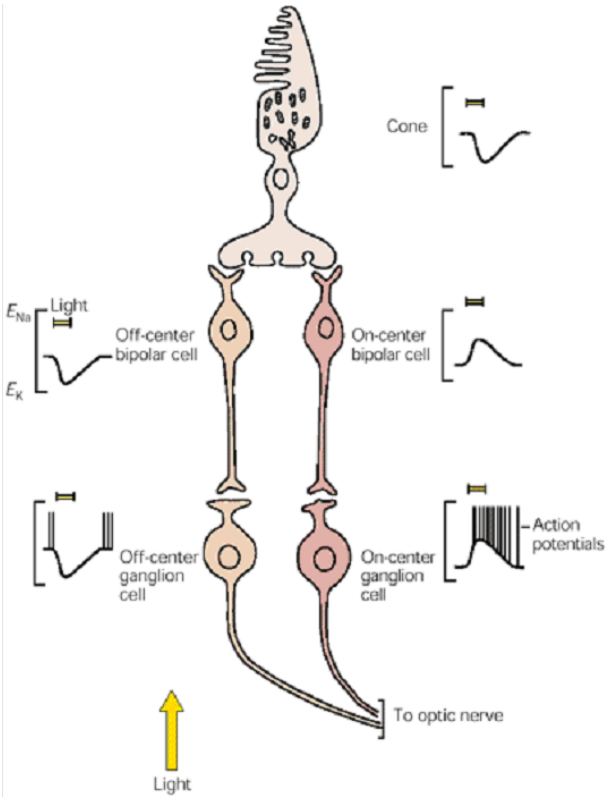

Figure 1.2: **Schematic diagram of the parallel ON and OFF pathways in the retina and related membrane potentials.** Light hyperpolarizes cones. A sign-conserving (+) synaptic connection causes OFF-type BCs to hyperpolarize when light is on, while a sign-inverting (-) synapse from cones makes the ON-type BC depolarized at the same time. (Image adapted from (Tessier-Lavigne 2000)).

channels such as TRPM1 (transient receptor potential cation channel subfamily M member 1) through an intracellular cascade (Koike et al., 2010), while ionotropic receptors directly form an ion channel (Popova, 2014, see also; Pang et al., 2012).

Different types of OFF BCs contain two sorts of ionotropic glutamate receptor, which are AMPA receptors, kainate receptors or both (Regus-Leidig and Brandstatter, 2012), while only one type of glutamate receptor, mGluR6, was found on all types of ON BCs (Masu et al., 1995). Despite expressing the same receptors, different dendritic signal kinetics on ON BCs (Ichinose et al., 2014) can arise because of varying the components of the second-

messenger cascade (Cao et al., 2012; Pearring et al., 2011). Other molecular factors that are responsible to manipulate the kinetics of dendritic signaling in ON BCs, and may differentially exist on different types of ON BCs, are voltage-gated calcium channels (De Sevilla Müller et al., 2013), potassium channels (Sulaiman et al., 2013), protein kinase $C\alpha$ (PKC) (Rampino and Nawy, 2011).

- **Cytoskeletal architecture of the cone pedicle**

  Another factor that results in differences between ON and OFF BCs is the cytoskeletal architecture of the cone pedicle (Haverkamp et al., 2001), which can lead to various spatial glutamate release that is detected by BC dendrites and affect the BC inputs (Behrens et al., 2016). From this point of view, dendrites of the ON BCs are directly opposite to the active zone of the PRs; so-called invaginating synaptic contact (Haverkamp et al., 2000), while in OFF BCs, dendrites contact to the base of the cone pedicle, so-called flat contact. This geometrical feature of OFF BCs leads to increment of distance that should be passed by glutamate from the active zones in PRs to the dendritic glutamate receptors in OFF BCs that represents a delay low-pass filter (DeVries et al., 2006).

- **Different expression of ion channels**

  L-type calcium channels, mainly $Ca_v1.4$ type (Oltedal et al., 2007), are included in terminals of both ON and OFF BCs that play a vital role in neurotransmitter release (Baden et al., 2013b). Other types of calcium channels have also been reported on BCs such as T-type, also known as $Ca_v3.x$, that are not necessarily expressed in the BC terminals (Puthussery et al., 2013). In addition to calcium channels, some of BCs in both ON and OFF categories express voltage-gated sodium channels in almost all mammals, such as mice (Baden et al., 2013a), rat (Cui and Pan 2008), monkey (Puthussery et al., 2013), ground squirrels (Saszik and DeVries, 2012), and also fish (Burrone and Lagnado, 1997; Baden et al., 2011). Although the general role of sodium channels seems to be generating all-or-none spikes, several

BC types containing sodium channels are not able to spike such as Db3b in macaque retina (Puthussery et al., 2013). Hyperpolarization-activated and cyclic nucleotide gated (HCN) channels are the other type of channels found widely in the BCs (Müller et al., 2003). It seems that HCN channels are found in all types of BCs, except for type 1 and 4, in rat (Ivanova and Müller, 2006), but no HCN channels has been found in BCs located in parvocellular pathway of macaque's retina (Puthussery et al., 2013). Voltage sensitive potassium channels have been reported in BCs varying in terms of tetraethylammonium (TEA) sensitivity: high-sensitive, low-sensitive, and resistant types (Hu and Pan, 2002; see also: Ma et al., 2003).

- **Morphological differences**

  A key difference between mammalian BCs from geometrical point of view is the axon length that is larger in ON BCs up to three times (Behrens et al., 2016). The longer axon length of ON BCs may lead to signal attenuation in the visual scene (Euler et al., 2014)

  In spite of getting depolarized or hyperpolarized through PRs, BCs are divided into two groups based on connection with PRs. If a BC receive input from rods, it is called ′ rod BC′ and so ′cone BC′ receive input from cones and rods. BCs make synapses with the amacrine and GCs in the inner plexiform layer.

1.2.4 The ganglion cells

GCs receive signals from either the BCs or amacrine cells and send trains of action potentials to the LGN through their axons . Around one million axons of GC converge to the optic nerve for further processing of visual information transferred to the visual cortex (Polyak, 1941; Quigley et al., 1982). GCs are divided into two groups of parasol (or M-type) and midget cells (or P-type) according to their sizes and dendritic branching levels (Soto et al., 2011). Parasol cells, which make about 80 percent of all GCs, are color-specific and so involved in color detection, while midget cells respond efficiently to the large objects, and

follow rapid changes in the stimulus (Kandel et al., 2000). GCs are also named ON and OFF GCs if connected respectively to ON or OFF BCs.

1.2.5 The amacrine cells

Amacrine cells are the most diverse group of neurons in the retina, their variety reaches up to 30 types based on their dendritic sizes and their stratification within the IPL (Kolb et al., 1981). Amacrine cells make synaptic contact with BCs, GCs and even themselves. Amacrine cells are movement sensitive and allow GCs to respond to a large range of light levels. Amacrine cells also modulate the rod BCs signals and send them to cone BCs as well as being responsible for interactions between ON and OFF cells, both BCs and GCs, by releasing different neurotransmitters (Masland et al., 2012).

1.3 Retinal implants

Retinal implants are neuroprosthetic devices that aim to restore vision in the blind by electrically stimulating the diseased retina. Vision can only be restored, up to 20 percent, in patients specially suffering from retinitis pigmentosa and macular degeneration. Both of which are degenerative diseases of the PRs.

- **Retinitis pigmentosa**

  Retinitis pigmentosa, which is mainly a genetic disorder, starts with degeneration of rods, so starts with night blindness. Then, the degeneration is spanned towards the macula and also affect cones leading to vision loss in the peripheral visual field, Fig 1.3, and finally to complete blindness.

- **Age-related macular degeneration**

  Age-related macular degeneration, which is usually reported in elderly people, is mostly because of atrophy of the pigment layer below the retina (dry type) or an unusual growth of blood vessels below the retina (wet type). Age-related macular degeneration affects the macula and thus leads to a loss of the central visual field, 1.3.

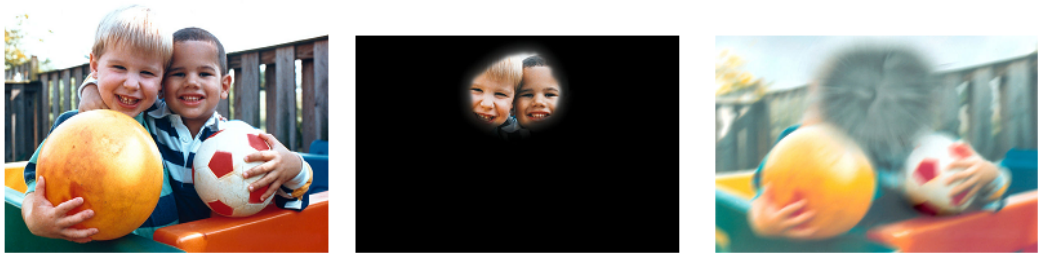

Figure 1.3: **Simulated view with different retinal diseases.** Left) Normal vision, Middle) Retinitis pigmentosa, Right) Age-related macular degeneration. (picture taken from: Simulation of Eye Disease Images. https://nei.nih.gov/health/examples).

The first implant was made by Brindley and Lewin (1968). The implant contained eighty electrodes positioned next to the visual cortex and successfully detected spots of light; phosphenes, in a totally blind patient. Although this approach or very similar approaches were selected by other groups e.g Dobelle et al. (1974), the main changes in the structure and method was made by Veraart et al. (2003) in which optic nerve was stimulated directly by stimulating of the GC axons. This method leaded to expansion of optic nerve prosthesis. The other big changes in visual prosthesis was microstimulation of the thalamus applied to generate phosphenes in monkeys (Panetsos et al., 2011). This type of stimulation called 'intercranial' stimulation. Notable feature of both type of intercranial and optic nerve stimulation was also their application on patients who lost an eye or having a damaged optic nerve. But both of these prosthesis need more sophisticated signal analysis and also have a lower efficiency in comparison to retinal implants because low-level processing of vision that is done by the retina is skipped.

There are three different types of retinal implants, i) subretinal implant, ii) suprachoroidal, iii) epiretinal, defined by position of the prosthesis, Fig 1.4.

- **Subretinal implants** are implanted between the retina and the choroid on the place of degenerated PR layer. Close vicinity to the first non-degenerative layer of retina makes these implants able to directly activate these layers and to exploit the natural neuronal circuitry. Simulation of extracellular stimulation used in this thesis represents these implants.

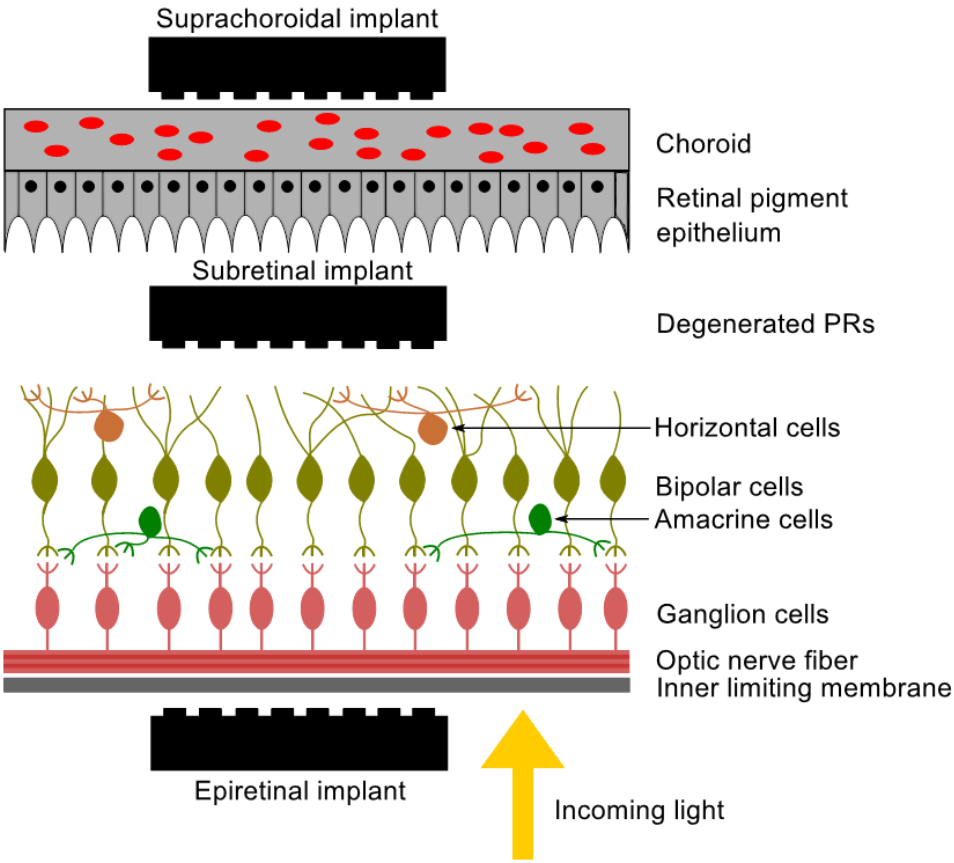

Figure 1.4: **Schematic picture of the retina with locations of different retinal implants.** A subretinal implant is positioned on the region of degenerated PRs while a suprachoroidal prosthesis is implanted between choroid and the sclera. Targets of both of which are the retinal BCs. Epiretinal implants stimulates the retina from the opposite side and the back of the eye by stimulation of GCs. (picture taken from (Werginz and Rattay, 2015)).

- **Suprachoroidal implants:** These type of implants are located out of the retina between the choroid and the sclera leading to minimize the surgical complexity. Disadvantage of these implants is longer distance to the targeted BCs in comparison to subretinal implants that causes larger population of activated neurons due to spread of stimulating electrical field that may result in limiting the spatial resolution.

- In **epiretinal implants**, the prosthesis is placed above the retina to directly stimulate the GCs in the GCL. Advantage of these implants is to provide

visual perception even if all other retinal layers have been damaged. The main disadvantage would be loosing effect of BCs.

1.4 Usual synapse versus ribbon synapse

A synapse is a place in where two or more neurons communicate. There are two types of synapses, i) electric synapse ii) chemical synapse. In electrical synapses, pre- and postsynaptic neurons are connected via a narrow channels called 'gap junctions'. The channels enable the neurons to communicate directly by passing ions and even small molecules.

Although two cells are not directly connected in chemical synapses, the presynaptic neuron uses 'neurotransmitters', i.e. endogenous chemicals, to affect the postsynaptic neuron. The effect can be excitatory or inhibitory depending on the type of neurotransmitters and the receptors located on the membrane of the postsynaptic cell. In the presynaptic terminals, neurotransmitters are in small membrane sacs called 'vesicles'. Vesicles connect to the 'active zones' regions from the internal side of the membrane. These vesicles are called 'docked vesicles'. Connection of docked vesicles to the membrane is through binding of a v-SNARE fiber from the vesicle membrane and a t-SNARE fiber of the terminal membrane (Szule et al., 2012). Size of the vesicles are almost the same, so release of one vesicle leads to a specific effect on the postsynaptic cell. This feature is interpreted as 'quantal character'. Active zones also contain many population of voltage-gated calcium channels, Fig 1.5.

In addition to usual chemical synapse, there is another type containing an extra protein structure perpendicular to the membrane called 'ribbon', Fig 1.6. These type of synapses are called 'ribbon synapses'.

In axon terminals of the cells containing ribbons, three types of vesicles exist. (i) few vesicles primed for fast release ($<$ 10 ms, Singer and Diamond, 2003) making the RRP. Docked Vesicles are in RRP. (ii) the vesicles tethered to the

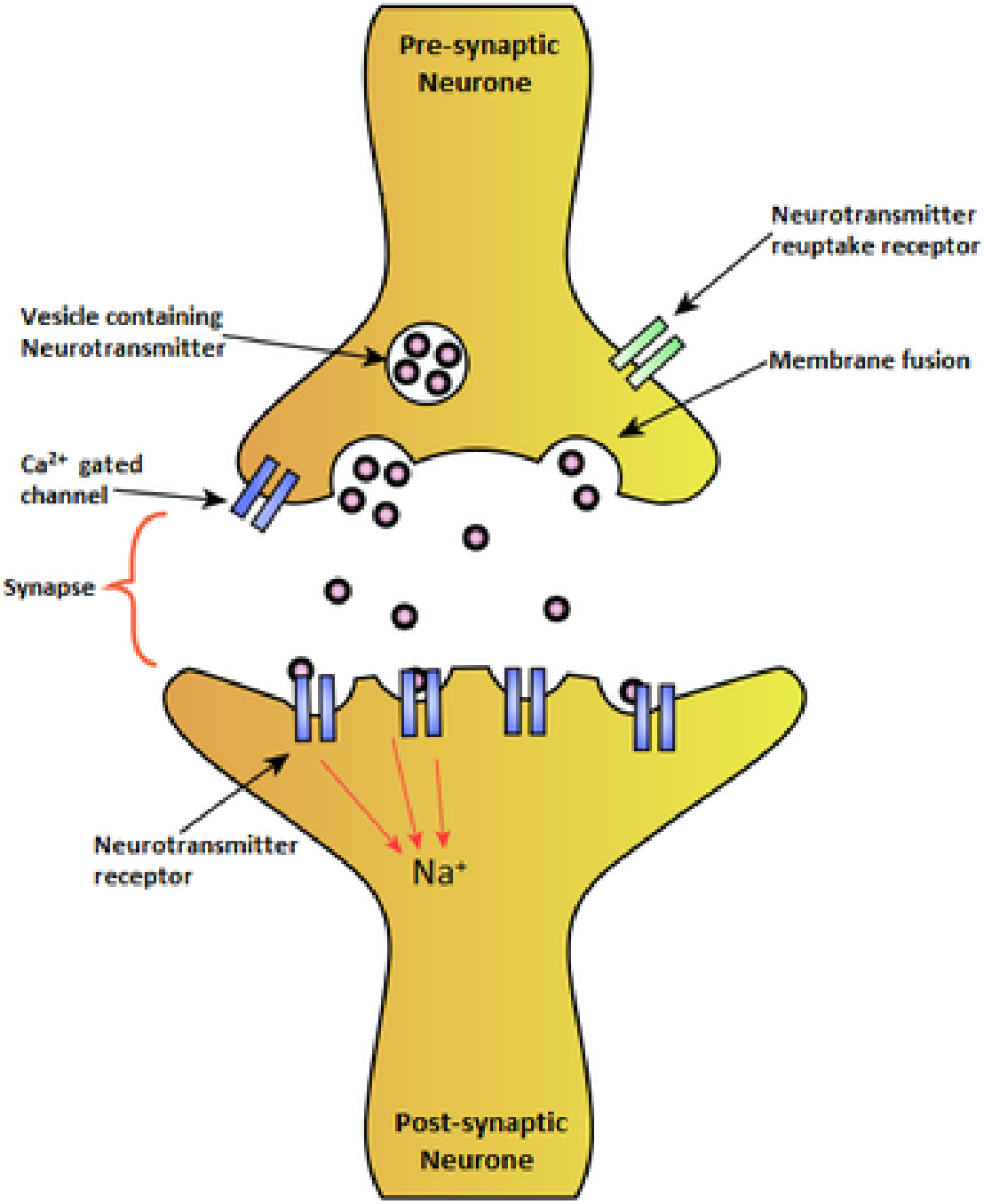

Figure 1.5: **Schematic picture of a synapse.** If any membrane depolarization arrives to the presynaptic terminal membrane, the presynaptic membrane becomes depolarized resulting in opening of the calcium channels. By opening the channels, calcium ions pass through the channels and come into the cell that leads to increase of intracellular calcium concentration. The intracellular calcium ions fuse with the vesicles leading to release content of the vesicles, neurotransmitters, into the synaptic cleft. The released neurotransmitters may make the post-synaptic cell excited or inhibited by opening different types of ion channels such as Na or K. (picture taken from https://psychonautwiki.org/wiki/Synapse).

ribbon making the RP and their population is larger than the vesicles in RRP. The RP usually becomes depleted over several hundreds of milliseconds. (iii) the freely diffusible vesicles in the terminal making the CP and their number reaches up to thousands (Sterling and Matthews, 2005). Tethered vesicles cannot leave the ribbon to be added to CP at all, but they can fill the empty places in the RRP, if any at all. When a vesicle leaves the ribbon, a vesicle from the CP is replaced (Graydon et al., 2014).

Release of docked vesicles depends on intracellular calcium concentration. Intracellular calcium concentration increases when terminal membrane depolarizes that results in opening voltage-gated calcium channels, mainly the L-types (Hartveit, 1999; Pan, 2000 and 2001), and so calcium ions would find the chance to come to the terminal. The calcium ions bind to the calcium-sensitive fiber connected to the docked vesicles, i.e. synaptotagmin, and cause neurotransmitter to release into the synaptic cleft. Depending on the time interval in which the vesicles are released, two types of vesicle release are defined. Fast vesicles release after a large depolarization of the terminal membrane is called 'transient vesicle release', which is responsible for contrast adaption (Oesch and Diamond, 2011). In case of prolonged stimulation, transient release is replaced by sustained releases with a slower rate and refers to luminance adaption in the retina (Oesch and Diamond, 2011). Continuous vesicle release from the ribbon in response to prolonged stimuli can be explained by RP dynamics (Heidelberger et al., 2005; Matthews and Fuchs, 2010). Released neurotransmitters finally bind to the receptors located on the surface of the postsynaptic cells that results in making the postsynaptic cell depolarized or hyperpolarized by opening the ion channels close to the receptors (Pan, 2001). We made a model for a single ribbon based on occupancy of RRP without considering RP and CP at all, see 2.7 for more details.

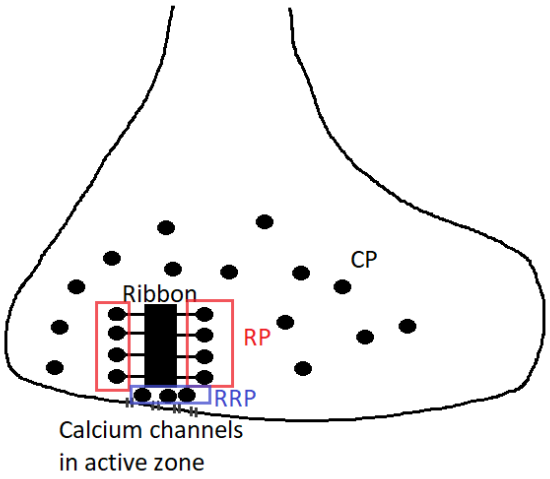

Figure 1.6: **Schematic picture of a ribbon in a terminal.** Three types of vesicles exist in a terminal containing ribbon, i) cytoplasmic vesicles flow on the cytocell making CP, ii) vesicles connected to the ribbon making RP, iii) readily releasable vesicles connected to the terminal membrane making RRP.

1.5 Objective and outline

This work is going to clarify crucial activation characteristics of DB4 BC from macaque's retina as well as rod BC in rat's retina when the cells are stimulated both intra- and extracellularly. To do this, multi-compartment models was applied to the real 3D morphology of the cells, as a fast and accurate framework, to calculate transmembrane voltage of the cells. Most of the results were compared to real electrical stimulation of in-vitro retina. External stimulation was done with a single point microelectrode which is a simple version of multi electrode arrays of real retinal implants. Furthermore, a model presenting general behavior of vesicle release from a single ribbon synapse presented that could explain the experimental data well. Finally, effect of periodic pulse on recovering of ribbon were discussed in details.

Substantial parts of the results section of this thesis published previously (Bassereh and Rattay, 2018a; Bassereh and Rattay, 2018b; Rattay et al., 2017; Rattay et al., 2018) or was submitted to review (Bassereh and Rattay, 2019).

- **Chapter 2** ***Methods*** presents all necessary methods for computing the presented results. All computational and mathematical basics are located here.
- **Chapter 3** ***DB4 BC with sphere soma*** presents the neuronal response of BCs during extracellular stimulation.
- **Chapter 4** ***Single-, two-, four-, and multi-compartmental model for DB4 BC with cone-cylinder-cone soma*** contains results of different models for retinal BCs and their similarities and differences.
- **Chapter 5** ***Vesicle release from a ribbon synapse of a BC*** contains results and a discussion of the presented models for neurotransmitter release from a retinal BC during intra- and extracellular stimulations.
- **Chapter 6** ***Conclusions*** states concluding remarks on this work.
- ***Appendix A*** contains two Python codes to calculate transmembrane of the cell in single and the three compartment models explained in chapter 2 and their detailed description.
- ***Appendix B*** contains the CV of the author.

Chapter 2

Methods

Neuronal cell membrane is mainly made of two phospholipid layers, so-called ′phospholipid bilayer membrane′. Each of the layers has a tail; which is mostly hydrophobic, and a head; which is hydrophilic. The two membrane layers are connected through the hydrophobic parts, Fig 2.1. The hydrophilic parts are polar and so absorb ions existing on their vicinities, while the hydrophobic parts are not polar. Thus, the phospholipid bilayer membrane itself works as a capacitor.

Since there is not any covalent lateral connections between the two layers of the membrane, different membrane proteins; e.g. ion channels, can float around on the membrane. Ion channels can be classified into three main groups 1- ion channels are permanently open and make a constant conductance for special ions either for cations or anions. 2- ion channels have a gating mechanism that their gates open only in case of a supra-threshold transmembrane voltage, so-called ′voltage-gated ion channels′. 3- ion channels have a gating mechanism but their gates open only in case of bounding with a ligand like Ca^{2+}; so-called ′ligand-gated ion channels′. Ion channels are capable of changing membrane conductance in different time scales so each of them can be considered as a variable or constant resistance. Thus finally, each small patch of the bilayer membrane containing ion channels is electrically equivalent to some resistances in series with their batteries (intracellular and extracellular concentration of different ions defines the battery), in parallel to a capacitor. If a patch of the membrane only contains ion channels with constant resistances is called linear or passive membrane and if it contains

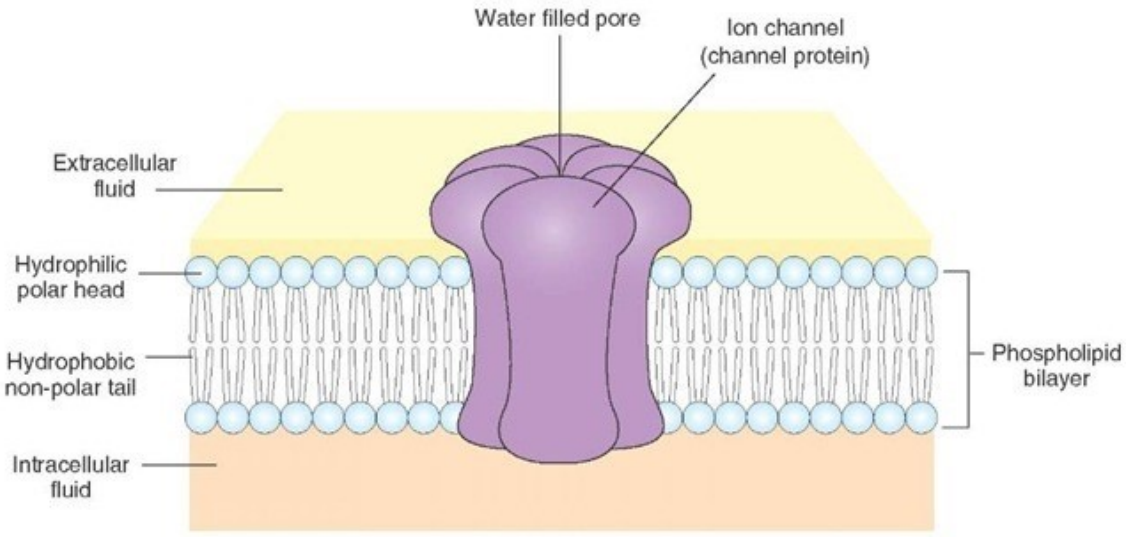

Figure 2.1: **Schematic representation of the neuronal membrane.** Phospholipid have a hydrophilic polar head and a hydrophobic nonpolar tail. The lipids connect to each other from their hydrophobic tails and their hydrophilic heads are outside the membrane. (picture taken from : http://what-when-how.com/neuroscience/electrophysiology-of-neurons-the-neuron-part-1/

different ion channels with variable resistance is called active membrane.

This chapter describes all mathematical and computational tools necessary to calculate the transmembrane voltage of any part of a neuron during intra- and extracellular electrical stimulations. First, the basics of a single compartment model will be explained. Second, the issue would be expanded to multi-compartmental method explaining a network of single compartments connected together. Third, all computational steps to calculate the transmembrane voltage of a simple neuron made of three passive compartments will be introduced using the Hodgkin-Huxley formalism. Next, ion channel kinetics of DB4 BC with sphere soma and real soma shape (two cones and a cylinder) will be explained. Finally, two models of vesicle release from a single ribbon will be introduced.

2.1 Compartment models

The most common approach to model the membrane voltage of neurons is ′compartmental model′. In this model, the neuron is considered to be made of one (single-compartment) or multiple (multi-compartment) compartments.

2.1.1 Single-compartment model

Three components may affect the membrane potential (or transmembrane voltage) while having only one compartment as mentioned above: 1- a capacitive current originating from insulating as well as polar features of the membrane 2- an ionic current explaining cross of ions through ion channels 3- an external stimulating current injected to the neuron.

Applying Kirchhoff's first law using all of these three terms leads to:

$$i_{cap} + i_{ion} + i_{stim} = 0 \tag{2.1}$$

$$\rightarrow \quad \frac{dV}{dt} * C + i_{ion} + i_{stim} = 0 \tag{2.2}$$

Where V is the membrane potential with the unit of mV, the terms i_{ion} and i_{stim} stand respectively for the ionic and injected current densities with dimension of $\mu A/cm^2$. C denotes the membrane capacitance in $\mu F/cm^2$ and time t has unit of ms. Throughout this work, all of the terms will presented in the same units. The terms 'membrane' and 'transmembrane' are the sam, too. The calculation of the term i_{ion} will be explained in section 2.2. Note that, in the single-compartment model, shape of the compartment is not of interested and only the total surface area of the neuron is important.

2.1.2 Multi-compartment model

Although single-compartment model would somehow works in a correct way specially for passive membranes, see chapter 4, it is not able to explain features of neuron with active membranes as well as when the cell is stimulated extracellu-

larly. Although simplifications of real morphology of the neurons would sometimes work as well, see chapter 4, it is necessary to extract real three-dimensional morphology of neurons to mimic their behavior more pragmatically.

Investigation of neuron's behavior while using their three-dimensional morphologies is called ′multi-compartment model′ and is based on the cable theory established by William Thomson in (1854). The starting point at which the model was expanded was at 1850 when Hermann von Helmholtz could measure the velocity of signal conduction in nerve fibers (Helmholtz, 1850) that had been considered to be infinite before. Then, introducing the concept of diffusion as a phenomenon exhibited by groups of particles by Einstein in (1905) and next very tremendous work of sirs Hodgkin and Huxley in (1952) on squid axon resulted in understanding general features of active membranes containing sodium and potassium ion channels. Rall used all of these findings and could present simple multi-compartment models (Rall, 1964).

Multi-compartmental method is actually a connected network of single compartments; see Fig 2.2. The connection between compartments is explained by ′axial currents′, which is an ohmic current, that flows in axial direction through the compartments. Applying Kirchhoff's first law for each compartment would lead to

$$i_{cap,n} + i_{ion,n} + i_{axial,n} + i_{stim,n} = 0 \tag{2.3}$$

$$\rightarrow \quad \frac{dV_n}{dt} * C + i_{ion,n} + i_{axial,n} + i_{stim,n} = 0 \tag{2.4}$$

The axial current for the nth compartment, $i_{axial,n}$, can be written as

$$\frac{V_n - V_{n-1}}{R_n/2 + R_{n-1}/2} + \frac{V_n - V_{n+1}}{R_n/2 + R_{n+1}/2} + \dots \tag{2.5}$$

Where $V_n - 1$ and $V_n + 1$ stand for the membrane potential of the neighbors connected to the n-th compartment and the dots at the end stand for possible

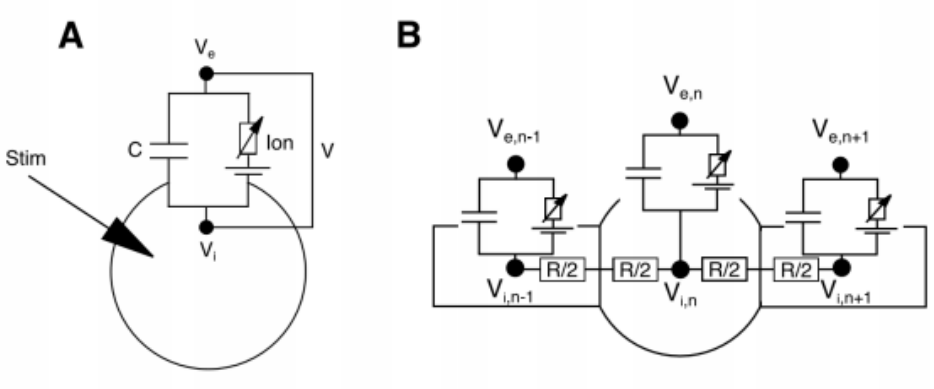

Figure 2.2: **Single (A) and multi-compartment models (B).** Multi-compartment method is actually a network of connected single compartments. In addition to a stimulus, an ionic and a capacitive current, which is found in the single-compartment model, multi-compartment model also contains an axial component between neighbored compartments. The membrane voltage V is the difference between the internal and external potential ($V_n = V_{i,n} - V_{e,n}$). (picture taken from (Werginz 2016, thesis)).

additional neighbors. $R_n/2$ is the resistance from the midpoint to the end of the n-th cylindrical compartment calculated by

$$\frac{R_n}{2} = \frac{\rho_i l_n}{2r_n^2\pi} \tag{2.6}$$

Where L_n is length of the compartment, $A_n = \pi r_n^2$ is cross section area of the compartment with radius r_n, and specific axial resistivity ρ_i. Unites of R, r, L, A_i, and ρ_i, are $k\Omega$, cm, cm, cm^2, and $k\Omega.cm$, respectively.

In Eq. 2.4, the term $i_{stim,n}$ refers to the current injected to the n-th compartment in intracellular stimulation, but, in extracellular stimulations, it is defined as

$$\frac{V_{e,n} - V_{e,n-1}}{R_n/2 + R_{n-1}/2} + \frac{V_{e,n} - V_{e,n+1}}{R_n/2 + R_{n+1}/2} \tag{2.7}$$

where $V_{e,n}$ is the extracellular applied voltage at the n-th compartment calculated via

$$V_{e,n} = \frac{\rho_e I_e}{4\pi r} \tag{2.8}$$

where I_e is the applied current to the electrode, ρ_e is the electric resistivity of the surrounding medium and r is the distance from center of each compartment to the electrode. Unites of I_e, ρ_e, and r are respectively μA, $k\Omega.cm$, and cm.

According to the activation function concept, Eq. 2.7 defines a virtual injected current that summarizes the driving forces of the n-th compartment resulting from the applied electrical field (Rattay 1999, Rattay et al. 2012). This way the extracellular stimulation becomes equivalent to the intracellular stimulation approach. Note that Eq. 2.7 looses one term for end compartments and obtains additional terms at branching points and at the soma.

In spite of single-compartment model, shape of the compartments are important in the multi compartmental model because shape of a compartment makes the related axial resistance. The morphology of any cell can be extracted by software like Neuromantic (Myatt et al., 2012). Although shape of the compartments are usually cylinders, soma sometimes is considered as a sphere. Although total surface of a sphere with radius r_s is $A_s = 4\pi r_s^2$, this surface can not be used to calculate the resistance of the soma since some part of the sphere will be vanished. Figure 2.3 shows how a sphere soma connects to a cylindrical compartment. The surface would be

$$A_s = 4\pi r_s^2 - \sum_j 4\pi r_s h_j \tag{2.9}$$

$$h_j = r_s - z_j \tag{2.10}$$

$$z_j = \sqrt{r_s^2 - r_j^2} \tag{2.11}$$

In order to compute the half resistance of the spherical soma from the middle

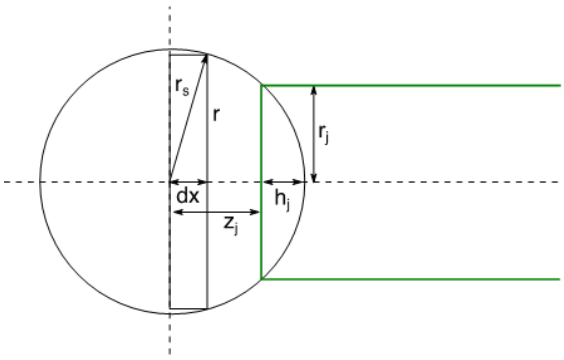

Figure 2.3: **A sphere soma is connected to its cylindrical neighbour** The half resistance from middle of the soma (black sphere) to each of its connected neighbors (green rectangular) is obtained by integrating the resistance from the middle axis of the soma to the contact surface. (picture taken from (Werginz 2016, thesis)).

point to each of its neighbors, $R_{s,j}/2$, we need to integrate the resistance from the middle axis of the soma to the contact surface with the connecting cylindrical compartment

$$\frac{R_{s,j}}{2} = \frac{\rho_i}{2} \int_0^{z_j} \frac{1}{r_s^2 - x^2} dx \tag{2.12}$$

$$\rightarrow \quad \frac{R_{s,j}}{2} = \frac{\rho_i}{2\pi r_s} ln \frac{r_s + z_j}{r_s - z_j} \tag{2.13}$$

Where ρ_i is the axial resistivity with $k\Omega.cm$ unit. r_j and r_s denotes the radiuses of connected compartment and soma, respectively, with the same cm units, see Fig 2.3.

After finding the axial resistance of each compartments, the axial current is expressed by multiplying an axial matrix M with the voltage vector V. M is computed by using a neighborhood matrix; also known as adjacency matrix. In the adjacency matrix, if two compartments are connected to each other, the related elements of the matrix is one, otherwise zero. See section 2.3.

$$i_{axial} = M * V \tag{2.14}$$

2.2 Membrane models

This section provides all needed information to model passive and active membranes and how the term i_{ion} is calculated by the Hodgkin-Huxley formalism.

Passive membrane

Kinetics of the membrane that does not contain any type of ion channel is explained by a linear leak current. Thus, the term i_{ion} will be

$$i_{ion} = g_L(V - E_L) \tag{2.15}$$

Where g_L is the conductance of the leak channel with mS/cm^2 unit, V in mV stands for membrane voltage obtaining by the difference between the internal and external potentials. E_L is the reversal potential of the leak current that mostly is equal with the resting potential.

Active membrane

The main work on propagation of action potentials as well as its simulation was done by Alan Lloyd Hodgkin and Andrew Fielding Huxley in (1952). They presented a mathematical framework for action potential generation and how it propagates. Hodgkin and Huxley's experiment using voltage-clamp method and their theoretical model for action potential; which is the main foundation of electrophysiology, leaded to win 1963 Nobel Prize in Physiology or Medicine.

In the voltage clamp method, the membrane voltage of the neuron is fixed at a $'$command voltage$'$ considered by the experimenter. Then, membrane voltage is recorded by a $'$voltage electrode$'$ at each time step and a $'$current electrode$'$ injects current into the cell simultaneously, with proportional negative or positive sign. Thus, the voltage clamp method is mainly a current injector. The electrode measuring the membrane potential is connected to an amplifier. The amplifier also receives inputs at each time step from the signal generator containing the command voltage. The amplifier subtracts the command potential from membrane potential ($V_{Command} - V_{Membrane}$). If the product was zero, no current is

sent to the current electrode. If the difference was more than zero, it means that the membrane needs some positive current to reach the command voltage and so the amplifier send current with positive sign to the cell until the difference of command and membrane voltages becomes zero. If the difference is negative, the amplifier sends current with negative sign to the neuron.

Although shape of the membrane voltage during an action potential had been recorded before, Hodgkin and Huxley suggested an interpretation for fast changes of membrane potential during action potential. They recognized that sodium and potassium ions play the vital role in action potential and these ions pass through pores. i.e. ion channels. They also detected that the open and closing states of these ion channels were dependent on the present state of the membrane potential, although they did not know biophysical properties of the ion channels. In this study, I consider depolarization of the membrane potential as increment in the membrane potential. Thus, inflow of positive ions will have negative sign; like sodium and calcium currents, and outflow will be positive; like potassium currents.

In the HH model, there are three terms for i_{ion}:

A term for sodium current

$$i_{Na} = g_{Na} m^3 h (V - E_N a) \tag{2.16}$$

A term for potassium current

$$i_K = g_K n^4 (V - E_K) \tag{2.17}$$

And a term of leakage related to membrane fluctuations

$$i_i on = g_L (V - E_L) \tag{2.18}$$

Where g_{Na}, g_K, and g_L are the maximum channel conductivities in mS/cm^2, m and n are activation variables and h is the inactivation variable. Gating variables of all channels change over time with

$$\frac{dX}{dt} = \frac{X_\infty - X}{\tau_X} \tag{2.19}$$

e.g. the equation for m is

$$\frac{dm}{dt} = \frac{m_\infty - m}{\tau_m} \tag{2.20}$$

and

$$X_\infty(V) = \frac{\alpha_X(V)}{\alpha_X(V) + \beta_X(V)} \tag{2.21}$$

$$\tau_X(V) = \frac{1}{\alpha_X(V) + \beta_X(V)} \tag{2.22}$$

Where X_∞ stands for the steady state value that the state variable X will finally reach to it at a fixed membrane potential. The time constant τ_X describes how long it takes for the state variable X to reach to the steady state. α and β are rate coefficients for opening and closing of the ion channel determined by HH to fit the measured data.

Considering Eqs. 2.21 and 2.22, Eq. 2.19 can be written as

$$\frac{dX}{dt} = \alpha_X - X(\alpha_X + \beta_X) \tag{2.23}$$

E_{Na}, E_K and E_L are the equilibrium potentials of each ion channel type X and can be calculated with the Nernst equation

$$E_X = \frac{RT}{2F} ln \frac{[X]_e}{[X]_i} \tag{2.24}$$

Where R is the gas constant ($8.314\ J.mol^{-1}.K^{-1}$), T stands for the temperature in Kelvin unit and F is the Faraday constant ($96485.3365 C.mol^{-1}$). $[X]_e$ and $[X]_i$ are the extracellular and intracellular ion concentrations, respectively.

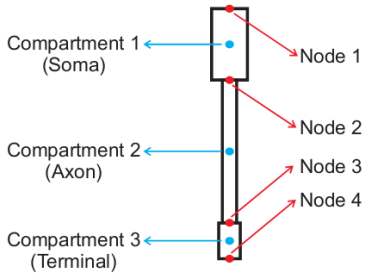

ID	TYPE	X	Y	Z	RADIUS	PARENT
1	1	0	0	0	5	-1
2	1	0	0	-10	5	1
3	2	0	0	-30	2	2
4	4	0	0	-35	3	3

Figure 2.4: **A neuron made of 3 compartments; one soma, axon and terminal, and its related .swc file in a table.** ID column presents an index from each node (red circles); the place where a compartment starts. TYPE presents the compartment belongs to which part of the cell (1 for soma, 2 for axon, and 4 for terminal in here). X, Y and Z are the three-dimensional coordinates of the nodes (in μm), RADIUS stands for the node radius and PARENT stores the ID of the connected nodes. The coordinates of the compartment; middle point of each compartment, are shown with blue points.

2.3 Geometry of neurons in .swc files, a simple example

Geometry (morphology) of any neuron can be stored in several formats. One of the most popular format is *.swc due to its very simple layout. Figure 2.4 shows a simple example of such a file. In a .swc file, each compartment has a single line except for the soma that is made of two or more compartments. In the format, the soma always is the starting point of the neuron, so it does not have neighbor and hence the related parent is indicated with $'$-1$'$.

To solve the equation 2.4 for the cell morphology explained in Fig 2.4 with considering passive membrane for all of soma, axon and terminal, the following steps should be done:

1. Finding length and surface of each compartments.
   That would be L_1=10, L_2=20, L_3=5 μm
   A_1=314.1, A_2=251.3, A_3=94.24 μm^2.

2. Finding midpoints of each compartments (this is an essential step in extracellular stimulation to compute the distance between all compartments and the electrode position, while this step should be ignored in intracellular stimulation).

$x_1 = x_2 = x_3 = y_1 = y_2 = y_3 = 0$
$z_1 = -5,\ z_2 = -20,\ z_3 = -32.5\ \mu m.$

3. Calculating resistance of each elements by considering $\rho_i = 0.1\ K\Omega.cm.$ R_1=127, R_2=1591, R_3=176 $K\Omega$.

4. Reducing one number from nodes and partner column and eliminating the first elements from remained ID, TYPE, X, Y, Z, Radius, Parent columns, see appendix A.

5. Finding the related connectivity matrix from new ID and partner columns.

$$C = \begin{bmatrix} 0 & 1 & 0 \\ 1 & 0 & 1 \\ 0 & 1 & 0 \end{bmatrix} \tag{2.25}$$

6. Finding the M matrix in Eq. 2.14 through the folloing formulas.

$$M_{ij} = \frac{-C_{ij}}{R_i/2 + R_j/2} \qquad if\ \ i \neq j \tag{2.26}$$

$$M_{ii} = -\sum_j M_{ij} \tag{2.27}$$

7. Making each of the terms in equation 2.4 in their matrix form as.

$$I_{Capacitor} = \begin{bmatrix} c\frac{dV_1(t)}{dt} \\ c\frac{dV_2(t)}{dt} \\ c\frac{dV_3(t)}{dt} \end{bmatrix} \tag{2.28}$$

$$I_{ion} = \begin{bmatrix} g_L(V_1(t) - E_L) \\ g_L(V_2(t) - E_L) \\ g_L(V_3(t) - E_L) \end{bmatrix} \tag{2.29}$$

$$I_{axial} = \begin{bmatrix} \frac{1}{A_1(R_1/2+R_2/2)} & \frac{-1}{A_1(R_1/2+R_2/2)} & 0 \\ \frac{-1}{A_2(R_2/2+R_1/2)} & \frac{1}{A_2(R_1/2+R_2/2)} + \frac{1}{A_2(R_2/2+R_3/2)} & \frac{-1}{A_2(R_2/2+R_3/2)} \\ 0 & \frac{-1}{A_3(R_2/2+R_3/2)} & \frac{1}{A_3(R_3/2+R_2/2)} \end{bmatrix} \begin{bmatrix} V_1(t) \\ V_2(t) \\ V_3(t) \end{bmatrix} \tag{2.30}$$

Replacing all of the terms in Eq. 2.4 leads to a matrix equation that must be solved numerically. In the following, the general definition of forward and backward Euler methods to solve differential equations as well as their formalism for HH model will be explained.

2.4 Solving methods

Since (coupled) ODEs like Eq. 2.4 cannot be solved analytically, a numerical method should be used instead. Some methods like forward and backward Euler, Crank-Nicholson (Crank and Nicolson, 1947) and Runge-Kutta (Kutta; 1901) method are usually used for solving ODEs numerically, each of which has its own advantages and disadvantages.

2.4.1 Forward Euler method

The philosophy behind forward Euler method is actually considering the first two terms of the Taylor series expansion that is actually the general derivation of the function. On the other hand, according to Taylor expansion

$$y(t+\Delta t) = y(t) + \Delta t\dot{y}(t) + \frac{(\Delta t)^2}{2}\ddot{y}(t) + ... \tag{2.31}$$

Considering the general definition of derivative function

$$\dot{y}(t) = \lim_{\Delta t \to +0} \frac{y(t+\Delta t) - y(t)}{\Delta t} \tag{2.32}$$

However, for any positive (small) Δt, the finite difference would be

$$\dot{y}(t) = \frac{y(t+\Delta t) - y(t)}{\Delta t} \tag{2.33}$$

By considering

$$\dot{y}(t) = f(t, y) \tag{2.34}$$

Eq. 2.33 would be

$$f(t, y) = \frac{y(t+\Delta t) - y(t)}{\Delta t} \tag{2.35}$$

By extracting $y(t+\Delta t)$ from this equation, the forward Euler method would be

$$y(t+\Delta t) = y(t) + \Delta t f(y, t) \qquad y(t=0) = y_0 \tag{2.36}$$

or

$$y_{n+1} = y_n + f(y_n, t_n)\Delta t \tag{2.37}$$

The advantage of the method is its simple implementation. In truncation of the Taylor series, an error is induced at every step known as the LTE. In general, a method with $O(h^{k+1})$ LTE is said to be of k-th order. For the forward Euler method, the LTE is $O(h^2)$ so the method is a first-order technique. Higher order techniques provide lower LTE for the same step size, so higher order methods are more precise.

2.4.2 Backward Euler method

Backward Euler method has the same strategy as the forward method with the difference that the current position of the function is calculated by the previous step. Thus

$$\dot{y}(t) = \frac{y(t) - y(t - \Delta t)}{\Delta t} \tag{2.38}$$

Again by considering $\dot{y}(t) = f(y(t), t)$

$$f(y(t), t) = \frac{y(t) - y(t - \Delta t)}{\Delta t} \tag{2.39}$$

Shifting the time t to $t + \Delta t$, this equation will be:

$$f(y(t + \Delta t), t + \Delta t) = \frac{y(t + \Delta t) - y(t)}{\Delta t} \tag{2.40}$$

Thus, the backward method can be witten as:

$$y(t + \Delta t) = y(t) + f(y(t + \Delta t), t + \Delta t)\Delta t \tag{2.41}$$

or

$$y_{n+1} = y_n + f(y_{n+1}, t_{n+1})\Delta t \tag{2.42}$$

In this study, a backward Euler method was used since we did not need high resolution for such ODEs and this model is so simple to implement.

2.4.3 Ionic current using Forward and Backward Euler methods

In order to solve Eq. 2.4, the differential equations for the state variables (x= m, h, n, ..) should be solved; considering Eq. 2.23. The related solutions both for Forward and backward Euler are

$$\frac{dx}{dt} = \alpha_x - x(\alpha_x + \beta_x) \tag{2.43}$$

$$\text{Forward Euler} \qquad x_{t+dt} = x_t + (\alpha_x - x_t(\alpha_x + \beta_x))dt \tag{2.44}$$

$$\text{Backward Euler} \qquad x_{t+dt} = x_t + (\alpha_x - x_{t+dt}(\alpha_x + \beta_x))dt \tag{2.45}$$

$$\rightarrow \qquad x_{t+dt} = \frac{x_t + dt\alpha_x}{1 + (\alpha_x + \beta_x)dt} \tag{2.46}$$

The ionic current and membrane voltage V at time $t + dt$ using Backward Euler method would be (since the forward method is so strict, we did not talked about them)

$$i_{ion_{t+dt}} = g_{Na}m^3_{t+dt}h_{t+dt}(V - E_{Na}) + g_K n^4_{t+dt}(V - E_K) + g_L(V - E_L) \tag{2.47}$$

$$V_{t+dt} = V_t + \frac{dV(t + dt, x_{t+dt})}{dt}dt \tag{2.48}$$

with the voltage derivative of

$$\frac{dV(V_{t+dt}, x_{t+dt})}{dt} = (-M * V_{t+dt} - I_{ion,t+dt} - I_{stim,t+dt}) * \frac{1}{C} \tag{2.49}$$

Combining both equations 2.48 and 2.49 results in

$$V_{t+dt} = V_t + (-M * V_{t+dt} - I_{ion,t+dt} - I_{stim,t+dt}) * \frac{dt}{C} \tag{2.50}$$

$$\rightarrow (I + M * \frac{dt}{C}) * V_{t+dt} = V_t + (-I_{ion,t+dt} - I_{stim,t+dt}) * \frac{dt}{C} \tag{2.51}$$

Where I is the identity matrix having the same size as M, the term $I_{ion,t+dt}$ can be obtained using equation 2.47 and $I_{stim,t+dt}$ is the stimulus current vector at time $t + dt$.

2.5 DB4 BC with spherical soma

Retinal implants generate artificial spikes in GCs that lead to visual perceptions in the blind. These spikes are made by stimulation of GCs, which is done in epiretinal implants, or via synapses from stimulated BCs in subretinal implants (Boinagrov et al., 2014; Sekhar et., 2016; Sekirnjak et al., 2008). Stimulation with electrodes close to BCs in subretinal implants permits patients to use the natural pathway of the eyes that may lead to better vision in comparison to artificial vision resulted from stimulation of GC axons in epiretinal implants (Greenberg et al., 1999; FitzGibbon, 2017; Rattay and Resatz, 2004). Although BC stimulation seems to be closer to the eye's natural signaling pathway, many features of BC responses to electrical stimulation are still not known. GCs and amacrine cells were considered to be the only spiking cells in the retina for many years, whereas signaling of all other retinal neurons were only assumed to be processed via graded potentials. However, both sodium and calcium spikes have been recently recorded in fish and mammalian BCs (Baden et al., 2013a; Cui and Pan, 2008; Walston et., 2015). From the neural engineering point of view, investigations on non-human primates are of special interest as their BCs are similar to humans' BCs.

Motion and flicker detection are done by BCs of the magnocellular pathway in the primate retina. Detection of the features needs high temporal resolution done by the cells. Generation of sodium spikes, compared to graded potentials, may supports this fast signal transport from PRs to GCs.

DB4 bipolar cell of the macaque's retina is the first case of study in this thesis. The cell morphology was extracted from (Puthussery et al., 2013) with the difference that a spherical soma was replaced with the real cylindrical-shaped soma. In 2.5 -left, the 3-D model of the cell is shown. DB4 is an ON (cone) BC making reciprocal synapses with AII amacrine cells. This is the first type detected by Polyak (Polyak et al., 1941).

Bipolar retinal cells have a short axon chain affecting number of sodium channels available on the cell, if any. The small sodium density is just able to generate a spikelet rather than an action potential. Amplitude of action potential is 100

mV more than spikelet. Note that, a BC can operate both via spikelets and graded potentials. Sending a spike to the synaptic terminals results in releasing of a larger amount of neurotransmitter at the synaptic connections to GCs and amacrine cells; see 5.

Figure 2.6 shows all types of retinal BCs of the macaque (Tsukamoto and Omi, 2015). From morphological point of view, dendrites of all bipolar types stratify at the same level in the OPL, but lentgh of the axons differ in different strata ($1 \sim 5$) of the IPL.

In the macaque's retina, three types of BCs contain sodium channels, two of which are only able to generate spike (Puthussery et al., 2013). Sodium channels are located at the AIS, also called sodium band. AIS is the place where the spike initiates in almost all types of neurons (Fried et al., 2009; Mainen et al., 1996). The most conductive part of the AIS in the DB4 BC has density of $1000\,mS/cm^2$. The sodium conductivity of the AIS has been shown in the histogram in 2.5 -right.

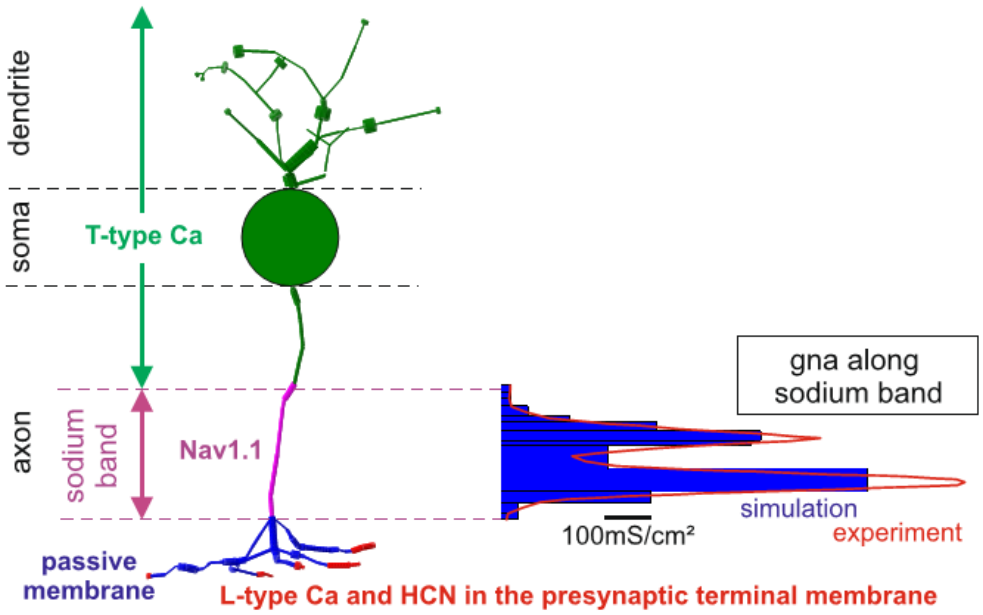

Figure 2.5: **3D model of a DB4 BC with a spherical soma and soma diameter of** 10.3 μm**).** The cell consists of 116 cylindrical compartments (left), the distribution of the sodium ion channels (right). The colors in the left imply on the types of the ion channels located on the cell membrane. A peak conductance value close to $g_{Na} = 1000\, mS/cm^2$ for voltage-dependent sodium channel type $Na_v1.1$ magnifies the role of sodium channels during spike generation. Calcium spikes are not generated in this cell type since calcium ion channels are located at soma and dendrite (green) having a large membrane surface, so such a small axial resistivity, as well as low calcium conductance value g_{Ca} between 1 and 2 mS/cm^2. The values of the blue g_{Na} histogram were used for the 9 sodium band compartments. Cell geometry and experimental data from (Puthussery et al., 2013).

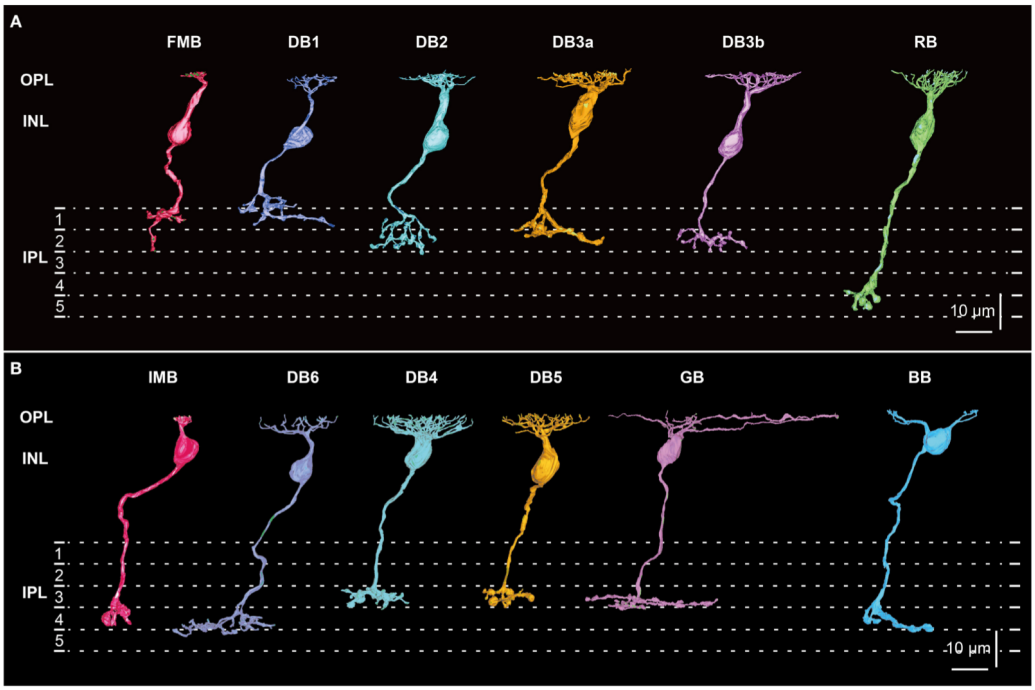

Figure 2.6: Morphology and stratication of OFF BCs (FMB, DB1, DB2, DB3a, and DB3b) and ON BCs (RB, IMB, DB4, DB5, DB6, GB, BB) in the macaque's retina. Strata 1-2 comprise the OFF sublamina and strata 3-5 define the ON layer. FMB cell-1 and cell-6 (FMB-1 and FMB-6) are connected to M/L and S cones, respectively. Each stratum of the IPL (1-5) is 6 μm thick. Picture taken from (Tsukamoto and Omi, 2015).

General geometrical properties of DB4 BC, a retinal ganglion and a brain pyramidal cell as well as their sodium channel densities are available in Table 2.1 in order to investigate origin of spike generation in the three different neurons; see (Rattay et al., 2017) for more details. Sodium band may vary in channel density, length, diameter, and its distance to the soma depending on the type of neurons.

2.5.1 Morphometry of the cell

The DB4 BC model is based on the reconstructed 3D morphology of the cell from macaque's retina and ion channel dynamic data according to (Puthussery et al., 2013). To simplify the calculations and as the soma effect was not of our interest,

	BC	GC	Pyramidal Cell
Dendrite $g_{Na}(mS/cm^2)$	0	25	8
Soma $g_{Na}(mS/cm^2)$**)**	0	80	8
Axon $g_{Na}(mS/cm^2)$	0	70	300
Sodium band $g_{Na}(mS/cm^2)$	350	400	420
Soma diameter (μm)	10.3	20	20
Sodium band diameter (μm)	0.5	2	1.22
Sodium band length (μm)	26	40	50
Distance between sodium band and soma (μm)	4.7	40	10
Main reference	Ref 1	Ref 2	Ref 3
Additional reference		Ref 4 Ref 5	Ref 6 Ref 7

1- Ref 1 :(Puthusserry et al., 2013)
2- Ref 2: (Rattay et al., 2014)
3- Ref 3: (Rattay et al., 2012)
4- Ref 4: (Sheasby et al., 1999)
5- Ref 5: (Jeng et al., 2011)
6- Ref 6: (Mainen et al., 1996)
7- Ref 7: (Hu et al., 2009)

Table 2.1: Morphometric features as well as sodium channel density of three different cells; see (Rattay et al., 2017) for more details.

the soma of the cell containing two cones and a cylinder was replaced by a sphere with the same surface area. The HH model (Hodgkin and Huxley, 1952) has been used for all channels.

Leak current conductance $g_L = 0.033\ mS/cm^2$ and membrane capacitance $C_m = 1\ \mu F/cm^2$ were taken from (Puthussery et al., 2013). Temperature coefficients were used to simulate the dynamics at $31°C$ (Rattay et al., 2002) in all of the calculations. In the following section, all presented channels with their dynamics are explained in detail. Intracellular resistivity was $0.1\ k\Omega.cm$ (Kasi et al., 2011; Werginz and Rattay, 2016).

Kinetics of the channels

- **Sodium channel** $Na_V1.1$ with the g_{Na} shown in Figure 2.5. Sodium channel density distribution has a peak represented by $1000\ mS/cm^2$ shown in Figure 2.5.

$$\begin{aligned} G_{Na_V1.1} &= g_{Na} \times m_{Na}^3 \times h_{Na} \times s_{Na} \\ I_{Na} &= G_{Na_V1.1} \times (V - E_{Na}) \\ with\ E_{Na} &= 50\ mV \end{aligned} \tag{2.52}$$

  - kinetics of activation (Puthussery et al., 2013); Spampanato et al., 2004; Barela et al., 2006)

$$\begin{aligned} V_{1/2} &= -27.2\ mV \\ Z &= 4.6\ mV \\ m_\infty(V) &= \frac{1}{(1 + exp(-(V - V_{1/2})/Z)} \\ \tau_m &= 0.612 + \frac{1}{exp(-(V + 132.)/16.7) + exp(+(V + 16.8)/18.2)} \end{aligned} \tag{2.53}$$

– kinetics of fast inactivation (Spampanato et al., 2004)

$$
\begin{aligned}
&V_{1/2} = -60\,mV \\
&Z = 7.7\,mV \\
&h_\infty(V) = \frac{1}{(1 + exp(-(V - V_{1/2})/Z)} \\
&\tau_h(V) = 20.1 * exp(-0.5(V + 61.4)/32.7)^2
\end{aligned}
\tag{2.54}
$$

– kinetics of slow inactivation (Spampanato et al., 2004)

$$
\begin{aligned}
&V_{1/2} = -60\,mV \\
&Z = 5.4\,mV \\
&s_\infty(V) = \frac{1}{(1 + exp(+(V - V_{1/2})/Z)} \\
&\tau_s = 1000 \times (106.7 \times exp(-0.5 \times ((V + 52.7)/18.3)^2))
\end{aligned}
\tag{2.55}
$$

- The **T-type Calcium channels** $Ca_v3.1$ is assumed to be of constant density $g_{Ca} = 2\,mS/cm^2$ located at soma, dendrite, and axon hillock compartments. Its m (activation) and h (inactivation) gates are defined by $V_{0.5} = -57,\ -81\ mV$ and slopes $z = 6.2,\ 4\,mV$, respectively, (Deleuze et al., 2012).

$$
\begin{aligned}
&G_{Ca_{V3.1}} = g_{Ca} \times m_{Ca}^2 \times h_{Ca} \\
&I_{CaV3.1} = G_{Ca_{V3.1}} \times (V - E_{Ca}) \\
&with\ E_{Ca} = 20\,mV
\end{aligned}
\tag{2.56}
$$

– kinetics of activation (Deleuze et al., 2012)

$$
\begin{aligned}
&V_{1/2} = -57\,mV \\
&Z = 6.2\,mV \\
&m_\infty(V) = \frac{1}{(1 + exp(-(V - V_{1/2})/6.2)} \\
&\tau_m = 0.612 + \frac{1}{exp(-(V + 132.)/16.7) + exp(+(V + 16.8)/18.2)}
\end{aligned}
\tag{2.57}
$$

– kinetics of inactivation

$$
\begin{aligned}
&V_{1/2} = -81\ mV \\
&Z = 4\,mV \\
&h_\infty(V) = \frac{1}{1 + exp(+(V - V_{1/2})/4)} \\
&\tau_\infty(V) = 28 + exp(-(V + 22)/10.5)\ for\ V \geq -81mV \\
&\tau_\infty(V) = exp((V + 467.)/66.6)\ for\ V < -81mV
\end{aligned}
\tag{2.58}
$$

- **L-type Calcium channels** $Ca_V1.4$ with $g_{Ca} = 10^{-4}\,mS/cm^2$ presented in terminals (Baden et al., 2013b).

$$
\begin{aligned}
&G_{Ca} = g_{Ca} \times c^3 \\
&I_{Ca} = G_{Ca} \times (V - E_{Ca}) \\
&with\ E_{Ca} = 20\,mV
\end{aligned}
\tag{2.59}
$$

– Dynamic of the channel with variable gate c (Wergniz and Rattay, 2016)

$$
\begin{aligned}
\alpha_c(V) &= -0.3 \times \frac{(V+70)}{exp(-0.1 \times (V+70)) - 1} \\
\beta_c(V) &= 10 \times exp(\frac{-(V+38)}{9}) \\
c_\infty(V) &= \frac{\alpha_c}{\alpha_c + \beta_c} \\
\tau_c(V) &= \frac{1}{\alpha_c + \beta_c}
\end{aligned}
\tag{2.60}
$$

- **Hyperpolarization-activated cyclic nucleotide-gated (HCN) channels** with $g_{HCN} = 10^{-5} mS/cm^2$ presented in terminals (Rattay et al., 2017).

$$
\begin{aligned}
G_{HCN} &= g_{HCN} \times y \\
I_{HCN} &= G_{HCN} \times (V - E_{HCN}) \\
&with\ E_{HCN} = -40\, mV
\end{aligned}
\tag{2.61}
$$

  – Dynamics of the channel with variable gate y (Zhang et al., 2000).

$$
\begin{aligned}
\alpha_y(V) &= exp(\frac{-(V+78.91)}{26.62}) \\
\beta_y(V) &= exp(\frac{(V+75.13)}{21.25}) \\
y_\infty(V) &= \frac{\alpha_y}{\alpha_y + \beta_y} \\
\tau_y(V) &= \frac{1}{\alpha_y + \beta_y}
\end{aligned}
\tag{2.62}
$$

- **Potassium channels**

  There are two types of potassium channels; fast and slow types. The fast type is located in sodium band with $g_K = 2\, mS/cm^2$ but the slow potassium channel is located at the soma, dendrite, and axon hillock with $g_K = 2.4\, mS/cm^2$. This conductance value was derived from the voltage clamp experiments in (Puthussery et al., 2013); see (Rattay et al., 2017) for

more details. The kinetics of potassium channels are based on the original HH potassium channel with two difference of voltage offset and tau rate. The tau rate makes the channel slow by the given factor. The fast potassium channel of the sodium band is shifted by 5 mV and has a tau rate of 5 that means 5 times slower than standard HH potassium channel. The slow channel type has no voltage shift but tau rate of 8.

The **fast potassium channel** with $g_K = 2mS/cm^2$ located at sodium band (Hodgkin and Huxley, 1952)

$$\begin{aligned} G_K &= g_K \times n^4 \\ I_{Kslow} &= G_K \times (V - E_K) \end{aligned} \tag{2.63}$$

– Dynamics of the channel

$$\begin{aligned} V_{offset} &= 5\,mV \\ \tau_{rate} &= 5 \\ \alpha_n(V) &= 0.1 \times -0.1 \times \frac{(V - V_{offset} + 55)}{exp(-0.1 \times (V - V_{offset} + 55)) - 1} \times \frac{1}{\tau_{rate}} \\ \beta_n(V) &= 0.125 \times exp(\frac{(V - V_{offset} + 65)}{-80}) \times \frac{1}{\tau_{rate}} \\ n_\infty(V) &= \frac{\alpha_n}{\alpha_n + \beta_n} \\ \tau_n(V) &= \frac{1}{\alpha_n + \beta_n} \end{aligned} \tag{2.64}$$

The **slow potassium channel** with $g_K = 2.4mS/cm^2$ located at soma, dendrite and axon hillock (Hodgkin and Huxley, 1952).

Channel Type	Q_{10}	T'
NaV1.1	Q_{10_m}= 2.2 Q_{10_h}= 2.9 Q_{10_s}= 2.9	20
T-type Calcium channel	Q_{10_m}= 5 Q_{10_h}= 3	24
L-type Calcium channel	1	10
HCN1	1	37
Fast potassium channel	2	6.3
Slow potassium channel	2	6.3

Table 2.2: Temperature Parameters

$$\begin{aligned} G_K &= g_K \times n^4 \\ I_{Kslow} &= G_K \times (V - E_K) \end{aligned} \tag{2.65}$$

– Dynamics of the channel

$$\begin{aligned} V_{offset} &= 0mV \\ \tau_{rate} &= 8ms \\ \alpha_n(V) &= 0.1 \times -0.1 \times \frac{(V - V_{offset} + 55)}{exp(-0.1 \times (V - V_{offset} + 55)) - 1} \times \frac{1}{\tau_{rate}} \\ \beta_n(V) &= 0.125 \times exp(\frac{(V - V_{offset} + 65)}{-80}) \times \frac{1}{\tau_{rate}} \\ n_\infty(V) &= \frac{\alpha_n}{\alpha_n + \beta_n} \\ \tau_n(V) &= \frac{1}{\alpha_n + \beta_n} \end{aligned} \tag{2.66}$$

The temperature dependency of all channels needed to be considered according to the following rule

$$\tau'_x = \tau_x \times Q_{10}^{-(T-T')/10} \tag{2.67}$$

Where Q_{10} is the change of time constants for a 10 degree difference in temperature that is measured experimentally, T is the stimulation temperature set at 31 $^{\circ}C$ and T' is the temperature at which the initial dynamics has been measured. All temperature parameters for the six presented channel types have been shown in Table 2.2. The GC model is based on traced data (Jeng et al., 2011).

Finally, the ionic current equation is written as

$$I_{ion} = I_{Na} + I_{Ca_{V3.1}} + I_{Ca} + I_{HCN} + I_{Kslow} + I_{Kfast} + I_L \tag{2.68}$$

2.5.2 Experimental spike versus simulation

Using the kineticks explained above for different types of ion channels would lead to produce the same spike shape of the DB4 BC in comparison to experiment, Fig 2.7.

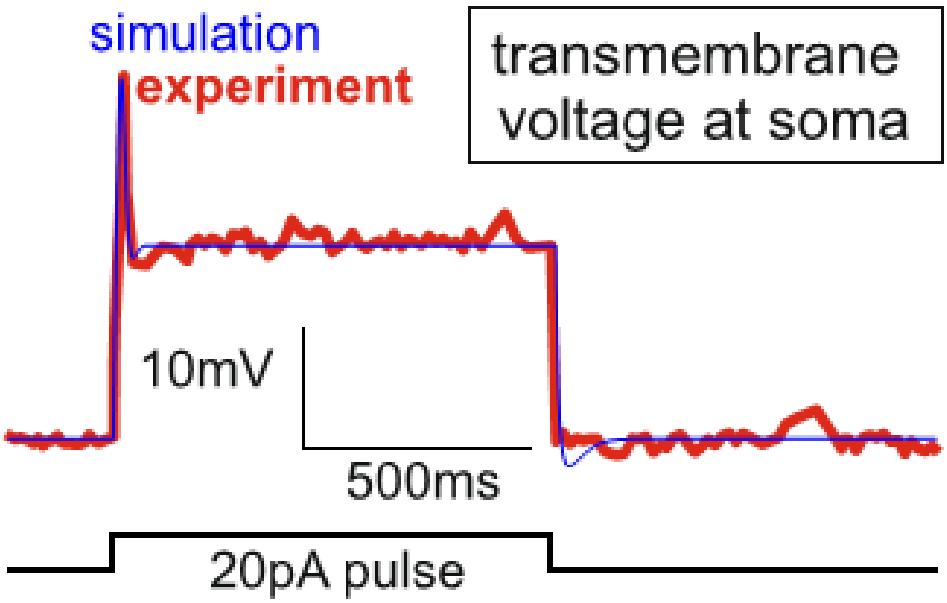

Figure 2.7: **Model versus experiment.** Shape of the spike of DB4 BC in experiment and simulation.

The results related to the cell containing these channels are discussed in 3; see (Rattay et al., 2017) for more details.

2.6 Single, two, four and multi compartmental models for DB4 BC with cone-cylinder-cone soma

Retinal BCs are one of the smallest neurons in the nervous system. More than 12 types of BCs have been reported for different vertebrates (Li et al., 2012; Light et al., 2012; Tsukamoto and Omi, 2016). Cell size and morphology are the two main factors varying between BC types in the same animal.

Different ion channels like sodium, potassium, HCN, and calcium ion channels have been reported in BCs. Ion channel types and densities change among the cell types and region within the cell (Hellmer et al., 2016; Hu et al., 2009; Ivanova and Müller F, 2006; Klumpp et al., 1995; Müller et al., 2003; Puthussery et al., 2013; Vielma and Schmachtenberg, 2016). Very large axon terminals of BCs in fish made it possible at first to quantify the ion channels existing on these cells. Usui et al. (1996) used an early single compartment model to explain this quantification.

Amacrine and GCs were only candidates of generating action potentials (spikes) in the retina for many years, but recently spiking has also been detected in BCs (Baden et al., 2013a; Cui and Pan, 2008) that is mainly because of sodium channels located in the axon (Greschner et al., 2014; Newkirk et al., 2013; Uzzell and Chichilnisky, 2004). Two types of BC, DB3a and DB4, both of which belong to the magnocellular pathway in the macaque's retina, are involved in motion and flicker detection. Although another type, DB3b type, is contains sodium channels, only these two types are able to generate action potentials. Their ability to generate sodium spikes causes fast signal transportation from PRs to GCs (Euler et al., 2014). Before detection of sodium channels in BCs, several types of ion channels had been recorded on the membranes (Kaneko et al., 1989; Lasater, 1988; Tessier-Lavigne et al., 1988). Most of these channels are common between spiking and non-spiking cells.

Modeling BCs has been used to simulate a variety of scenarios, from BCs' input by PRs (Ishihara et al., 1998; Ishihara et al., 2003), to artificial stimulation by patch-clamp (Oltedal et al., 2007; Usui et al., 1996) and extracellular electrodes

(Benav, 2012; Freeman et al., 2011; Resatz and Rattay, 2003; Rattay et al., 2003). Simulation of BC located in an external field generated by extracellular electrodes has applications in the design and interpretation of retinal implants (Chuang et al., 2014).

As explained before, the most common approach for modeling neurons is the compartment model that refers a cell to one or more compartments. The compartments are usually cylinders. Interactions between the environment and compartments and between compartments themselves are governed by equivalent electrical circuits representing the electrophysiological properties of the cell. The main parameters including electrophysiological properties are membrane capacitance, which usually has the same value per unit area in all compartments, different conductivities representing ion channels, and axial resistance, which determines the connection power between connected compartments using length and diameter of two neighbors (Rattay, 1999; Rattay et al., 2002).

The following subsections provide an overview over the most commonly used BC compartment models.

2.6.1 Single compartment model (SCM)

In the SCM, which is the simplest possible case, the entire cell is simulated by just one compartment. The main advantage of this model is the small need for computational resources and time. However, there are a number of disadvantages that make it unuseful in many cases. For example, homogeneously distributed ion channel density makes it unsuitable to simulate spiking. SCM also cannot be used to simulate extracellular stimulation as well.

Although there are some main limitations in SCM, it has successfully been used in modeling a different phenomena related to BCs. For example, Ishihara et al. (1998) used SCM to simulate a system made of rod and cone PRs connected to BCs, each of which was represented by a SCM (Ishihara et al., 1998). Investigation of the role of gap junctions in improving the dynamic range of the retina using SCMs was done by (Publio et al., 2009). Also, a recent study by Ishihara that investigates the roles of AMPA receptor kinetics in OFF-BCs was

done using SCM (Ishihara, 2017).

2.6.2 Two compartment model (TCM)

The next most simple model after SCM is TCM. Although it is more complex than SCM, it has advantages of short timing like SCM while it allows each compartment to have different properties such as ion channel distribution. This model was used by Ishihara and coworkers (Ishihara et al., 2003) to analyze the impact of ionic currents on light responses using a model made of a soma and an axon terminal compartments connected by a resistor playing role of the axon. The TCM has also been useful for modeling BCs with a passive membrane; the same as SCM, (Mennerick et al., 1997; Oltedal et al., 2007) as well as in extracellular stimulation when the transmembrane voltage is recorded only at the terminal (Freeman et al., 2011).

2.6.3 Multi compartment model (MCM)

MCM refers to a model with at least three compartments. They are usually 3D models made of many cylindrical, spherical or cone-shaped segments similar to the morphology of a real cell. The 3D model is obtained by one of different tracing techniques such as filling the neuron with fluorescent markers, known as dyes, before imaging by a two photon (Duebel et al., 2006), confocal (Saszik and DeVries, 2012) or electron microscope (Haverkamp et al., 2003).

Although this model is the most precise model to simulate BCs, it has not been used frequently due to not having real morphologies of BCs. Oltedal and coworkers by help of MCM investigated the effect of axon morphology on the passive signal attenuation between soma and axon terminal in a rat rod BC (Oltedal et al., 2009). MCM was also used to study the response of ON and OFF BCs during extracellular stimulation (Werginz et al., 2015) to analyze the impact of calcium current reversal on neurotransmitter release during subretinal stimulation (Werginz and Rattay, 2016) and to simulate sodium spikes in a BC (Rattay et al., 2017). Figure 2.8 shows the equivalent circuit for all of SCM, TCM, FCM. For FCM see section 2.6.5.

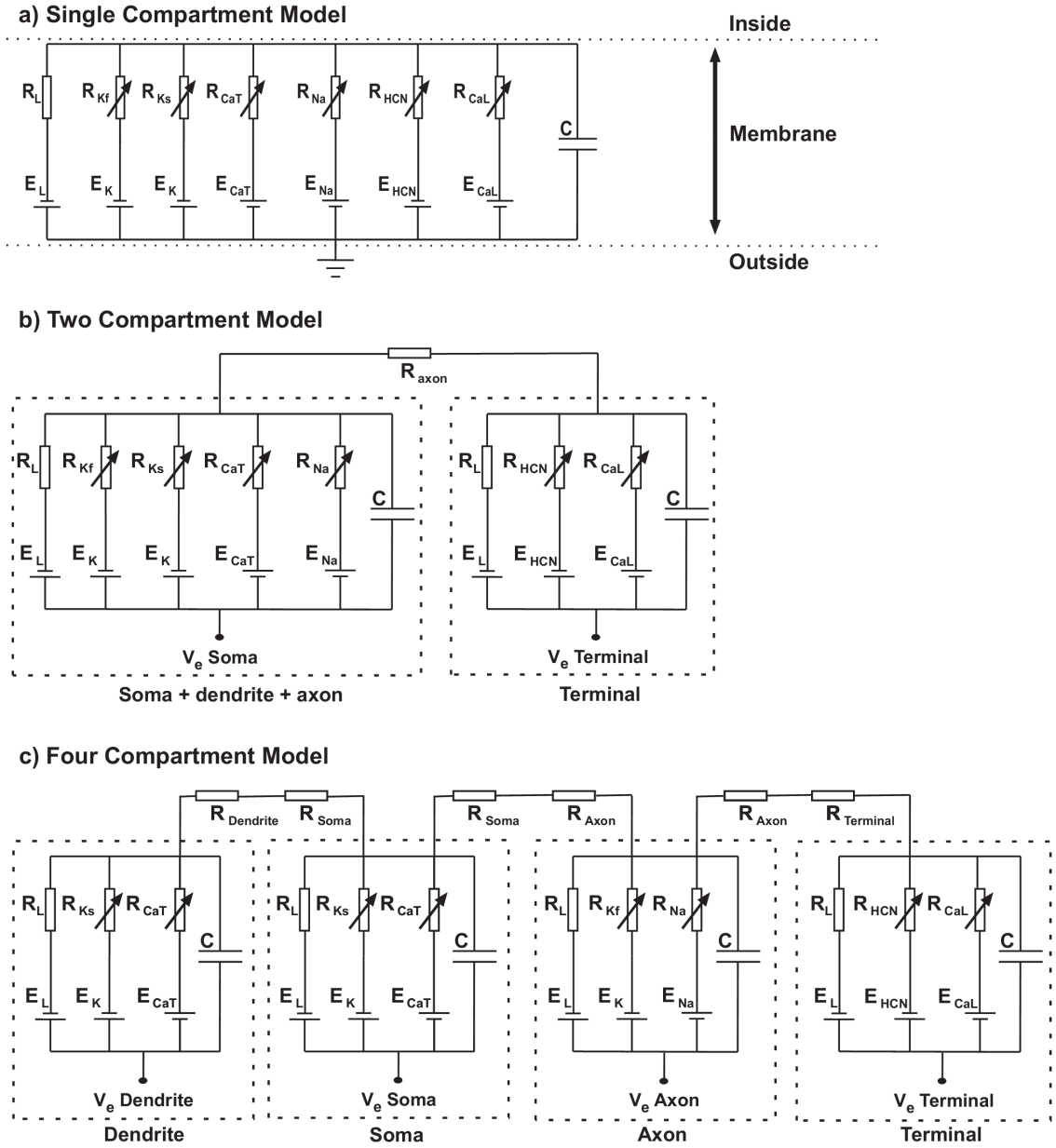

Figure 2.8: **Equivalent electrical circuits for a) SCM, b) TCM, c) FCM.**

2.6.4 Conversion of MCMs from 3D to 2D

Although there are three-dimensional neuron morphologies in internet databases, these data banks still do not cover BCs well. To overcome to this issue and considering there are a lot of 2D BCs' pictures in different papers, a Matlab method was developed to generate 3D cell geometries (Encke et al., 2013) based on 2D morphologies (Haverkamp et al., 2003; Strettoi et al., 2010). According to Encke's method, the positions and local diameters of the neuron parts from the 2D image is extracted and the missing third dimension is estimated with a normally distributed random values; see section 2.7 for more details.
The required number of compartments and responses of a model depend mainly on the questions it is going to address. If different models generate approximately similar results, it is rational to choose the least resource intensive one, which actually means the one with fewer compartments. Another application models with few compartments is situations in which the 3D MCM is not available.

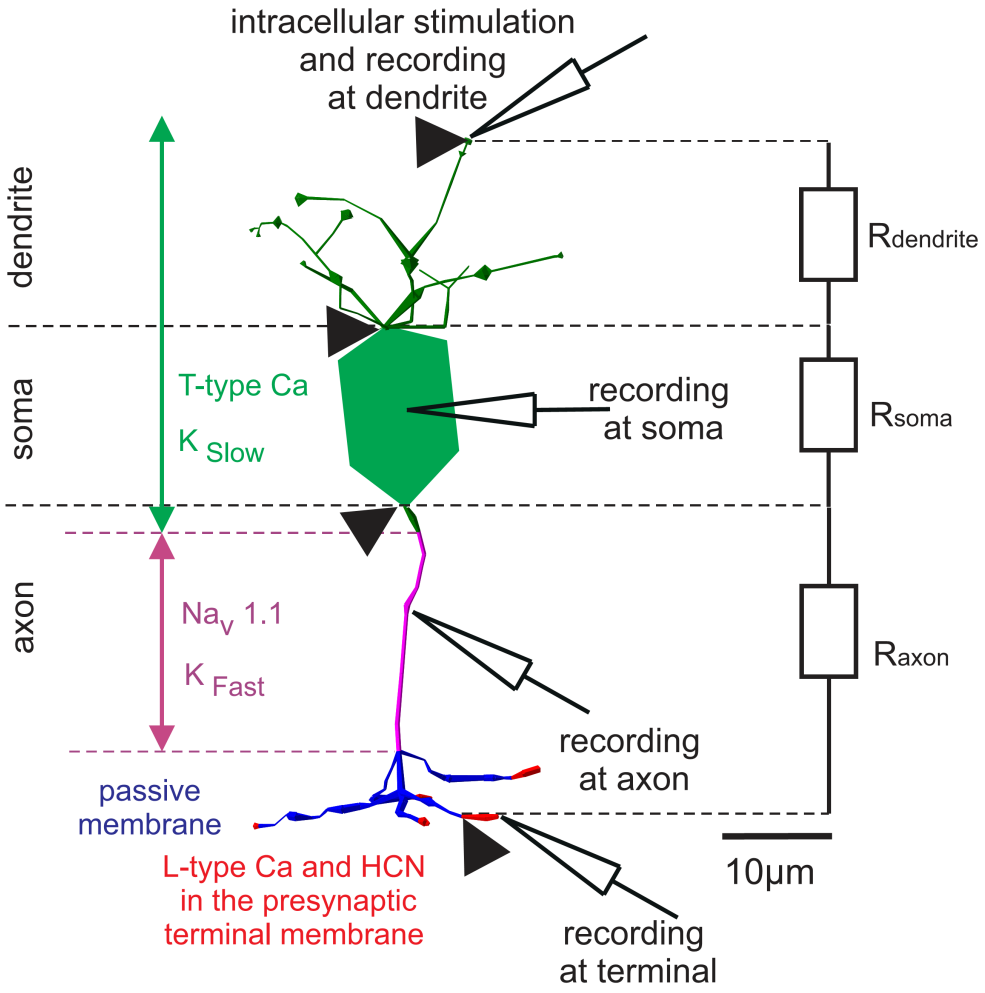

Figure 2.9: **Functional segments with the main ion channel types of a DB4 BC consisting of 117 compartments.** The soma is made of two cones and one cylinder. Dendrites, soma, and axon hillock contain Cav3.1 and slow potassium channels highlighted in green. Nav1.1 sodium channels and fast-type potassium channels are distributed on the axon (purple); the blue parts represent the passive parts of the axon. The terminals (red) contain HCN and L-type Cav1.4 channels. The diagram shows a typical simulation task where the BC was stimulated via synaptic input current and the response was recorded at 4 sites. Cell geometry and experimental data were taken from (Puthussery et al., 2013).

The four models investigated in this study were one-, two-, four- and multi compartment cells. For all models, the membrane capacitance was $1\mu\ F/cm^2$

based on the mentioned number in (Puthussery et al., 2013), the same for the intracellular resistivity 0.1 $k\Omega.cm$, extracellular resistivity 1 $k\Omega.cm$, and the leak current conductance $g_L = 0.033\, mS/cm^2$. It seems that DB4 BC has the lowest leak current conductance among several reported values (Freeman et al., 2011; Oltedal et al., 2007; Oltedal et al., 2009; Werginz et al., 2015). Passive models also contain the same features as active models but all ion channels are removed except for the leak conductance. All simulations were run at 31 $^{\circ}C$ (Rattay et al., 2002).

2.6.5 Ion channels distribution

The 3D morphology of a DB4 is based on a cell with 117 compartments; Fig 2.9 comparable to the morphology of Fig 2.5. The difference is the soma shape that a spherical soma is replaced with a cone-cylinder-cone structure that better fits the shape of the original cell.

Kinetics of the channels in MCM

- The **Sodium channel** $Na_V1.1$ density has two peaks on the axon represented by $g_{Na} = 650\, and\, 1000 mS/cm^2$ that were at a distance of 12.3 μm and 22.7 μm from the soma, respectively (Puthussery et al., 2013). In the MCM, axon stimulation was applied to the most excitable compartment with $g_{Na} = 1000 mS/cm^2$. Sodium channel kinetics were based on (Spampanato et al., 2004; Barela et al., 2006). To determine the inactivation variable h, data from a 5 Hz sinusoidal current injection experiment was fitted by $\tau_{corr} = 4$ (Puthussery et al., 2013).

$$
\begin{aligned}
&G_{Na_V1.1} = g_{Na} \times m_{Na}^3 \times h_{Na} \times s_{Na} \\
&I_{Na} = G_{Na_V1.1} \times (V - E_{Na}) \\
&with\ E_{Na} = 50.0\, mV
\end{aligned}
\tag{2.69}
$$

– kinetics of activation (Puthussery et al., 2013; Aradi and Soltesz, 2002)

$$\begin{aligned} V_{1/2} &= -27.2\,mV \\ Z &= 4.9\,mV \\ m_\infty(V) &= \frac{1}{(1+exp(-(V-V_{1/2})/Z)} \\ \tau_m &= 0.15\,ms \end{aligned} \tag{2.70}$$

– kinetics of fast inactivation (Spampanato et al., 2004)

$$\begin{aligned} V_{1/2} &= -60\,mV \\ Z &= 7.7\,mV \\ \tau_{corr,Na} &= 0.25 \\ h_\infty(V) &= \frac{1}{(1+exp(-(V-V_{1/2})/Z)} \\ \tau_h(V) &= \tau_{corr,Na} * 20.1 * exp(-0.5(V+61.4)/32.7)^2 \end{aligned} \tag{2.71}$$

– kinetics of slow inactivation (Spampanato et al., 2004)

$$\begin{aligned} V_{1/2} &= -60\,mV \\ Z &= 5.4\,mV \\ s_\infty(V) &= \frac{1}{(1+exp(+(V-V_{1/2})/Z)} \\ \tau_s &= 1000 \times (106.7 \times exp(-0.5 \times ((V+52.7)/18.3)^2)) \end{aligned} \tag{2.72}$$

- The **T-type Ca_v3.1** channels were homogeneously distributed (specific conductance $g_{Ca} = 1\ mS/cm^2$) in the soma, dendrite, and axon hillock compartments. Its m (activation) and h (inactivation) gates are defined by $V_{0.5} = -57,\ -81\,mV$ and slopes $z = 6.2,\ 4\,mV$ respectively (Deleuze et al., 2012).

$$
\begin{aligned}
&G_{Ca_V3.1} = g_{Ca} \times m_{Ca}^2 \times h_{Ca} \\
&I_{CaV3.1} = G_{Ca_{V3.1}} \times (V - E_{Ca}) \\
&with\ E_{Ca} = 120\, mV
\end{aligned}
\tag{2.73}
$$

– kinetics of activation (Deleuze et al., 2012)

$$
\begin{aligned}
&V_{1/2} = -57\, mV \\
&Z = 6.2\, mV \\
&m_\infty(V) = \frac{1}{(1 + exp(-(V - V_{1/2})/Z)} \\
&\tau_m = 0.612 + \frac{1}{exp(-(V + 132.)/16.7) + exp(+(V + 16.8)/18.2)}
\end{aligned}
\tag{2.74}
$$

– kinetics of inactivation

$$
\begin{aligned}
&V_{1/2} = -81\, mV \\
&Z = 4\, mV \\
&h_\infty(V) = \frac{1}{1 + exp(+(V - V_{1/2})/Z)} \\
&\tau_h(V) = 28 + exp(-(V + 22)/10.5) \qquad for\ V \geq -81mV \\
&\tau_h(V) = exp((V + 467.)/66.6) \qquad for\ V < -81mV
\end{aligned}
\tag{2.75}
$$

- **L-type Calcium** channel $Ca_{V1.4}$ with $g_{Ca} = 11.9\, mS/cm^2$ presented in terminals. Kinetics of the channels were fitted from (Protti and Llano, 1998).

$$
\begin{aligned}
&I_{Ca} = g_{Ca} \times c^3 \times (V - E_{Ca}) \\
&with\ E_{Ca} = 20\, mV
\end{aligned}
\tag{2.76}
$$

– Dynamic of the channel with variable gate c (Wergniz and Rattay, 2016)

$$
\begin{aligned}
\alpha_c(V) &= -0.4 \times \frac{(V+80)}{exp(-0.1 \times (V+88)) - 1} \\
\beta_c(V) &= 10 \times exp(\frac{-(V+76)}{12.6}) \\
c_\infty(V) &= \frac{\alpha_c}{\alpha_c + \beta_c} \\
\tau_c(V) &= \frac{1}{\alpha_c + \beta_c}
\end{aligned}
\tag{2.77}
$$

- **Hyperpolarization-activated cyclic nucleotide-gated (HCN) channels:** HCN type one (HCN1) channels are at the terminals and the current fit is based on (Zhang et al., 2000), leading to $g_{HCN} = 3.52\, mS/cm^2$ and

$$
\begin{aligned}
&I_{HCN} = g_{HCN} \times y \times (V - E_{Na}) + g_{HCN} \times y \times (V - E_K) \\
&with\ E_{HCN} = -40\, mV
\end{aligned}
\tag{2.78}
$$

  - Dynamics of the channel with variable gate y

$$
\begin{aligned}
\alpha_y(V) &= exp(\frac{-(V+23)}{20}) \\
\beta_y(V) &= exp(\frac{(V+130)}{10}) \\
y_\infty(V) &= \frac{\alpha_y}{\alpha_y + \beta_y} \\
\tau_y(V) &= \frac{1}{\alpha_y + \beta_y}
\end{aligned}
\tag{2.79}
$$

- The **potassium channels** are the same as the channels in section 2.5.1.

Kinetics of the channels in SMC

The SCM has a surface area the same as the real cell i.e. $650\ \mu m^2$. All ion channels present in the MCM are available with the same kinetics but with averaged conductivities of $g_{Na} = 23.52$, $g_{Kfast} = 0.1$, $g_{Kslow} = 1.83$, $g_{Ca3.1} = 0.76$,

$g_{Ca1.4} = 0.38$ and $g_{HCN1} = 0.11\, mS/cm^2$.

Kinetics of the channels in TMC

The TCM is made of a somatodendric compartment and a terminal connected together via a resistance playing role of the axon, Fig 2.8. The TCM surface has the total surface equal to the MCM, 650 μm^2. In the model, soma surface is 512 μm^2 and the terminal surface is 138 μm^2 since the geometry of Fig 2.9 was divided at the center of the axon and add half of the axon surface, 21.5 μm^2, to the soma. Axon length and diameter are 27.3 and 0.5 μm. The same as MCM, the K_{slow} and $Ca_v3.1$ channels are located in the somatodendric compartment with averaged conductances of 2.32 and 0.96 mS/cm^2, respectively. The other conductances of $Na_v1.1$, K_{fast}, $Ca_v1.4$ and $HCN1$, all of which located at the terminal, are 110.95, 0.475, 1.81 and 3.535 mS/cm^2. The kinetics of the ion channels are also the same as the MCM.

Kinetics of the channels in FMC

The FCM is made of four cylindrical compartments, each of which represents dendrites, soma, axon, and terminals. The surface area of each compartment is the same as the total surface area of all compartments making that cell region in the MCM. The diameters of the compartments in FCM are actually the average of the diameters of all MCM compartments making each region. The areas of dendrite, soma, axon, and terminal are respectively 135.45, 355.13, 138.39, and 20.8 μm^2, with the diameters 0.6, 10.7, 0.62, and 0.6 μm. Since shape of the compartments is cylinder, the compartment lengths are easilly calculated from the surfaces as 72.39, 10.56, 71.04 and 11.03μm, respectively. The $Na_v1.1$ and K_{fast} channels are at the axon with conductances of 110.5, and 0.47 mS/cm^2, respectively. $Ca_v3.1$ and K_{slow} channels are on the soma and dendrite with conductances of 1.0 and 2.4 mS/cm^2. Finally, $Ca_v1.4$ and $HCN1$ channels are located at the terminal with the same conductances used in the TCM.

2.7 Ribbon synapse model

Output of retinal bipolar neurons has two components; transient and sustained outputs, that is unique between most of the neurons. The uniqueness originates from existence of an extra protein structure called 'ribbon'. A synaptic ribbon is a protein structure perpendicular to the active zones (Sterling and Matthews 2005; Matthews and Fuchs, 2010; Schmitz, 2009) characterized by rows of connected vesicles on each of its two faces (Maxeiner et al., 2016 ; Singer and Diamond 2006). Ribbons have been found in hair cells of the cochlea and vestibular organ (Wersall et al., 1965; Smith and Sjostrand, 1961), retinal PRs and BCs (Kidd, 1962; Dowling and Boycott, 1966; Sjostrand, 1953, 1958), electroreceptors and lateral line receptors of fish and pinealocytes (Wachtel and Szamier, 1966; Hama, 1965; Vollrath and Huss, 1973), as well as some neuromuscular junctions (Kosaka and Ikeda, 1983; Katz et al., 1993). Shape of ribbons varies from planar, in PRs (Sterling and Matthews 2005), whether platelet, in BCs (Graydon et al., 2014), to spheroid, in hair cells (tom Dieck and Brandstaetter 2006), and T-shape, in drosophila PRs (Prokop and Meinertzhagen 2006).

RBC receive input from rod PRs (Dowling and Boycott, 1966) and put their outputs on AII and A17 amacrine cells at their axon terminals (Famiglietti and Kolb, 1975; Nelson and Kolb, 1985). From the morphological point of view, RBCs are the simplest BC types because of a poorly branched dendritic tree and usually not more than three terminal branches. These features allowed easily to simulate 3D morphology of a rat RBC from its 2D depiction in ref (Oltedal et al., 2009) with a good accuracy by Encke's method. In the method, positions and local diameters of the neuron parts are determined from the 2D image and the missing coordinates of the third dimension is estimated through a normally distributed random function (Encke et al., 2013); Fig 2.10. After reconstruction, the cell has total surface area of 525 μm^2, this area of which, portions of dendrite, soma, and axon + terminal are 100, 254, 170 μm^2, respectively, the same as the numbers already presented in (Oltedal et al., 2009).

Paired-pulse voltage-clamp recording from a synaptically connected RBC and

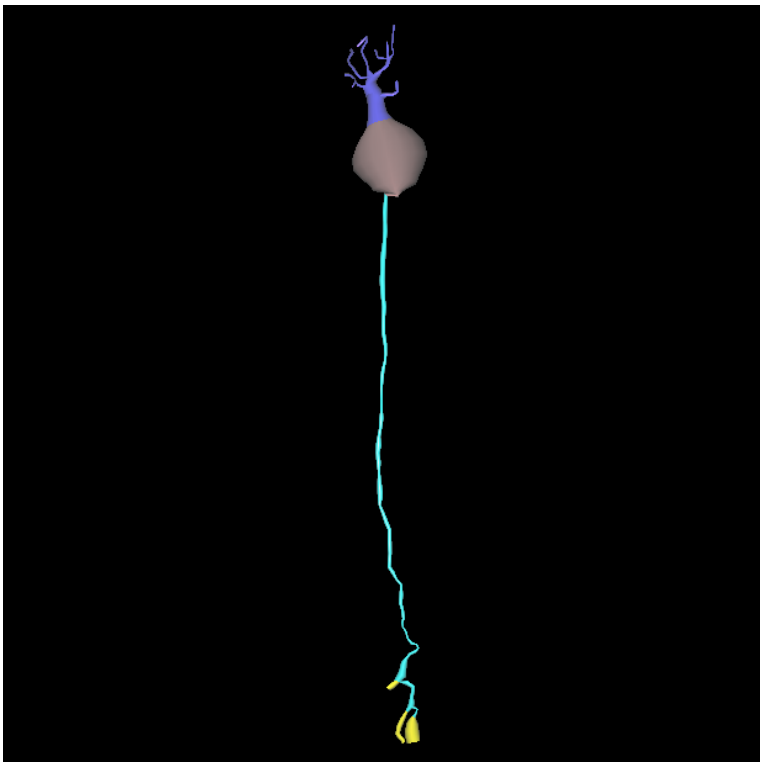

Figure 2.10: **3D model of a rat RBC.** The cell consists of 151 cylindrical- compartments, 9 of which belong to the soma highlighted in gray, 85 compartments make the axon (cyan), 14 out of 85 are the axon terminals (yellow), and finally 57 dendritic compartments (blue). Diameters in axonal, terminal and dendritic compartments vary between 0.11-1.3 μm, while in soma between 0.3-5.2 μm and the total length of the cell is 98.7 μm in z direction.

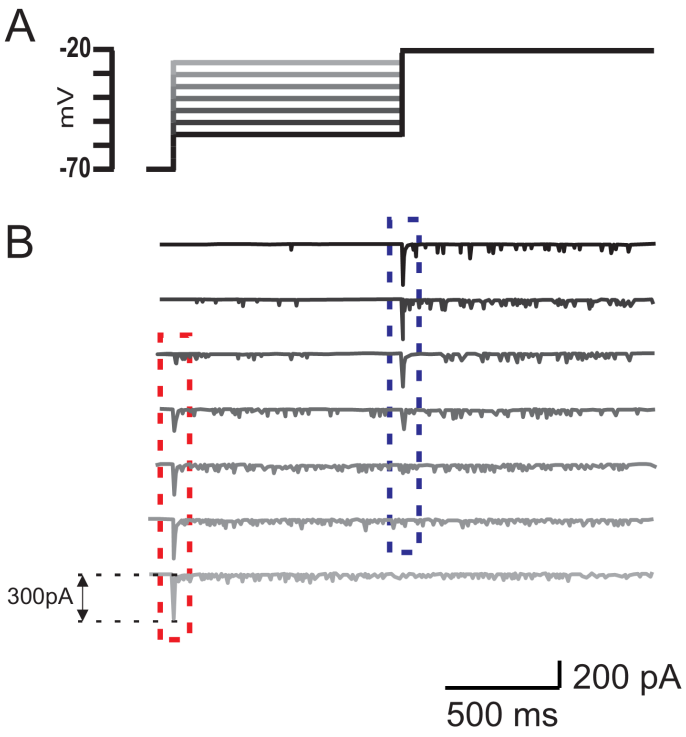

Figure 2.11: **Vesicle release from a rat RBC visualized in a synaptically coupled RBC-AII pairs experiment.** RBC is maintained at -70 mV then stepped to specific voltages; from -55 mV to -25 mV for 1 s with voltage step of 5 mV and then jumps to -20 mV lasting also for 1 s (A), while EPSCs of the AII cell are recorded simultaneously (B). Thus, amplitudes of AII EPSCs are proportional to the number of vesicles released from the RBC. Any large enough change in transmembrane voltage of RBC causes a rapid response in AII cell showing the transient vesicle release, highlighted in dashed red and blue windows. Sustained vesicle releases also are the low amplitude EPSCs taken place in any transmembrane voltage with a specific rate. The strongest amplitude of 300 pA corresponds to total depletion of all previously full RRPs containing 55 vesicles in total. This case (lowest line in B) corresponds to a first step to -25mV and is without a second transient respond for the step to -20 mV. The diagram was replotted from (Oesch and Diamond 2011, Fig 3a).

an amacrine cell allowed to quantify RBC's vesicle release from the EPSC of the AII (Oesch and Diamond 2011). Several key parameters of the proposed model are based on this technique. In the experiment, the transmembrane voltage of a rat RBC increases from -70 mV to other potentials with step voltage of 5 mV for one second followed by another second voltage step fixed at -20 mV, Fig 2.11. The recorded EPSCs of the AII, Fig 2.11 B, are closely related to the number of released vesicles from the RBC. When transmembrane voltage of RBC changes from -70 mV to any value more than -45 mV, a current enters AII cell referring to transient release of vesicles from RBC (Fig 2.11 B, highlighted in dashed red window). Voltage step changes from -70 mV to -55 or -50 mV causes no EPSC in the AII that means no transient vesicle has been released from the RBC. Transient vesicle releases are also seen when the transmembrane voltage of the RBC changes to -20 mV from other potentials (Fig 2.11 B highlighted in the dashed blue window) and the number of transient released vesicles increased with the first voltage step. RBC voltage change from -25 to -20 mV shows no transient release that means the RRP becomes empty when voltage of RBC changes from -70 mV to -25 mV. In spite of transient release, sustained release is seen for each arbitrary voltage with a specific rate, EPSCs between dashed red and blue windows represent the sustained releases. Rates of sustained release depends on the terminal transmembrane voltage of the cell.

Here, the standard value for the pool size RRP is 10 (Graydon et al., 2014). Assuming a maximum of 10 vesicles in every RRP of a RBC ribbon and considering total size of the RRPs equal to 55 (Oesch and Diamond, 2011) lead to 5.5 ribbons in a RBC as an average value. Maximum AII EPSC amplitude of 300 pA according to RBC voltage change from -70 to -25 mV, Fig 2.11 B, corresponds to the release of all 55 RRP vesicles. According to dashed red window in Fig 2.11 B, the transient EPSCs are 0, 0, 58, 147, 209, 274, 300 pA respectively when RBC voltage changes from -70 mV to -55, -50, -45, -40, -35, -30, -25 mV that leads to total transient vesicle release of 0, 0, 11, 27.5, 38.5, 49.5, 55 for relevant voltage shift. Each of transient release is done as a single event in a time unit. By dividing total transient vesicle release numbers to 5.5, the number of tran-

siently released vesicles for a single ribbon would be governed as 0, 0, 2, 5, 7, 9, 10 respectively for the related transmembrane voltage change.

In the presented release and refill models, in addition to transient and sustained releases, there are two types of vesicle feeding; refill and recovery.

2.7.1 MODEL V: a vesicle release and refill model based on terminal transmembrane voltage

According to the experiment of Fig 2.11, a simple release and refill model will be developed in the following based on terminal transmembrane voltage $V_T(t)$ as input parameter. Beside transient and sustained release, two temporal components are included that are refill and recovery. Each of the terms is explained bellow in details.

- **Transient release**

  The transient vesicle release refers to the number of released vesicles from the pool RRP that are released rapidly upon depolarization. As mentioned above, RBC voltage change from -70 mV to -55, -50, -45, -40, -35, -30, -25 mV respectively leads to release of 0, 0, 2, 5, 7, 9, 10 transiently vesicles from a single ribbon in a time unit. Figure 2.12 shows a fitted step function to this data where the steps are defined as

$$TR(V_T) = \begin{cases} 0 & \text{if } V_T \leq -50 \\ [-0.000223(V_T)^3 - 0.0351(V_T)^2 - 1.23V_T - 2] & \text{if } -50 \leq V_T \leq -20 \\ 10 & \text{if } V_T > -20 \end{cases} \tag{2.80}$$

  where [] is the floor function; a function that takes a real number X as input and produces the greatest integer less than or equal to X as output, necessary to bring an integer concept for number of released vesicles. The relation showing number of transiently released vesicle during a single time step Δt when transmembrane voltage of terminal changes from $V_T(t)$ to

$V_T(t + \Delta t)$ is simulated as

$$TR(V_T) = \begin{cases} TR(V_T(t + \Delta t)) - TR(V_T(t)) & \text{if } V_T(t + \Delta t) > V_T(t) \\ 0 & \text{else} \end{cases} \tag{2.81}$$

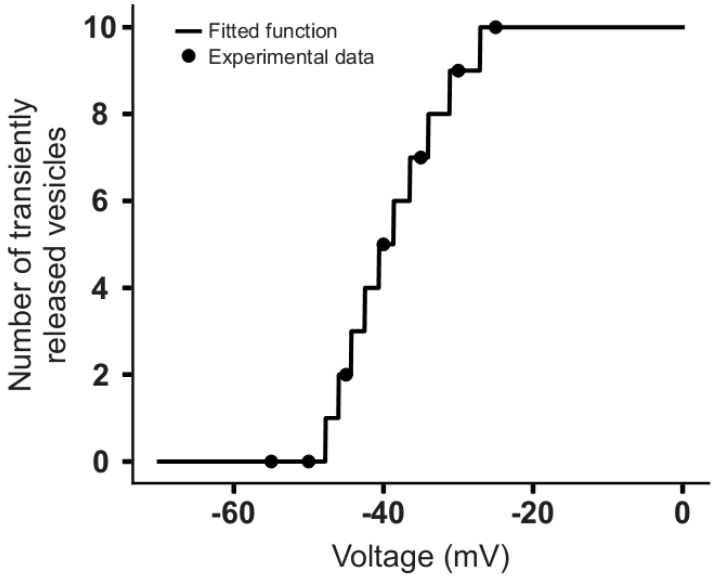

Figure 2.12: **Number of transiently released vesicles from a single ribbon among voltage change from -70 mV.** Circles represent experimental data of 2.11 B and the solid line is the fitted function, Eq. 2.80, showing each voltage step that causes one additional vesicle to be released.

- **Sustained release**

  In comparison to transient release, sustained vesicles are released in essentially larger time intervals through stochastic events but with specific rates (number/second). To find the rates for one ribbon, we used Fig 2.13, redrawn from ref (Oesch and Diamond, 2011, Fig 3c). Integration over the EPSC- time diagrams exhibits the amount of charges coming to the AII cell that is proportional to the amount of released neurotransmitters. Rescaling the diagrams by 1/5.5 in order to find the amount of charge originating from a single ribbon and once again by 1/0.36 to put size of the RRP equal

10 shows the cumulative vesicles release versus time from a single ribbon, Fig 2.13. Figure 2.13 shows both transient and sustained releases; transient releases are taken place rapidly after depolarization and vesicle release continues afterwards with linear rates showing sustained releases. Thus, the slope of each diagram shows average number of sustained released vesicles per second at each transmembrane voltage. Then, by fitting a function to steady state of the $I_{ca}(V)$ diagram, $I_{Ca}(V_T) = c_\infty^3(V_T - E_{Ca})$, sustained vesicle release rate becomes a function of terminal voltage. We preferred to explain sustained release rate based on $I_{ca}(V)$ because vesicle release is stopped as soon as the terminal transmembrane voltage reaches to the calcium Nernst potential or pass through that (Werginz and Rattay, 2016). According to Fig 2.13 and Eq. 2.60 sustained release rate is

$$Sus(V_T) = 1.3c_\infty^3(V_T - E_{Ca}) \tag{2.82}$$

where c_∞ is the steady state of the gate at voltage V, and 1.3 is a number used for normalizing the rates for a standard ribbon with 10 vesicles in RRP at initial with dimension of $vesicle.s^{-1}.mV^{-1}$. α and β are explained at Eq. 2.60.

To consider the stochastic release, an equally distributed random number between $(0, 1000]/\Delta t$ is generated at each time step Δt, $\Delta t = 1\ ms$, by $F_{Sustained}(t, V_T)$ compared to the related value in $Sus(V_T)$, if this number is less than the related number in $Sus(V_T)$, a vesicle is released from the pool, otherwise, not. The number 1000 is actually used to change the second dimension to millisecond. The maximum release rate 45 $vesicles.s^{-1}$, Fig 2.13 C, means an average time between two releases is 22.22 ms. Thus, a time step $\Delta t = 1\ ms$ seems to be appropriate. The sustained release is simulated as

$$F_{sustained}(t, V_T) = \begin{cases} 1 & \text{if } random1 \leq Sus(V_T) \\ 0 & \text{if } random1 > Sus(V_T) \end{cases} \tag{2.83}$$

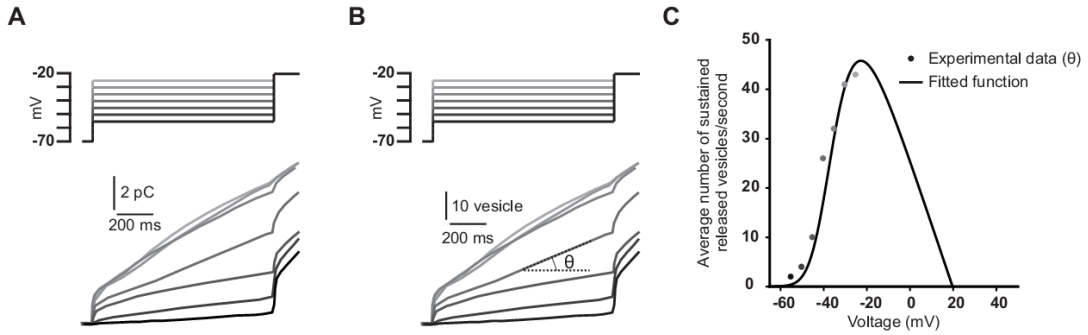

Figure 2.13: **Rate of charge coming to the AII cell represents a criterion for sustained vesicle release.** (A) Amount of charge coming to the AII cell versus time. The diagram was replotted from ref (Oesch and Diamond 2011,Fig 3c) actually obtained by integrating AII EPSC traces of Fig 2.11 B. (B) Cumulative vesicle release versus time from a single ribbon obtained by dividing diagrams in A once to 5.5 and once to 0.36 pC. Slope of each diagram, Θ, defines average number of sustained released vesicles per second for a standard ribbon with 10 vesicles in RRP at initial. Voltage protocols shown in the top of A and B represent the voltages in which the RBC is clamped according to, Fig 2.11 A. (C) Circles correspond to the slopes of the lines in B using the same gray intensity and the solid line is the fitted function based on Eq. 2.82.

- **Refill**

  The RRP should be fed via the same rates as sustained releases since rate of sustained vesicle release remains constant at each transmembrane voltage even when the pool is empty, the pool is empty when the transmembrane voltage reaches to -25 mV from -70 mV and stays at -25 mV for one second; see Fig 2.11 and Fig 2.15. Thus, the same strategy as sustained release is applied for refiling process. In the refilling process, a random number, between $(0, 1000]/\Delta t$, is generated in each time step then is compared with the related number in $Sus(V_T)$, if the random number is less than the related number in Sus(V), one vesicle is injected to the pool; otherwise, not. The refill process is explained by $F_{Refill}(t, V_T)$ as follow

$$F_{Refiil}(t, V_T) = \begin{cases} 1 & \text{if } random2 \leq Sus(V_T) \\ 0 & \text{if } random2 > Sus(V_T) \end{cases} \tag{2.84}$$

  Two series of random numbers, random1 and random2, are generated by

$F_{Sustained}(t, V_T)$ and $F_{Refill}(t, V_T)$ for the same time step to consider the independency between refill and release terms.

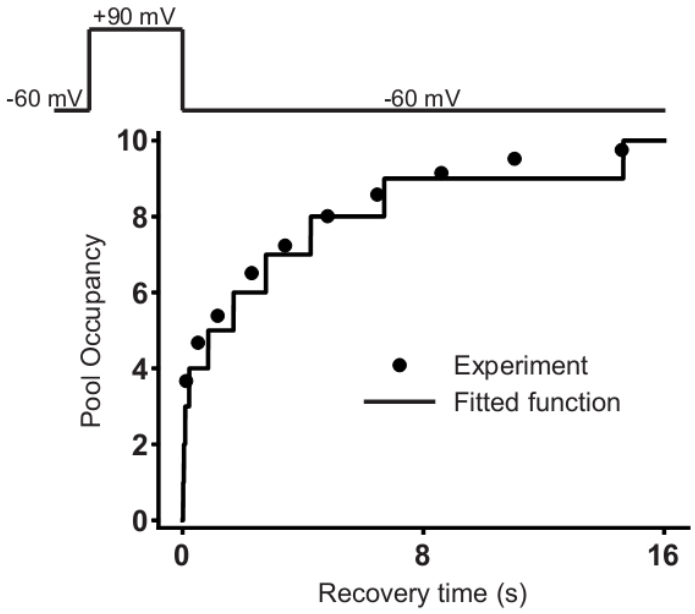

Figure 2.14: **Recovery time of the RRP based on a double pulse experiment.** The transient response of the second pulse (not shown in the stimulus) depletes the pool again and thus the corresponding number of released vesicles defines the number of vesicles in RRP during recovery. Black circles show the number of incoming vesicles until the second pulse is applied; replotted from (Singer and Diamond, 2006, Fig 5). The solid line is the fitted function plotted by $F_{Recovery}(t, V_T)$. Although 40% of the RRP is recovered during only $\approx$ 120 ms time interval, it takes $\approx$ 15 s for complete refilling.

- **Recovery**

  Needed time for the RRP to become full again is called 'recovery' time. Recovery time was investigated also in two paired-pulse experiments (Singer and Diamond 2006, Fig 5) where the RBC was stepped from -60 mV to +90 mV, to make the RRP pool empty, then stepped again to -60 mV causing recovery without any sustained release. Then for different time intervals the cell was stepped again to +90 mV while simultaneously the AII EPSC was measured. To find the recovery term, a function to the data from this double pulse experiment was fitted. Circles in Fig 2.14 show the replotted

experimental data and the solid line represents the modelled recovery time explained by the following equation:

$$F_{Recovery}(t, V_T) = \begin{cases} 0 & \text{if } V_T > -60\,mV \\ [0.15 - 3.6e^{-t/60} - 6.4e^{-t/3900}] & \text{if } V_T \leq -60\,mV \end{cases} \tag{2.85}$$

where [] is the floor function as already explained.

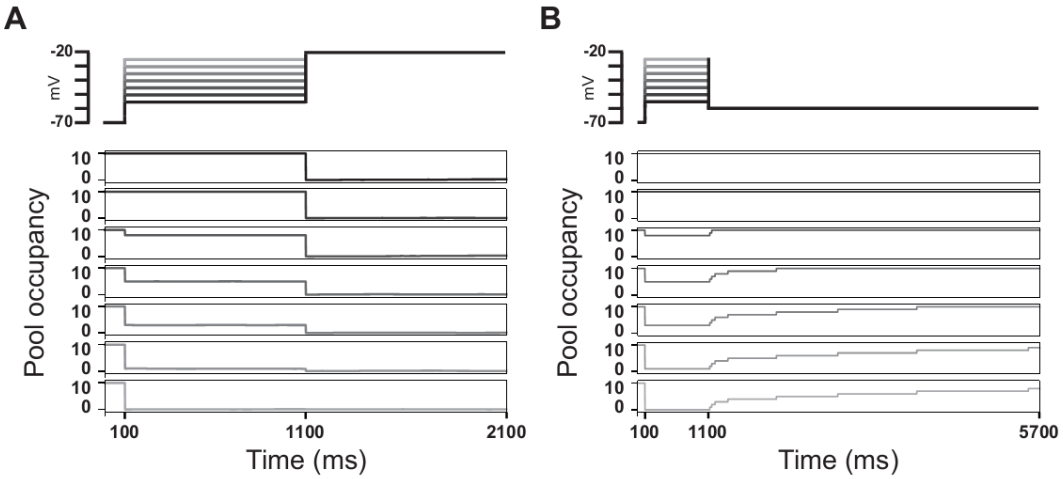

Figure 2.15: **Pool occupancy continuously varies with changing of transmembrane voltage of RBC.** A) Schematic of the voltage protocol used in the paired-pulse recordings in Fig 2.11 A (top) and the related RRP occupancy versus time (bottom). B) Schematic of the voltage protocol used in A except for being stepped to -60 mV instead of -20 mV (top) and the related RRP occupancy versus time (bottom). The RRP starts being recovered as soon as the terminal transmembrane voltage reaches to its resting membrane potential; -60 mV, in different time intervals dependent on previous state of pool occupancy.

- **A mathematical framework for occupancy of the RRP**

  The equation explaining the occupancy of the RRP versus time is made of four terms $F_{Sustained}(t, V_T)$, $F_{Refill}(t, V_T)$, $F_{Transient}(t, V_T)$, $F_{Recovery}(t, V_T)$ that respectively stand for sustained vesicle release from the RRP, vesicles coming to the pool, rapid (transient) vesicle release and recovery. The equation is

$$\frac{\Delta RRP}{dt} = F_{Sustained}(t, V_T) + F_{Refill}(t, V_T) - F_{Transient}(\Delta V_T) + F_{Recovery}(t, V_T) \tag{2.86}$$

The terms showing vesicle release from the pool are marked with negative signs and the terms showing entrance of vesicles to the pool are marked with positive signs. Pool occupancy versus time is shown in Fig 2.15 A for the voltage protocol used in Fig 2.11 A, here average of N=10000 trials was used to reduce the stochastic influence. When the RBC transmembrane voltage jumps from -70 mV to -55 mV and -50 mV, the pool remains full, jumping to -45 mV makes 20% of the pool empty and this number decreases to 50%, 80%, 90%, and 100% for voltage jumping to -40, -35, -30, and -25 mV, respectively. Afterwards, when the voltage reaches to -20 mV, the pool again becomes empty. Fig 2.15 B shows the recovery time of the pool. The ribbon sends vesicles to the pool as soon as the cell reaches its resting membrane potential; -60 mV, or hyperpolarizes more (less than -60 mV), Fig 2.14. The pool becomes full in different time intervals dependent on the previous occupancy state of the pool. In other words, the more the pool is empty, the more time it needs to become full. For example, it takes only 48 ms to get full when the cell is stepped from -45 to -60 mV as the pool was 80% full. The other time intervals for the states of -40, -35, -30, and -25 mV to become full are 0.96, 2.9, 6.6, 15 s, respectively.

As refilling and sustained release terms obstruct each other's effect for trials, which is usually more than N=1000 trials, the number of transient vesicles released from the RRP is actually result of RRP occupancy change for when the change is negative, while positive RRP occupancy change shows RRP recovery. So number of released vesicles (NRV) from the RRP at time t when the terminal membrane voltage is V_T is governed by RRP occupancy changes plus the term showing sustained release

$$\begin{aligned} NRV(t, V_T) &= -\Delta RRP(t, V_T)|_{t=t_0} + F_{sustained}(t, V_T) \\ and\, \Delta RRP(t, V_T))|_{t=t_0} &= RRP(t_0, V_T) - RRP(t_0 - T_0, V_T) \end{aligned} \tag{2.87}$$

where $\Delta RRP(t, V_T)$ stands for RRP occupancy changes at time t that is average of N=10000 trials, T_0 and t_0 stand for the time in which the RRP occupancy starts and stop decreasing, respectively. Note that, when $\Delta RRP(t, V_T)$ is less than zero some vesicles have left the pool and when it is positive, some vesicles has been injected to the pool; recovery process. T_0 would be so small for voltage clamp experiments since the membrane voltage changes fast in these experiments, but larger for the cases in which the terminal membrane voltage depolarizes via spike or non-spike stimulations. $F_{Sustained}(t, V_T)$ is the sustained vesicle release term from the RRP explained by Eq. 2.83. Figure 2.16 shows the results of Eq. 2.87 for the protocol of Fig 2.11 A, using a time step $\Delta t = 1\, ms$ and $T_0 = 1\, ms$.

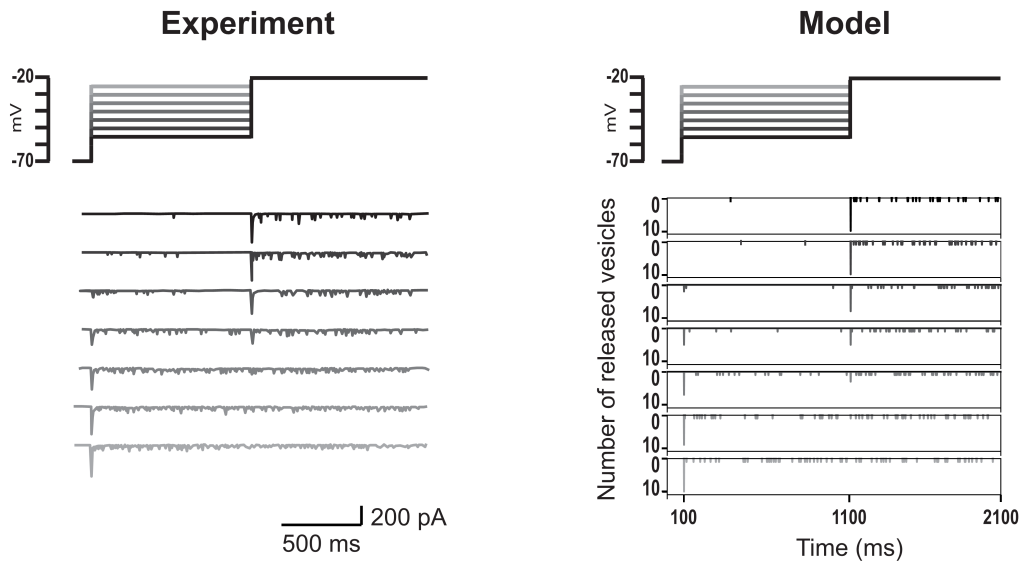

Figure 2.16: **Comparison of coupled RBC-AII paired-pulse experiment of Fig 2.11 and number of released vesicles simulated for a single ribbon.** Transient and sustained releases show the same characteristics; e.g. the weakest pulse (darkest black) causes a single released vesicle (sustained) and no transient release, but all 10 vesicles of the pool are transiently released at the beginning of the second strong stimulus, -20 mV.

2.7.2 ModelCa: a vesicle release and refill model based on intracellular calcium concentration

A possible step to improve the release model is considering the calcium concentration in the terminal as the key parameter. Vesicle release depends on the degree of depolarization of membrane of axon terminals that control voltage-gated calcium channels. In BCs these are mainly L-type channels, located linearly parallel to the bottom surface of the ribbon. Intracellular calcium concentration $[Ca^{2+}]$ depends on calcium current across the terminal membrane, surface area and volume of the terminal (A, V) and a decay time constant τ (Fohlmeister et al., 1990)

$$\frac{d[Ca^{++}]_i}{dt} = -\frac{Ai_{Ca}}{2VF} - \frac{[Ca^{++}]_i - [Ca^{++}]_{res}}{\tau_{Ca}} \tag{2.88}$$

where $F = 96485.33\, C.mol^{-1}$ is the Faraday constant, $[Ca^{2+}]_{rest}$ is the initial calcium concentration set to $0.34\,\mu M$ and $\tau = 10\,ms$ (Werginz and Rattay 2016), time step $dt = 10\,\mu s$ was used for solving this equation.

For terminal voltage <-60 mV, there is no calcium current flow, but onset of depolarization causes inward calcium current flow Fig 2.17 A, B. Inward calcium current reaches a maximum after a while if terminal transmembrane voltage remains constant. Increment of the calcium current results in increasing of intracellular calcium concentration to a steady state value (maximum value) Fig 2.17 C. Thus, a specific intracellular calcium concentration value is referred to each transmembrane voltage. By finding maximum value of calcium concentration for each transmembrane voltage, the corresponding sustained release rate is easily obtained by help of Fig 2.13 C, and can be fitted as following; see Fig 2.18,

$$Sus([Ca^{2+}]) = 56.59 - \frac{0.52 + 56..59}{1 + (\frac{[Ca^{2+}]}{20.14})^{0.84}} \tag{2.89}$$

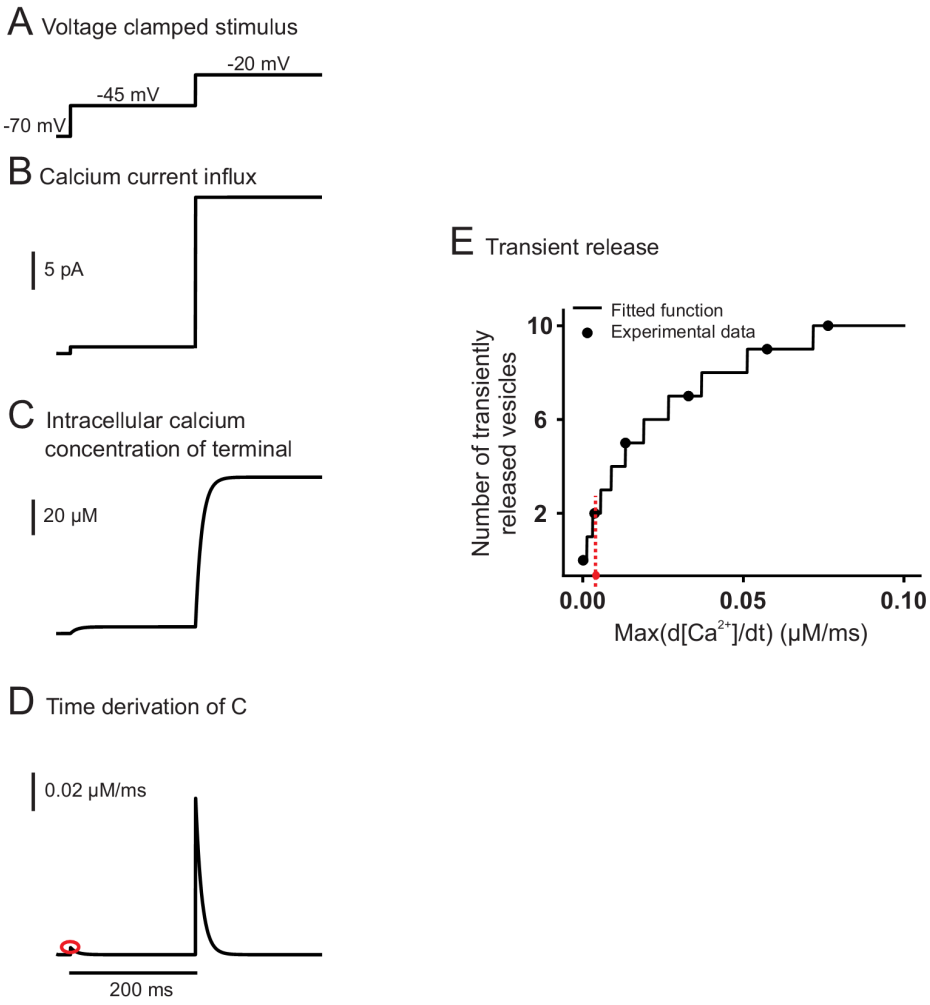

Figure 2.17: **Intracellular calcium concentration changes as a criterion for transient release.** (A) Voltage clamped stimulus is increased 2 times for 25mV. (B) L-type calcium current, shown with positive sign, is much larger for the second step which is a consequence of gating variable c. (C) Intracellular calcium concentration with initial intracellular calcium concentration of 0.34 μM calculated by Eq. 2.88. (D) Intracellular calcium concentration changes versus time, i.e. time derivation of C. (E) Number of transiently released vesicles versus local maximum points of D (circles), and fitted function obtained by Eq. 2.93. According to Fig 2.11 B, transmembrane voltage change from -70mV to -45m causes to release of 2 transient vesicles, maximum of calcium concentration change during the same voltage change is $0.004 \mu M/ms$ which are shown as red circles in D and C. The dashed red line in E explains that $0.004 \mu M/ms$ would release of two vesicles.

where 20.14 has dimension of μM, 1 and 0.84 are dimensionless numbers, and 56.59 and 0.52 have dimension of $vesicle/s$.

The stochastic release process (sustained release vesicle) can be simulated as

$$F_{sustained}(t,[Ca^{2+}]) = \begin{cases} 1 & \text{if } random1 \leq Sus([Ca^{2+}]) \\ 0 & \text{if } random1 > Sus([Ca^{2+}]) \end{cases} \tag{2.90}$$

where $F_{sustained}(t,[Ca^{2+}])$ works like $F_{sustained}(t,V_T)$. In other words, a random integer number between $(0,1000]/dt$, $dt = 0.01\ ms$, is generated at each time step by $F_{sustained}(t,[Ca^{2+}])$, all of the numbers in the interval has the same probability to be chosen, compared to the related value in $Sus([Ca^{2+}])$, if this number is less than the related number in $Sus([Ca^{2+}])$, one vesicle is released from the pool, otherwise, not.

Refilling process can be calculated with the same algorithm as sustained release:

$$F_{Refiil}(t,[Ca^{2+}]) = \begin{cases} 1 & \text{if } random2 \leq Sus([Ca^{2+}]) \\ 0 & \text{if } random2 > Sus([Ca^{2+}]) \end{cases} \tag{2.91}$$

Again to show independency of generated random numbers in $F_{sustained}(t,[Ca^{2+}])$ and $F_{Refill}(t,[Ca^{2+}])$ we show them by random1 and random2.

The recovery process is simulated with the same formalism as Eq. 2.85:

$$F_{Recovery}(t,[Ca^{2+}]) = \begin{cases} 0 & \text{if } [Ca^{2+}] > 0.34\ \mu M \\ [0.15 - 3.6e^{-t/60} - 6.4e^{-t/3900}] & \text{if } [Ca^{2+}] \leq 0.34\ \mu M \end{cases} \tag{2.92}$$

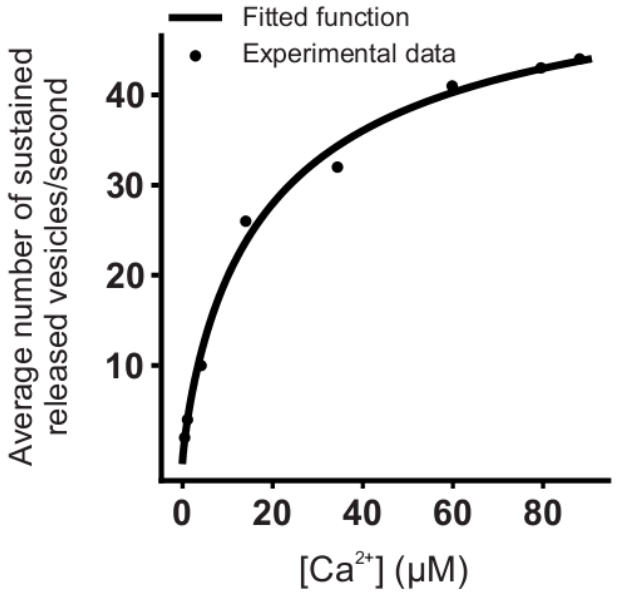

Figure 2.18: **Rate of sustained released vesicle as a function of intracellular calcium concentration.** Steady state intracellular calcium concentration as in the example of Fig 2.17 C is fitted to the experimental data from ref (Oesch and Diamond 2011) observable also from Fig 2.13 C. Circles show the relation. Solid line is the fitted function by Eq. 2.89.

By calculating time derivation of intracellular calcium concentration, Fig 2.17 D, a criterion for transient vesicle release is appeared. Local maximum points of intracellular calcium concentration changes would correspond to number of transient vesicle release for any change in terminal voltage , Fig 2.17 E by help of Fig 2.12. For example, when the terminal voltage changes from -70mV to -45mV; see (Fig 2), two transient vesicles are released. Thus, two-vesicle release is equivalent to $0.004\mu M.s^{-1}$, see red parts in , Fig 2.17 D. The transient release is explained by

$$F_{Transient}(t,[Ca^{2+}]) = 16.2 - \frac{0.43 + 15.96}{1 + (27.02\frac{d[Ca^{2+}](t)}{dt})^{0.75}} \tag{2.93}$$

where 16.2, 0.43, and 15.96 have dimension of $Vesicle.s^{-1}$, 1 and 0.75 have no dimension. 27.02 is a normalizing number with dimension of $s.\mu M^{-1}$. [] is the floor function as already discussed. To find the transient release versus time,

the times in which the local maximum points are taken place (T_1, T_2, T_3,...) are extracted at first, these points are roots of second time derivation of intracellular calcium concentration and show the times in which the transient releases are taken place. Using indicator function χ_{T_i} and other terms already explained, RRP occupancy versus time would be

$$\begin{aligned}\frac{dRRP}{dt} &= -F_{Sustained}(t,[Ca^{2+}]) + F_{Refill}(t,[Ca^{2+}]) \\ &\quad -\chi_{T_i}F_{Transient}(t,[Ca^{2+}]) + F_{Recovery}(t,[Ca^{2+}])\end{aligned} \tag{2.94}$$

where T is a set containing the times at which the local maximums points of time derivation of intracellular calcium concentration are taken place. Time step $dt = 10\,\mu s$ was used for solving this equation.

Number of released vesicles at time t will be governed by solving

$$\begin{aligned}NRV(t,[Ca^{2+}]) &= -\Delta RRP(t,[Ca^{2+}]) + F_{Sustained}(t,[Ca^{2+}]) \\ \Delta RRP(t,[Ca^{2+}]) &= RRP(t,[Ca^{2+}]) - RRP(t-dt,[Ca^{2+}]) \\ &\quad if\ \ \Delta RRP(t,[Ca^{2+}]) < 0\end{aligned} \tag{2.95}$$

Although we used a special kinetics for calcium ion channels, any type of kinetics can be used with the same mechanism without affecting generality of the problem. Figure 2.19 show experimental data versus data calculated by this equations.

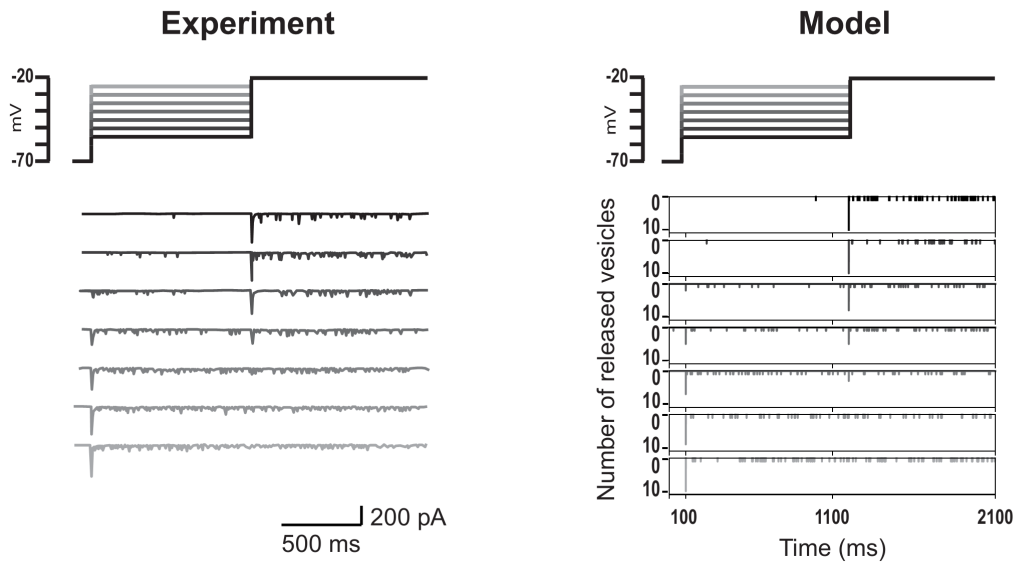

Figure 2.19: **The model based on intracellular calcium concentration.** (Left) Experimental data from Fig 2.11. Right) The data modeled by Eq. 2.95 showing number of released vesicles versus time from the pool.

Chapter 3

DB4 Bipolar cell with sphere soma

This chapter answers different questions regarding the behavior of BCs to specially extracellular stimuli. Some of the questions are directly related to the biophysical properties of BCs like ion channel distribution and some others involved in position of the electrode in relation to the cell. The position of the electrode determines de- and hyperpolarizing effects along the neuron. One of the main interesting result in this chapter is the electrical effects at the ends of the neurites. Although the effects are negligible in large configurations (far from the stimulating electrodes), on a small structure such as BCs they play a vital role in signal transfer. The multi-compartment model explained at section 2.5 was used to do the calculations of this chapter.

3.1 Intracellular versus extracellular stimulation

Current injection to any part of the BC leads to spike generation if the magnitude of the current is large enough. Since sodium channles are located at sodium band, current injection either to soma or sodium band results in generating spike first in the sodium band, Fig 3.1. The small size of the cell, 61 μm, in axial direction results in fast transision of the generated spike to the terminals observable in voltage curves of sodium band and terminals, Fig 3.1. Since the ratio of surface of

sodium-band to the surface of soma, (surface of sodium-band)/(surface of soma), is so small, the generated spike amplitude recorded in soma and dendrite are much less than the recorded signals in terminal and axon. The signal also has a delayed peak at the soma and dendrite. In addition to the surface ratio, the smaller number of sodium channels in the BC in comparison to GC or PC (Table 2.1) cannot charge the large capacitance of the soma with enough axonal current to generate a somatic spike with the same amplitude as sodium band spike.

Since potassium channels are activated only when the membrane depolarizes, so anodic intracellular stimulation does not hyperpolarize any part of the cell Fig 3.1 a, but cathodic extracellular stimulation makes some parts of the cells depolarized and some other parts hyperpolarized, Fig 3.1 b-left. Changing the electrode polarity from cathodic (Fig 3.1 b-left) to anodic (Fig 3.1 b-right) makes the hyperpolarized regions depolarized (and vice versa). For example, the hyperpolarized dendrites (left upper part in Fig 3.1 b) become the most depolarized compartments of the cell when stimulus pulse polarity changes (right upper part in Fig 3.1 b).

One of the most important result is spike generation while shifting the electrode position from sodium band to the soma, which is somehow small distance. In this shift, it is necessary to change the pulse polarity of the electrode (compare Fig 3.1 b). Another important point is the way that the spike is generated in the sodium band when the electrode is above the sodium band. In this case, a cathodic stimulation is needed. This is demonstrated from the first moment of stimulation where the sodium band, which is shown by the purple curve, is always the most depolarized segment (upper case in Fig 3.1 b), but the terminal, which are shown by red curves, is depolarized (lower right case in Fig 3.1 b) for anodic stimulation that finally activates the sodium band by intracellular current flow.

3.1.1 Bipolar cells versus ganglion and pyramidal cells

Although both BCs and GCs are retinal neurons, there are some differences from morphological point of view. GCs have a larger soma diameter, larger dendrites, and a very long axon with a longer sodium band in comparison to BC. A standard

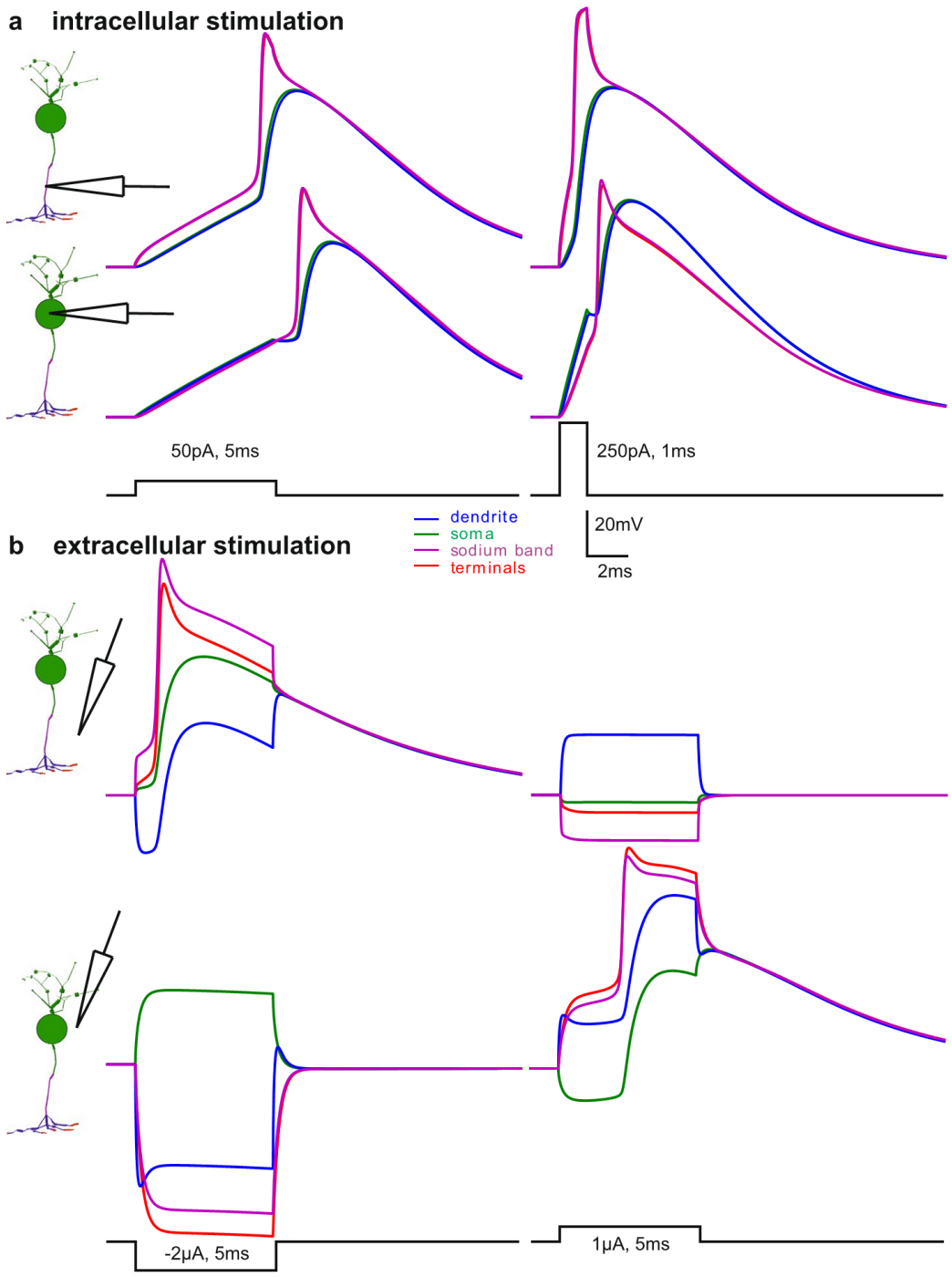

Figure 3.1: **Transmembrane voltages for intracellular and extracellular stimulations of DB4 BC.** a) The spike initially is generated in the sodium band and then propagates to the soma and dendrite with short delay and smaller spike amplitude. b) Extracellular stimulation makes some regions hyperpolarized and some others depolarized during stimulation. Electrode distance to cell axis is 10 μm. Resting membrane voltage is $-70\,mV$.

Pulse duration and Injection site	1ms soma	1ms sodium band	10 ms soma	10 ms sodium band
BC	221	151	29	27
GC	758	639	127	127
PC	1000 (4300)	220 (220)	280 (320)	120 (150)

Table 3.1: **Intracellular threshold currents for BC, GC, and PC all in pA.** The PC values are for a 1D cell model as well as 3D model (in brackets); for more details see (Rattay et al., 2012).

neuron like PC is much closer to GCs than BCs. The GC geometry is similar to ref (Rattay, 2014). The simplified cell has a long axon and the dendrite tree of a real cell is replaced by a dendrite having two branches with 300 μm long and parallel to the axon (upper part of Fig 3.2).

Table 3.1 shows intracellular threshold currents for somatic stimulation of the BC, GC and PC. Smaller BC soma diameter ($d = 10.3\,\mu m$) as well as only a few dendrites causes the lower threshold of the BC. Soma diameter in both PC and GC has the same value, 20 μm, but the PC has the larger dendritic tree with many branches close to the soma that results in increasing of the threshold current for spike generation. The PC has less threshold current than the GC when the sodium band is stimulated because of the presence of low threshold $Na_v1.6$ channels in the PC axon (Hu et al., 2009), while low value of BC threshold in this case refers to small size of the sodium band.

Although the BC has lower threshold than GC in intracellular stimulation, it has higher thresholds than that of GC for extracellular cathodic stimulation (solid lines in the lower part of Fig 3.2 for the 20 μm electrode distance). Spike generation in extracellular stimulations does not occur for both polarities in many points near the BC. This is only possible in a small region, 7.5 μm length highlighted in light blue rectangular in 3.2, but there is not such a limitation for the GC and the PC (Figs 3.2 and 3.3). Another special features seen in BC is the threshold between anodic and cathodic pulses in extracellular stimulation. Anodic pulses usually need higher amplitudes than cathodic ones (see for example

GC in Fig 3.2) (Rattay, 1999; Ranck, 1975), but it is vice versa for the BC (Fig 3.2).
Another special feature is seen in PC for a small region where the electrode is above the dendrite and close to the soma (green arrow in Fig 3.3 a). This feature referring to intracellular current flow between the compartments on spike initiation site is discussed in the next subsection and in the discussion.

3.1.2 Spike initiation site

As most parts of the modeled GC have sodium channels with large enough densities, different sites of spike initiation were presented for GC. Thus, spike initiation sites depend on the exact position of the electrode, pulse polarity, and pulse amplitude. How a spike is actually propagated along GCs is explained by considering blocking phenomena (Rattay, 2014; Ranck, 1975). In the GC and BC, spikes were initially generated in the sodium band and the soma. Figure 3.2 shows the thresholds for a cathodic (negative) electrode above the soma of the GC. In this state, the spike is generated within the soma because the distance between electrode and soma surface is so small, 10 μm. Moving the electrode a bit to the left side increases the distance and so the threshold current increases as well. Keep moving the electrode to the left for several micrometers, spike initiation was also observed within the soma, but a larger horizontal shift leads to the axon hillock become closer to the electrode. On the other hand, moving the electrode for more than 10 μm, the hillock is closer to the electrode and sodium channels in the hillock open and axonal current flow results depolarization in the sodium band that lead to an AP peak in the cathodic pulse. This is in accordance with published results (Werginz, et al., 2014).

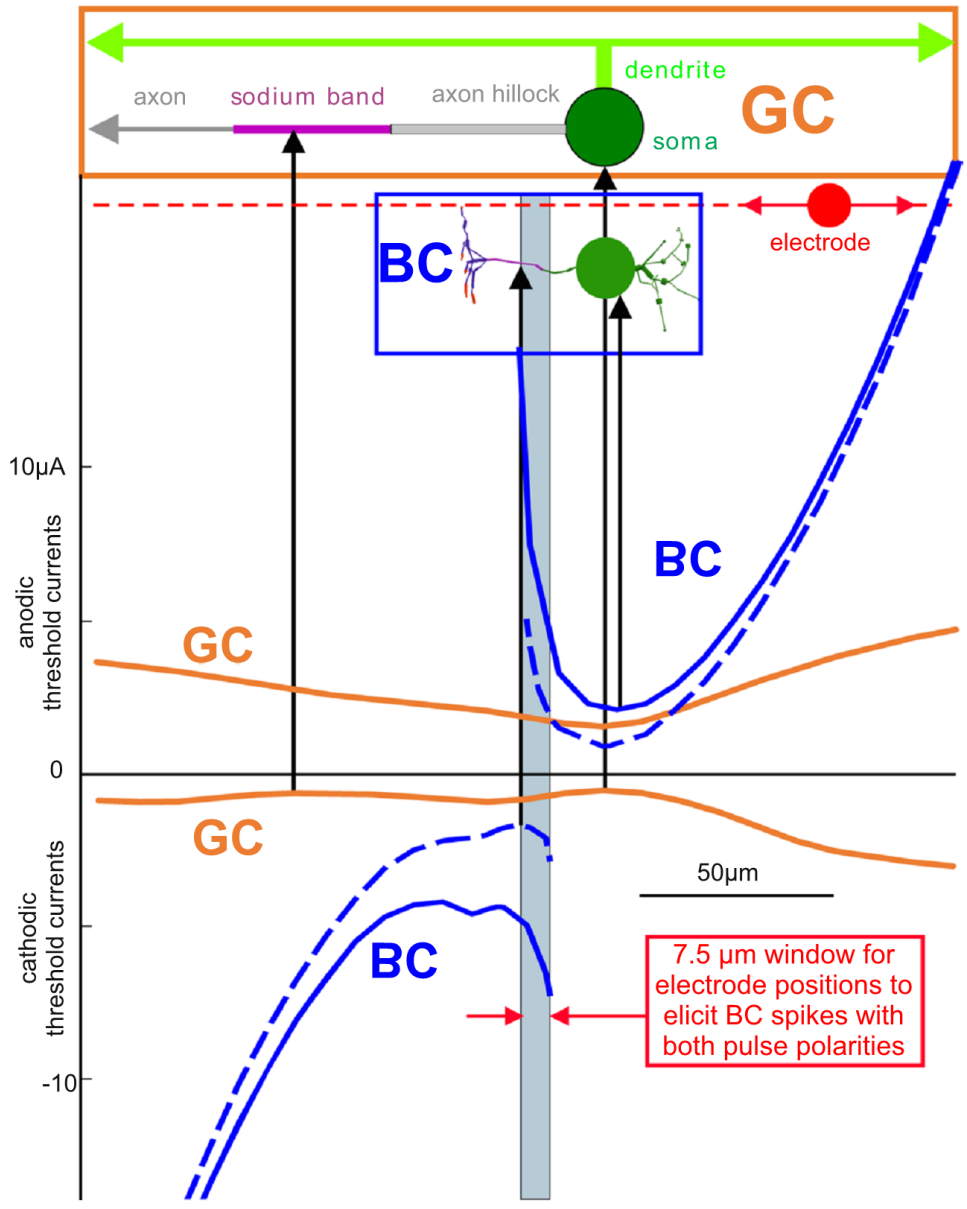

Figure 3.2: **Anodic and cathodic threshold currents to make spike for the bipolar and the ganglion cell when an extracellular stimulating electrode is located at the distance of 20 μm (solid lines) and 10 μm (dashed lines) from the axon.** For the GC both polarities will lead to spike generation at any electrode position, but spike is only generated in the BC with specific polarity in different positions. Only for a small area above the AIS of BC (highlighted with light blue rectangular) both polarities generate spike. Pulse duration is 10 ms.

Figure 3.3 a explaines the sensitivity of the PC for a similar situation of BC and GC in Fig 3.2. As the axon in the PC is myelinated and the sodium channels are located at the nodes of Ranvier, a zig-zag curve is seen for the cell in cathodic stimulation that is not seen in BC and GC. Also, since the dendrite compartments contain very small density of sodium channels in comparison to axon, electrode positions above the dendrite need higher thresholds than above the axon. A $-50\,\mu A$ pulse is just below the threshold for the electrode position marked with a red +. A bit larger pulse will make a spike at dendrite developing from the red line (Fig 3.3 b left upper case). Experimental studies also show a various spike initiation sites (Ranck, 1975; Gustafsson et al., 1976; Stuart and Sakmann, 1994; Nowak and Bullier, 1998).

From biophysical point of view, the main differences in the BC in comparison to GC and PC is that the sodium channels are only found within the sodium band. Thus, it is expected that the spike should always be generated from the sodium band in the BC, but the results of the BC in extracellular stimulation show another situation: When the stimulating electrode moves along the axon at the distance of 20 μm far from the neuron axis, only in a small region the spike is initially generated in the sodium band, Fig 3.4. For all other positions, strong transmembrane voltages in the terminals are the driving forces to generate the spike via intracellular (axonal) current flow. This is especially observable from the cathodic stimulation diagrams shown in Fig 3.4 right. As figure 3.4 shows, transmembrane voltage of the terminal has larger amplitude than the sodium band.

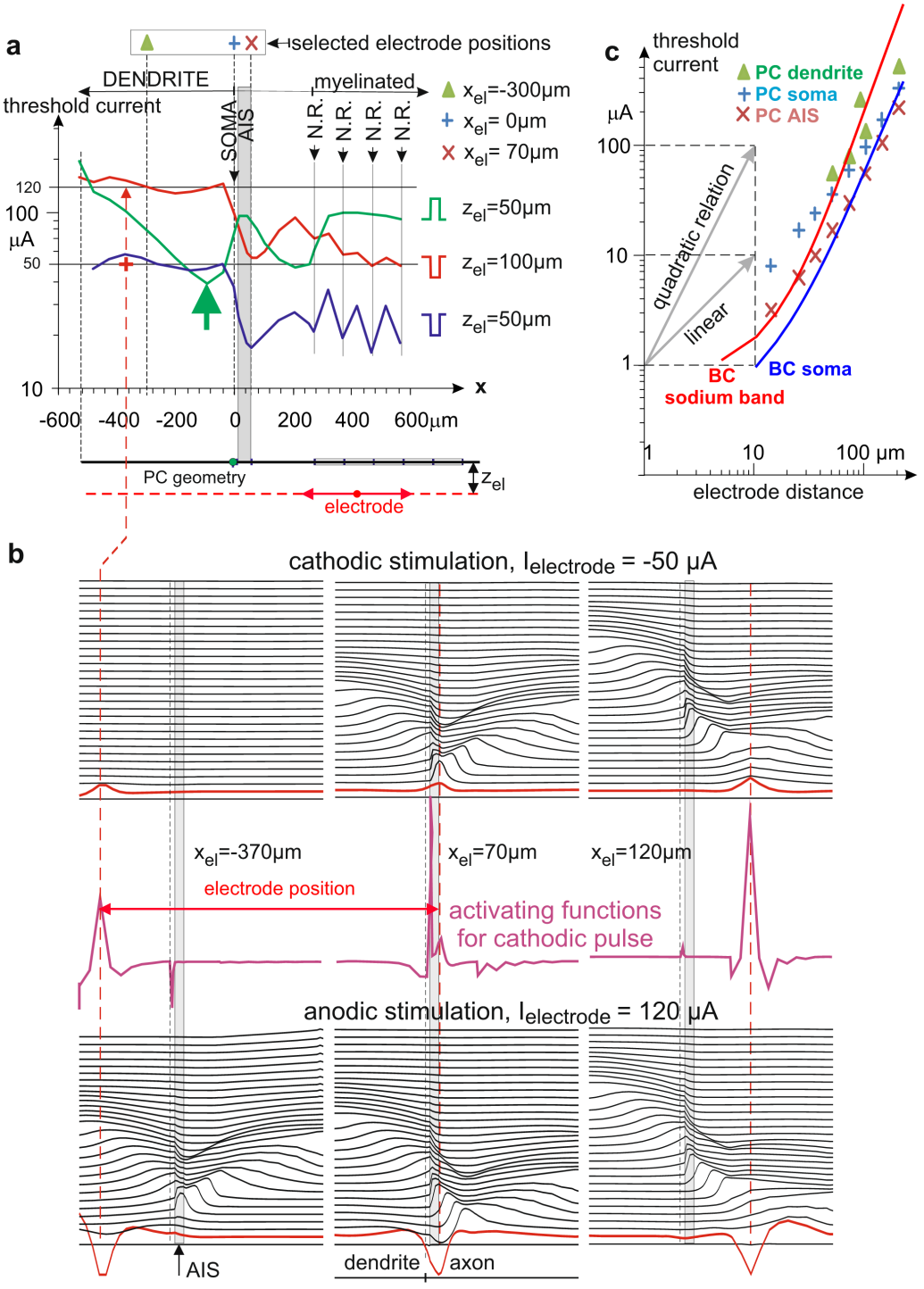

Figure 3.3: **Thresholds for the 1D pyramidal cell.** (a) Anodic and cathodic threshold currents for the PC when an electrode is moved parallel to the axon. (b) Transmembrane voltage changing over time along the cell (c) and radial current distance relationship for selected electrode positions. The lowest PC thresholds for cathodic pulses are taken place at the distal end of the sodium band (highlighted with gray area, AIS) and at the nodes of Ranvier (N.R.) in the myelinated axon. The anodic thresholds are dramatically bigger than for cathodic pulses (see green and blue lines in (a)). More explanations of AP generations are shown in (b) for -

both stimulus pulse polarities showing transmembrane voltage versus time along the cell. The shifted lines are for 100 μs intervals. Diagram c explains current distance relations for different electrode positions in extracellular stimulation of the PC (markers) and BC (solid lines). The depicted cases are for cathodic stimulation with exception of BC soma (blue line) that is, in agreement with Fig 3.2, only possible for anodic stimulation. The use of logarithmic scaling is because of change of current - distance relations from linear to quadratic. Pulse duration is 100 μs for PC and 10 ms for BC.

3.2 Discussion

A sodium spike in a spiking BC is generated via the following steps: (i) neurotransmitters released from PRs cause to open the ion channels of the dendrite, (ii) ion current flow into dendrite via T-type calcium channels make the cell slightly depolarized, (iii) after reaching the depolarization to the AIS, larger density of sodium channels in the sodium band generate a spike. The generated spike arrives to the terminals with an negligible delay (compare spikes of Figs. 3.1 and 3.4).

In the case of small synaptic input signals that is not enough to activate the sodium channels, the cell's response would only be graded potentials at the terminals. The amount of neurotransmitter released in such a 'subthreshold' stimulation is proportional to the dendritic membrane voltage (Euler et al., 2014; Singer and Diamond, 2006; Werginz and Rattay, 2016). Although T-type calcium channels in DB4 BC support the initiation of sodium spikes, generation of calcium spike via the channels is not possible because of their low density.

Generation of sodium spikes in the BC during extracellular stimulation depends on both polarity and position of the microelectrode. In some regions, the electrode should carry anodic pulses and on the other regions the electrode must be cathodic. Only for electrode positions within a small region, marked as direct excitation window in Fig 3.4, both polarities results in spike generation. This result seems to be important for subretinal implants in which position of electrodes close to a BC soma may be problematic.

One of the results observed both in experiments (Rattay and Wenger, 2010)

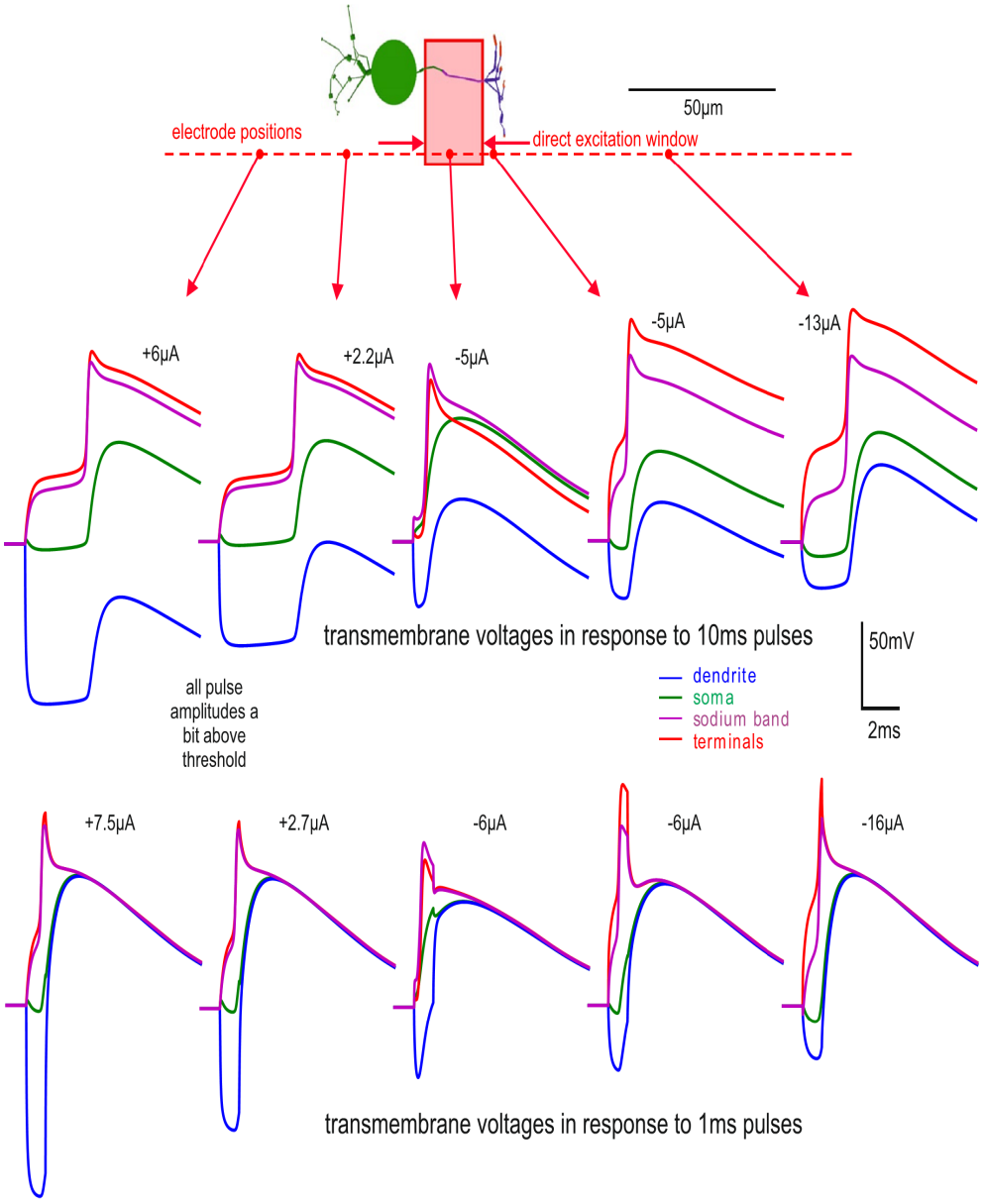

Figure 3.4: **Transmembrane voltages during anodic and cathodic extracellular stimulation.** Except for the case in which the electrode is above the sodium band, which was marked as red rectangle, spike is generated at the terminal in extracellular stimulations. In 4 out of the 5 shown cases, the terminal voltages are more depolarized than the sodium band both for 10 and 1 ms pulses. Electrode distance is 20 μA from the axon axis.

and computer simulations (Rattay, 1986; Rattay, 1990; Werginz, et al., 2014) is that anodal thresholds of neurites are about 4 times larger than the cathodal ones. This rule also holds roughly for GC as shown in Fig 3.2 and for the PC, Fig 3.3 a, but the BC again does not follow this rule as sodium spikes are not generated at all in anodal stimulation. The best electrode position for sodium spike generation is close to the sodium band in cathodic pulses.

Another result observed both in theory and experiment is that small axons are harder to stimulate than thicker ones (Blair and Erlanger, 1933). Thus, higher thresholds of the BC than the GC for cathodic stimulation (Fig 3.2) originate from the much smaller diameter of BC vs. GC (Table 2.1).

Chapter 4

Single-, two-, four-, and multi-compartmental model for DB4 Bipolar cell with cone-cylinder-cone soma

Three types of stimulation of BCs were investigated in this chapter; (i) simulation of intracellular stimulation of dendrites, which is taken at natural situations in which PRs put input at the dendrite of BCs; (ii) intracellular soma stimulation of BCs, the most common method used in experiments and (iii) stimulation of BCs by extracellular microelectrode, which is close to BC stimulation in retinal implants. The multi-compartment model explained at section 2.6 was used to prepare the results of this chapter.

4.1 Passive vs. active cell membrane

Only a small types of retinal BC are able to generate spikes, e.g. 2 in macaque (Puthussery et al., 2013) and 3 in mouse (Hellmer et al., 2016), and other types use graded potentials to communicate with other cells because of their passive cell membranes.

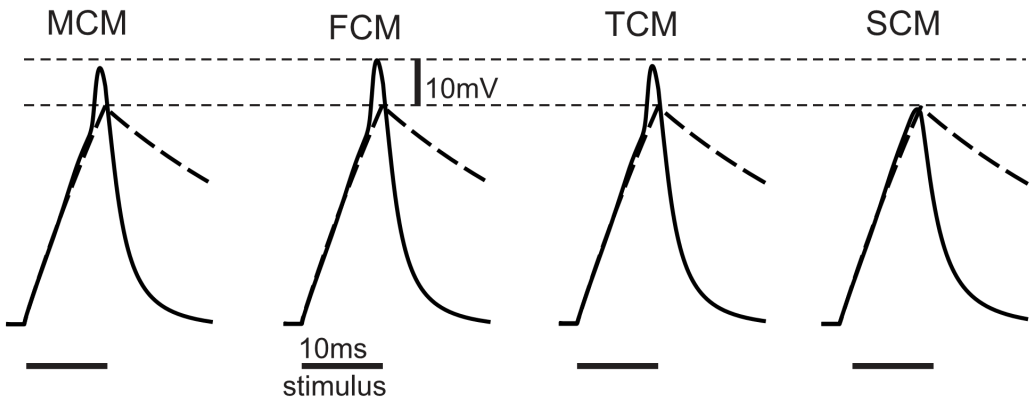

Figure 4.1: **Transmembrane voltage versus time for SCM, TCM, FCM, and MCM during soma stimulation.** A pulse with amplitude of 35 pA and duration of 10ms generate spikes in MCM, FCM and TCM, but not in SCM (solid lines). All models show almost the same behavior for passive membranes (dashed lines).

At first, to investigate the difference between passive and active membranes, a current pulse of 35 pA with a duration of 10 ms is injected to the soma in all of the SCM, TCM, FCM and MCM including both passive and active membranes, Fig 4.1. Figure 4.1 shows that when the position of sodium ion channels changes from the axon to the dendrite and soma region, in SCM, the spike is not generated. This is also true for TCM in which the sodium channels are shifted from the terminal to the soma compartment.

4.2 MCM vs. FCM and axon length impact on the transmembrane voltage

From geometrical point of view, the main feature varying among BCs is the axon length. Axon length of the largest BC is three times of the smallest. To investigate the impact of axon length on model behavior, we considered a new version of the FCM that the axon length is three times of the axon in FCM (the axon changes from 97.09 to 213.27 μm). Figure 4.2 shows the passive and active version of the new model as well as the original FCM and MCM when their dendrite is stimulated by intracellular pulse of 35 pA and duration of 10 ms.

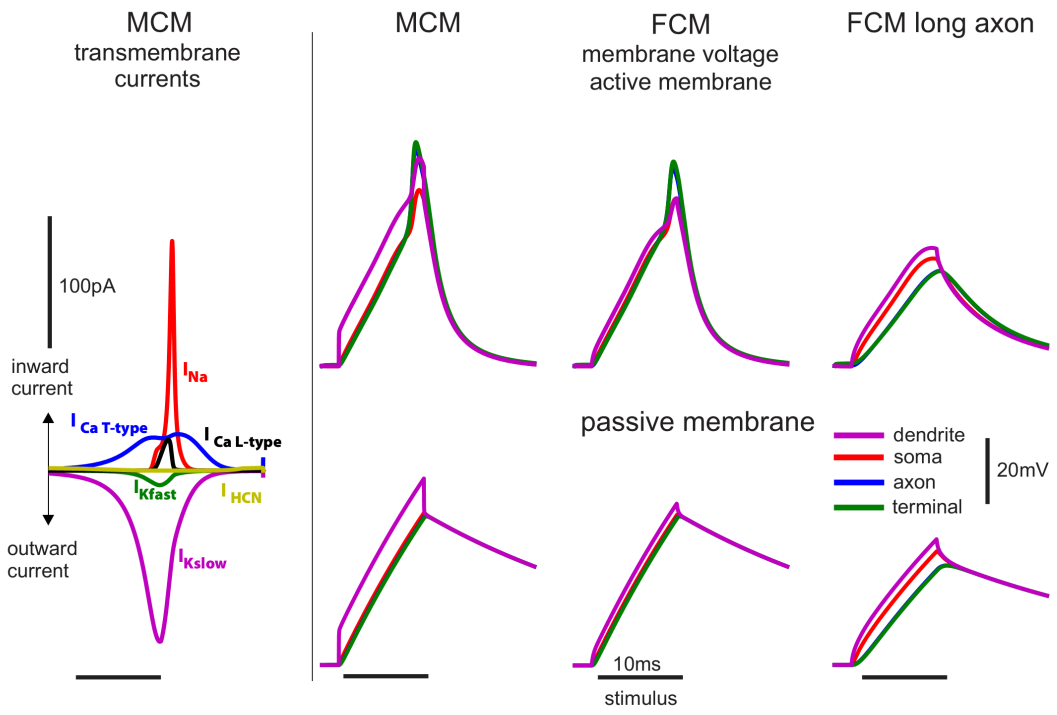

Figure 4.2: **Current and voltage membrane versus time in intracellular stimulation at dendrite.** Left) Currents of the active MCM. Both T-type calcium current and the slow potassium currents located in dendrite and soma are activated before the sodium current and obstruct each other's effect and so don't affect the timing of the sodium current in both FCM or MCM. Right) Transmembrane voltage versus time for a 35 pA pulse amplitude and 10 ms pulse duration. The weaker response in the long axon model is because of the bigger surface. The positions of the stimulating and recording electrodes in the MCM are depicted in Fig 2.9.

There are several differences in the membrane voltages between these three models. The main difference between the FCM and MCM is the higher transmembrane voltage of dendrite in MCM both in active and passive membranes originating from size of the dendrite. Since the dendrite tips in the MCM are so thin, in comparison to FCM, it highly increases the resistance between adjacent dendritic compartments. Thus, the injected current encounters to a big axial resistance and can not pass through it resulting in a higher local transmembrane voltage than the FCM. There is small difference between the transmembrane voltages of soma, axon and terminal in FCM and MCM, but the long axon FCM shows a smaller depolarization due to small transmembrane currents in the pas-

sive part of the axon.

In the active case, the MCM and the original FCM do not show similar spikes. Higher dendritic voltage in the MCM is seen. As in 3 mentioned, the spike is generated in the axon due to higher sodium channel density and backpropagates to the soma and dendrites. Thus, higher dendritic voltage in the MCM originates from large axial resistance of the dendrite in comparison to FCM. The long axon FCM shows a lower membrane voltage in all compartments both in active and passive cases and no spikelet.

The voltages of the MCM and FCM except for dendrite also matches well in passive membrane. The longer axon leads to increment of axonal resistance and loss of signal. To elicit the same response as in the FCM or MCM, a higher stimulation pulse amplitude is needed in the larger FCM. Thus, a FCM developed for one kind of BC may not work for a different type without adaptations.

4.3 Maximum of membrane voltage for long pulses

To investigate behavior of both FCM and MCM in both active and passive membranes, a 100 ms pulse with different intensities is injected to dendrite and soma of both models and the maximum membrane voltages are recorded in dendrite, soma, axon and terminal, Fig 4.3.

For both cases of somatic and dendritic stimulations in the active membrane, the maximum voltages recorded from different sites are dramatically the same in MCM and FCM, with a maximum difference of less than 3%, except for dendrite voltage in dendritic stimulation. This result also was shown in Fig 4.2.

Also, it was already shown that all four models show similar transmembrane voltages when the soma is stimulated in passive membrane, Fig 4.1. As the passive membrane behaves like a linear system, the maximum magnitude of transmembrane voltages is proportional to the pulse amplitude injected to the cell. This behavior is independent from model type or the stimulation site.

The maximum voltage in the active cases is smaller than the passive cases due

to repolarizing transmembrane currents originating from two types of potassium channels. The sharp increase in maximum voltage of active case that occurs after threshold current 32 pA shows activation of the sodium channels.

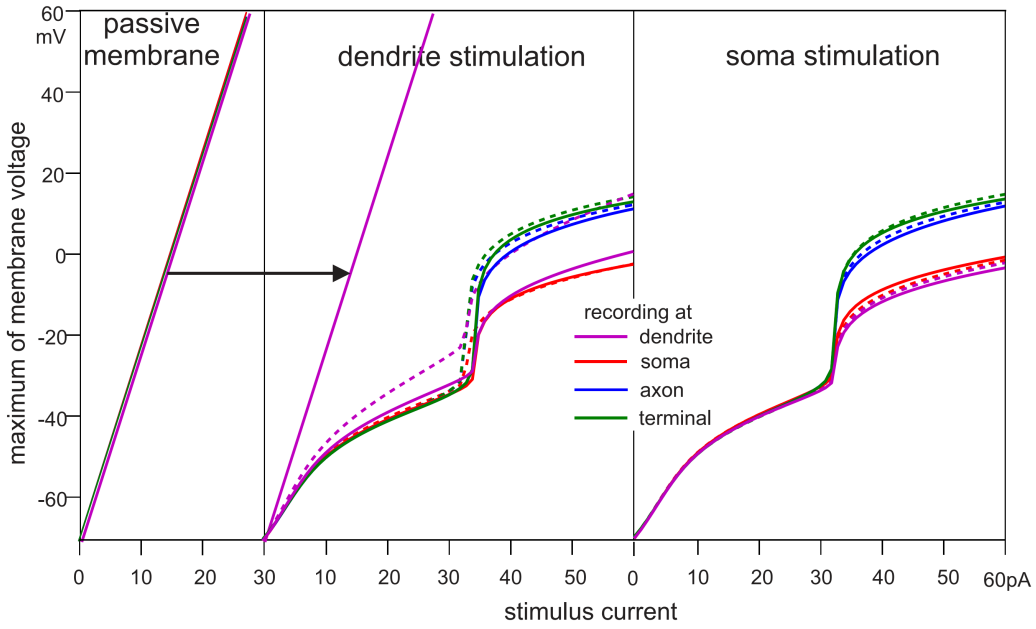

Figure 4.3: **Maximum transmembrane voltage versus pulse amplitude for 100 ms pulse duration.** Left) The dendritic stimulation of MCM in passive membrane. Hardly recognizable recordings in soma, axon, and terminal compartments represents the same linear behavior. middle) FCM versus MCM under dendritic stimulation. right) FCM versus MCM under somatic stimulation. Solid lines are FCM and dashed lines are the MCM.

4.4 Sinusoidal stimulation

Experiments on DB4 BC with 5 Hz sinusoidal current injection to the soma with pulse amplitude of 10 pA (Fig 9c in Puthussery et al., 2013) shows one spike per peak with a delay of $2.9 \pm 1.0\, ms$. A similar behavior with small longer delay is seen in the MCM as well (Fig 4.4).

Figure 4.4 shows several results as following, (i) terminal membrane voltage increases relative to the soma voltage, (ii) peak of the L-type calcium current

appears about 0.5 ms after the sodium current peak presenting fast synaptic activation, (iii) I_{HCN}, which is activated during the hyperpolarization phase of the sinus current, supports spiking by making the cell depolarized (highlighted by arrow in Fig 4.4, middle trace).

The last MCM computer simulation of Fig 4.4 was also done for FCM, TCM and SCM to clarify the differences, Fig 4.5. Decrement in the number of compartments results in decrease of spike amplitude. This phenomena can be explained by the axial (intracellular) resistance between compartments, although it has no representation in the SCM. As the axial (intracellular) resistance increases, the sodium spike hardly pass through the axonal membrane that results in increasing the membrane voltage. Perhaps, this is the reason why sodium channels themselves are located in axon or near thin segments in most of the neuron types. This effect cannot be explained by the TCM and SCM representing another reason why these models should not be used in active membrane.

4.5 Extracellular stimulation

Extracellular stimulation refers to current injection to an electrode (a point source in this case). The current affects extracellular medium by making an external potential, see Eq. 2.8. Since the resistivity of the extracellular medium is considered to be constant, this results in a spherically symmetric potential gradient around the electrode. Thus, different parts of the cell senses different extracellular potentials that depends on their distance to the electrode.

As soon as the pulse is injected to the electrode, the external made electric field causes capacitive currents through the cell membrane that means a potential difference between interior and exterior side of the cell is made. If the stimulation continues with constant intensity, intracellular currents flow until all internal points sense almost the same potentials again. In anodic stimulation (positive current injection), the external spherical potential surfaces close to the electrode is higher than the surfaces close to the cell compared to the intracellular potential. Thus, cell regions closer to the electrode hyperpolarizes and the more far region

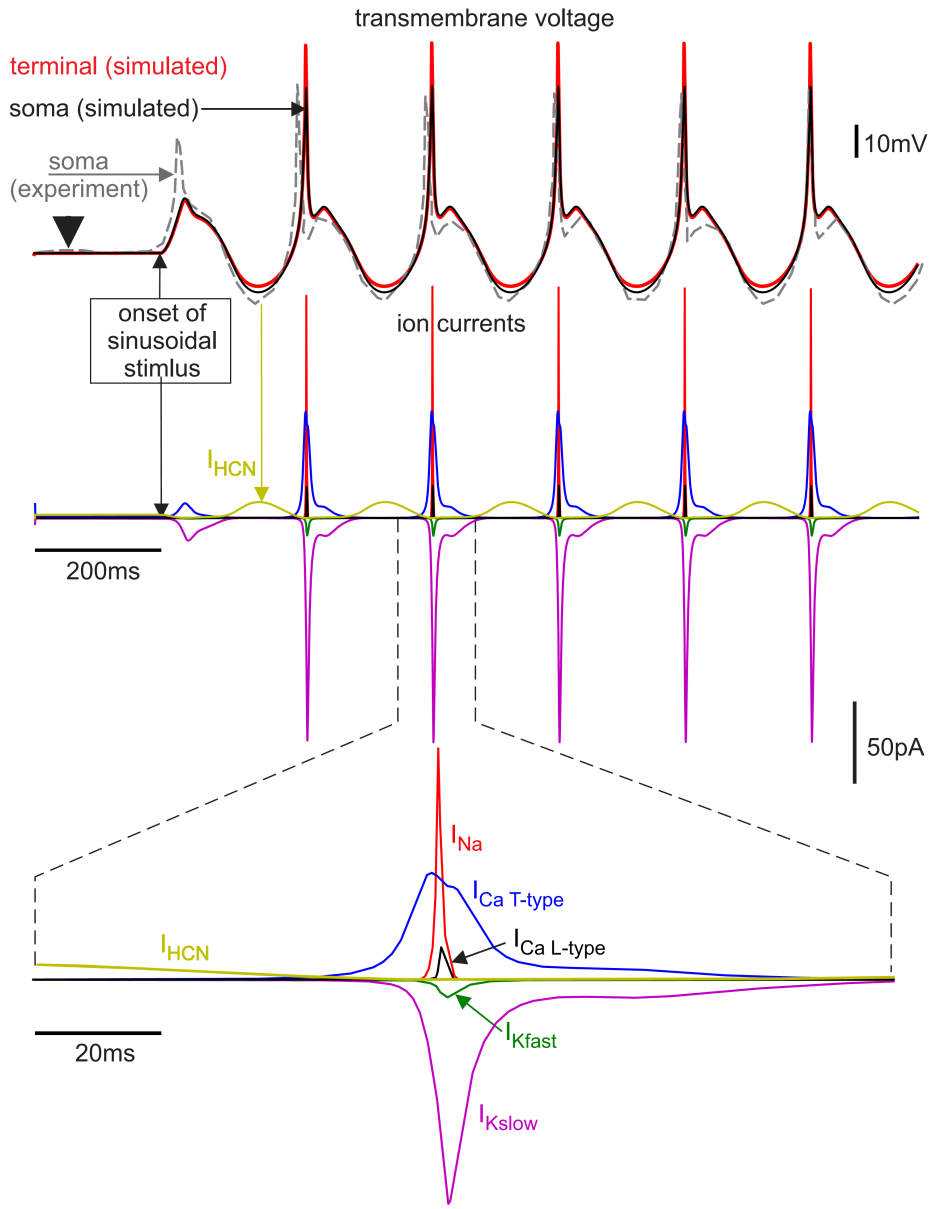

Figure 4.4: **Transmembrane voltage and currents during 5 Hz sinusoidal current injection at the soma.** top) Simulated and experimental spikes. middle) Related ion currents. bottom) Ion currents for a small window. Membrane voltage recorded at the soma is redrawn from Fig 9c of (Puthussery et al., 2013). The pulse amplitude is 10 pA.

points depolarize, Fig 4.6. This is vice versa for cathodic stimulation (negative current injection); for details see (Rattay et al., 2017).

This results is seen in the transmembrane voltages versus time in Fig 4.6. The dendrite transmembrane voltage changes faster in the MCM than in the FCM, because the dendrites in MCM have more total resistance than in the FCM, see 4.1. Thus, the membrane voltage of different parts of the cell located at the vicinity of an electrode depends on the cell geometry, which explains resistance of each compartment, and the orientation relative to the electrode, which defines either a compartment hyperpolarizes or depolarizes.

For each compartment, the external voltage V_e is calculated by the distance of the compartment center from the electrode, Eq. 2.8. This means that two edges of a single compartment with a large length sense different extracellular voltages, but the model only considers one value per compartment. Therefore, a model containing more compartments simulates more faithfully the effects of extracellular stimulation, MCM used here is in a good condition.

In figure 4.6, the simulation were done with TCM, FCM and MCM, all of them contains a passive membrane. The electrode was located at $30\,\mu m$ above the soma center and the pulse amplitude and duration were $1\ \mu A$ and $1\ ms$, respectively. The membrane voltages were again recorded from dendrite, soma, axon, and terminal if exist. Since the SCM cannot explain extracellular stimulation at all, it is not included in Fig 4.6. All cells show the predicted polarization. The soma in the TCM polarizes because the TCM does not have dendrite and the soma is the closet compartment to the electrode. This is vice versa in the FCM and MCM. The voltage traces of the FCM are roughly comparable to those of the MCM.

In Fig 4.6, the electrode distance to the BC is the same as in the subretinal implant for the blind. As several retinal BCs are able to generate spikes, it is of interest whether spikes can be generated both for this distance or more remote positions that are typical for epiretinal implant types. Figure 4.7 shows the membrane voltages of dendrite, soma, axon and terminal versus time for stimulus intensities just above threshold for the BC with active membrane. The cell is at

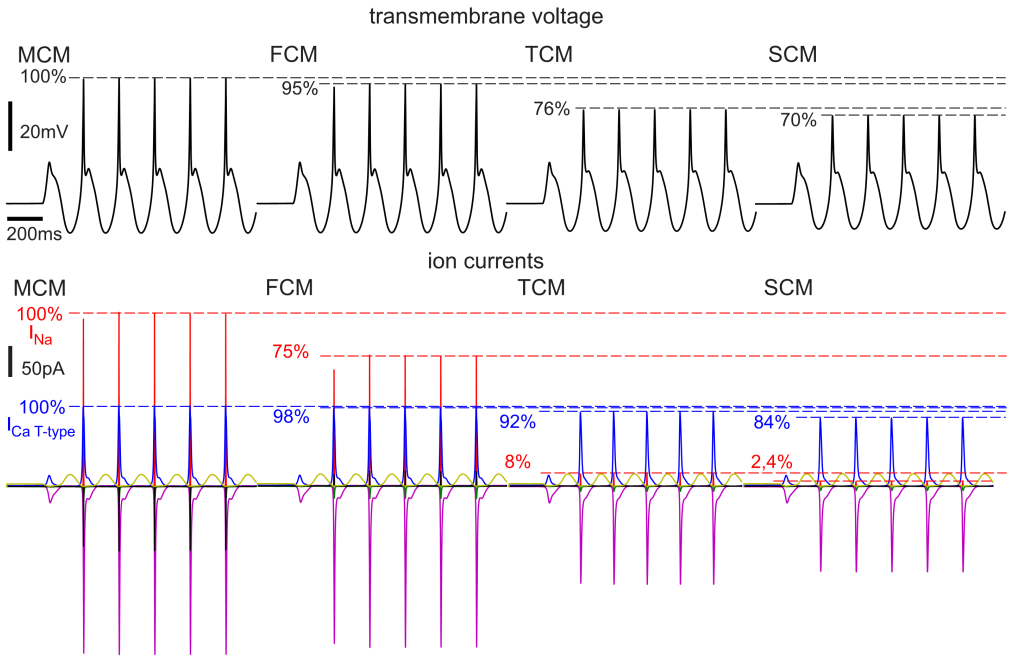

Figure 4.5: **Spikes and ionic currents for the sinusoidal current injection at the soma as in Fig 4.4 for different models.** T-type calcium currents are not so sensitive to model with maximum decrease of 16% of amplitude (MCM vs. SCM). However, the sodium current is highly sensitive to model.

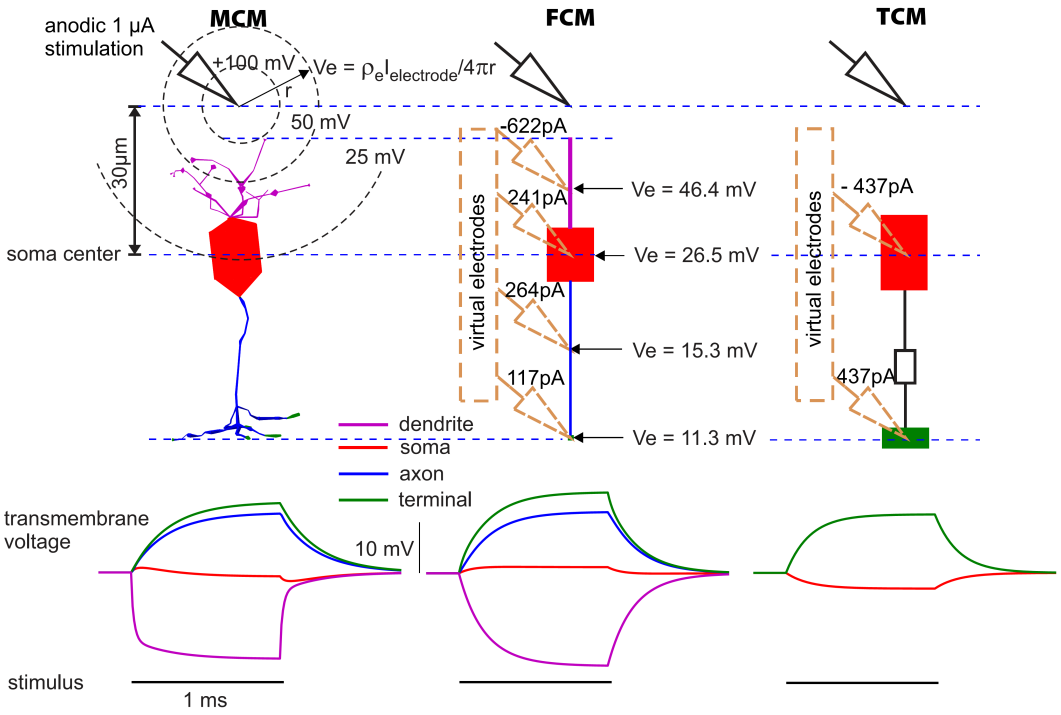

Figure 4.6: **Morphology (top) and transmembrane voltage versus time in passive membrane (bottom) of MCM, FCM, and TCM when the models are stimulated with anodic pulse extracellularly.** The pulse amplitude is $1 \mu A$ pulse applied at the electrode located $30\,\mu m$ above the soma center. The electrode generates spherical equipotential surfaces, shown as dashed circles in 2-D.

rest initially. The first parts of the cell behavior is approximately the same as the passive model because all ion channel are closed during the subthreshold phase (compare Fig 4.6 and both graphs at the top of Fig 4.7 during 1 ms of pulse application). Considering the whole excitation process, as the membrane voltage of the terminal is higher than any other part of the cell in all cases, it means that spikes are generated in the terminal. This is also true when the electrode is located below the cell, where cathodic pulse is needed to generate spike (Fig 4.7 bottom).

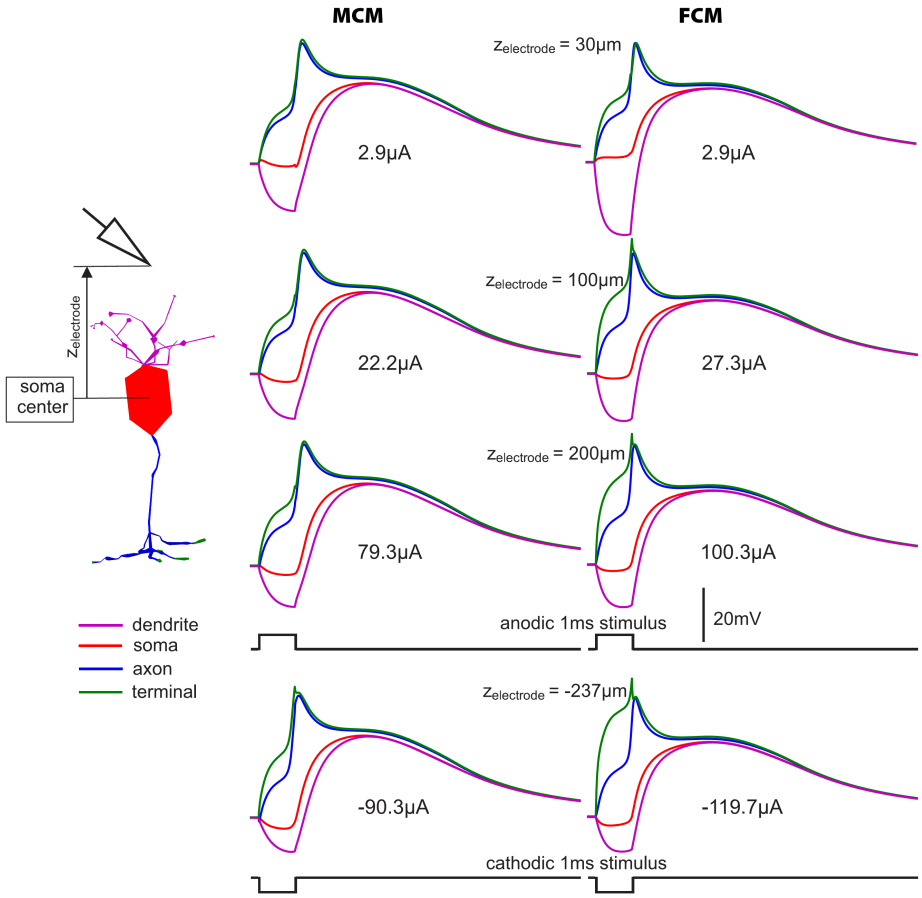

Figure 4.7: **Transmembrane voltage versus time as well as the needed threshold currents of MCM and FCM to generate a spike for four electrode positions along the cell axis.** Thresholds (2.9 μA, 22.2 μA, etc.) increases in a non-linear way with $z_{electrode}$, the electrode distance from soma center, as excepted (see, 2.8). $z_{electrode}$ equal to 30 μm simulates the position used in subretinal implants, 100 and 200 μm are the positions close to epiretinal implants, and the -237 μm case (here the electrode is actually 200 μm far from the closest terminal ending) represents suprachoroidal electrode position (Shepherd et al., 2013; Werginz and Rattay, 2015).

4.6 Discussion

The presented FCM can reproduce many of the results calculated by the MCM, which uses real morphology of the BC, in a shorter time, while TCM and SCM

are not able to do this.

According to the natural signal transfer through the DB4 BC starting at a dendritic synapse, which the dendrite is stimulated via PRs, and ending at one of five axon terminals, the total axial resistance is given by $R_{Dendrite} + R_{Soma} + R_{Axon} + R_{Terminal}$ in the FCM, see Fig 2.9.

The main physiologic parameters of rat rod BCs containing a passive membrane are: specific membrane capacitance = $1.1\,\mu F/cm^2$, axial specific resistivity = $130\,\Omega.cm$ and specific membrane conductance = $0.042\,mS/cm^2$ (Oltedal et al., 2009). These values are close to DB4 BC used in this paper, $1.0\mu F/cm^2$, $100\Omega.cm$, $0.033mS/cm^2$, taken from ref (Puthussery et al., 2013). As retinal BCs are among the smallest interneurons of the nervous system, there is almost no delay in signal transmission in these cells. Additionally, small specific membrane conductance causes almost no attenuation in the signal transmission (Oltedal et al., 2009). Both of these features enable the cells to transmit single photon signals without inquiry of active membrane (Field and Rieke F, 2002).

In experiments, stimulation and recording can only be done by using soma due to its relatively large diameter. According to Fig 4.1, the SCM and TCM reproduce almost the same results as the MCM while the cell has a passive membrane. SCM and TCM were already used successfully for BCs, for SCM see (Guo et al., 2014; Ishihara et al., 1998; Ishihara et al., 2003; Publio et al., 2009; Usui et al., 1996) and for TCM see (Freeman et al., 2011; Mennerick et al., 1997; Oltedal et al., 2007; Werginz and Rattay, 2015). In addition to SCM and TCM, MCM using both 2D and 3D approaches has been used for BCs with passive (Oltedal et al., 2009; Resatz and Rattay, 2003; Rattay et al., 2003; Werginz and Rattay, 2016; Werginz et al., 2015) and active membranes (Benav, 2012; Rattay et al., 2017).

The main limitation of SCM is not to be able to be used in extracellular stimulation since both of the terms in Eq. 2.7 are eliminated ; see also (Rattay, 1999). Although this limitation is resolved in TCM, TCM itself has a very low accuracy due to neglect of intracellular resistances 4.6. FCM is also not trustable in extracellular stimulation 4.6. Thus, to model extracellular stimulation accurately,

MCMs are vital.

The data in this chapter suggests some heuristics points for accuracy tests in future research. Any of SCMs, TCM or FCM are adequate for simulation of a BC with passive membrane during intracellular stimulation. In active membranes, approximately all results were qualitatively correct for FCMs exepct for dendrite recording during dendritic stimulation, but the accuracy depends on the individual task (Figs 4.2, 4.3, 4.5, 4.7).

Chapter 5

Vesicle release from a ribbon synapse of a bipolar cell

Because the expression of sodium channels on the membrane of amacrine and GCs had been detected, these two types of neurons were for many years the only candidates to generate spikes in the retina; all BCs were considered to have passive membranes (no sodium channel on the membrane). Thus, the synaptic ribbon was assumed to be responsible for both transient and sustained responses in BCs (Matthews and Fuchs, 2010). However, the detection of sodium spikes in BCs (Cui and Pan, 2008; Puthussery et al., 2013) containing ribbons as well as recent progress in retinal implants has led to questions such as 'what is the role of the spike on vesicle release in a BC-containing ribbon?', 'how do spiking and non-spiking BCs behave in an external electric field?', and 'why does contrast detection gradually decrease in patients using retinal implants?'. This chapter aims to response to these questions. The multi-compartment model and synapse models explained in section 2.7 were used to calculate the results of this chapter.

5.1 Differences between modelV and modelCa

One of the differences between modelCa, Eq. 2.95, and modelV, Eq. 2.87, is the signal delay, i.e., the time interval between stimulation of the BC and the release of the first vesicle. The modelV has no signal delay, while the modelCa has a

maximum signal delay of $0.43ms$, similar to experimental data (Baden et al., 2011, Singer and Diamond, 2003; see discussion), Fig 5.1. Figure 5.1 shows the first transiently released vesicles versus time when the terminal membrane changes from -70 to other potentials with a step voltage of $5\,mV$ in a voltage clamped experiment. Transiently released vesicles have a time delay of 0.27, 0.34, 0.40, 0.43, and $0.43\,ms$ when the transmembrane voltage changes from $-70\,mV$ to -45, -40, -35, -30, and $-25\,mV$, respectively.

5.2 Vesicle release from spiking and non-spiking bipolar cells in intracellular stimulation

To investigate vesicle release in spiking and non-spiking BCs, two cells with the same geometry should be considered in extracellular stimulation because the geometry of the cells defines the shape and amplitude of the potential exerted to the compartments (Rattay et al., 2018). Thus, an imaginary spiking BC with the same shape was made by adding sodium and potassium channels to the axon. When the two spiking and non-spiking BCs are stimulated intracellularly with a $100\,ms$ rectangular pulse of $500\,pA$, the terminal transmembrane voltage of the non-spiking BCs reaches $-48mV$, leading to no transient vesicle release; however, the voltage membrane of the terminal in spiking BCs passes through $-10\,mV$, which means that the terminal depolarizes for $50\,mV$, leading to the release of all 10 vesicles existing in the pool (Fig 5.2). Both models in Eq. 2.87 and 2.95 produced the same results. Thus, spikes make the RRP empty. Here, sustained release is not of interest because the pulse duration is not long. An average of the three sustained vesicle is released among a 100-ms pulse stimulation in spiking BCs, while this number is less than one in the cell with a passive membrane.

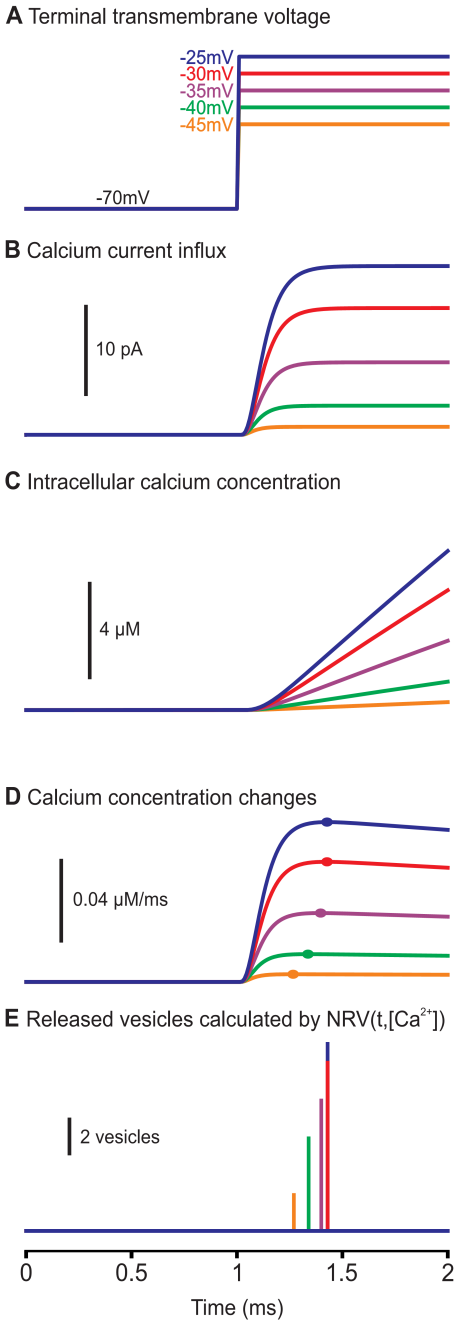

Figure 5.1: **ModelCa based on the intracellular calcium concentration has a maximal time delay of 0.43 ms.** A) Voltage of the terminal membrane is clamped at $-70\,mV$ and then changed to other voltages with a voltage step of $5\,mV$. B) Calcium current coming to the terminal with a positive sign and C) intracellular calcium concentration for the same protocol as A. D) Calcium concentration changes versus time (solid lines) as well as local maximum points (circles). E) Released vesicles versus time calculated by 2.95. Transiently released vesicles have a time delay of 0.27, 0.34, 0.40, 0.43, and 0.43 ms when the transmembrane voltage changes from $-70\,mV$ to -45, -40, -35, -30, and $-25\,mV$, respectively.

5.3 Vesicle release from spiking and non-spiking bipolar cells in extracellular stimulation

When both spiking and non-spiking BCs are stimulated extracellularly with small pulse amplitudes, between $0.9 - 3\,\mu A$ and a long pulse duration of $10\,ms$ (Fig 5.3), the number of transiently released vesicles increases linearly versus the pulse amplitude for the non-spiking cell while it increases exponentially in the spiking cell because the spike has sufficient time to reach to the terminal and make the terminal more depolarized. Both cells with active and passive membranes have the same behavior in small pulse durations, such as $3\,ms$, since the terminal in both of the cells senses the same voltage originating from the microelectrode and the spike does not have sufficient time to reach to the terminal (data not shown). The major difference between the two models appears when the pulse amplitudes pass through $4\,\mu A$; the number of transiently released vesicles starts decreasing in modelCa but remains constant in modelV (Fig 5.3). The reduction in the number of transiently released vesicles for large pulse amplitudes is because of the outward calcium currents that take place when the terminal transmembrane voltage depolarizes more than $E_{ca} = -20\,mV$.

5.4 Vesicle release from spiking and non-spiking bipolar cells during pulse trains stimulation

Figure 5.4 shows the responses of spiking BC among pulse trains. To do this, the spiking BC is stimulated with a pulse amplitude of $1500\,pA$ and $3\,\mu A$ in intra- and extracellular stimulations, respectively, with a pulse duration of $1\,ms$ followed by a 200-ms zero amplitude pulse (5 Hz pulse). Spike amplitudes are 52, $45\,mV$ in intra and extracellular stimulations, respectively. In both the intra- and extracellular stimulations, the number of transiently released vesicles reaches a constant value, 3 vesicles, because all of the 10 vesicles existing in the pool are released after being exerted by the first pulse but the pool receives 3 vesicles from the ribbon in the recovery time of $200\,ms$ (Fig 5.4).

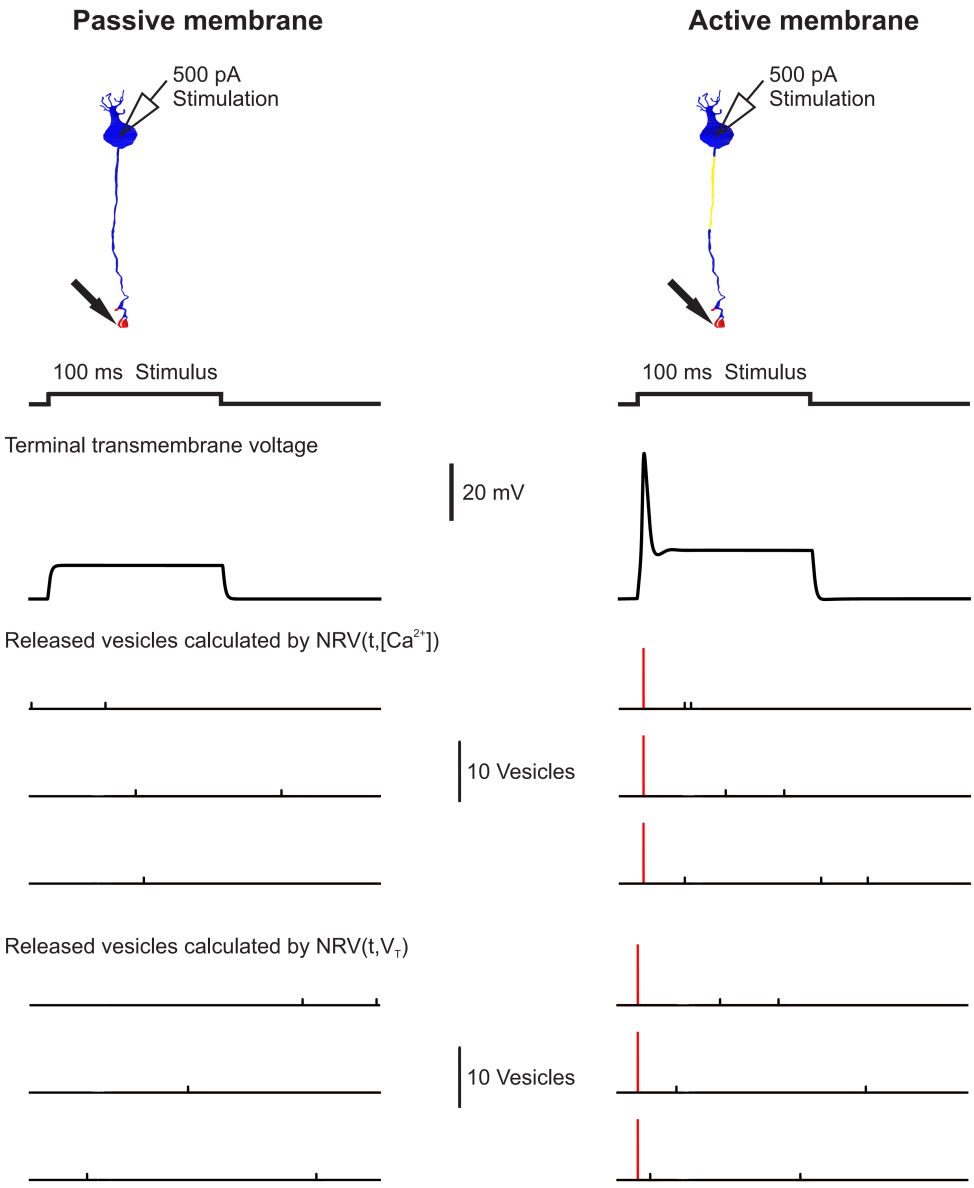

Figure 5.2: **Vesicles released in a passive vs. active membrane in intracellular stimulation.** Passive compartments are highlighted in blue, and compartments containing L-type calcium channels are highlighted in red. The yellow part represents sodium and potassium channels that amplify the stimulus (top). The released vesicles from the terminal for three trials are both calculated by 2.95 and 2.87. For the passive membrane, the terminal transmembrane voltage does not reach $-45\,mV$ and therefore no transient release occurs. This is in contrast to the active case in which the spike causes a transient release of all 10 vesicles calculated by both models of 2.95 and 2.87.

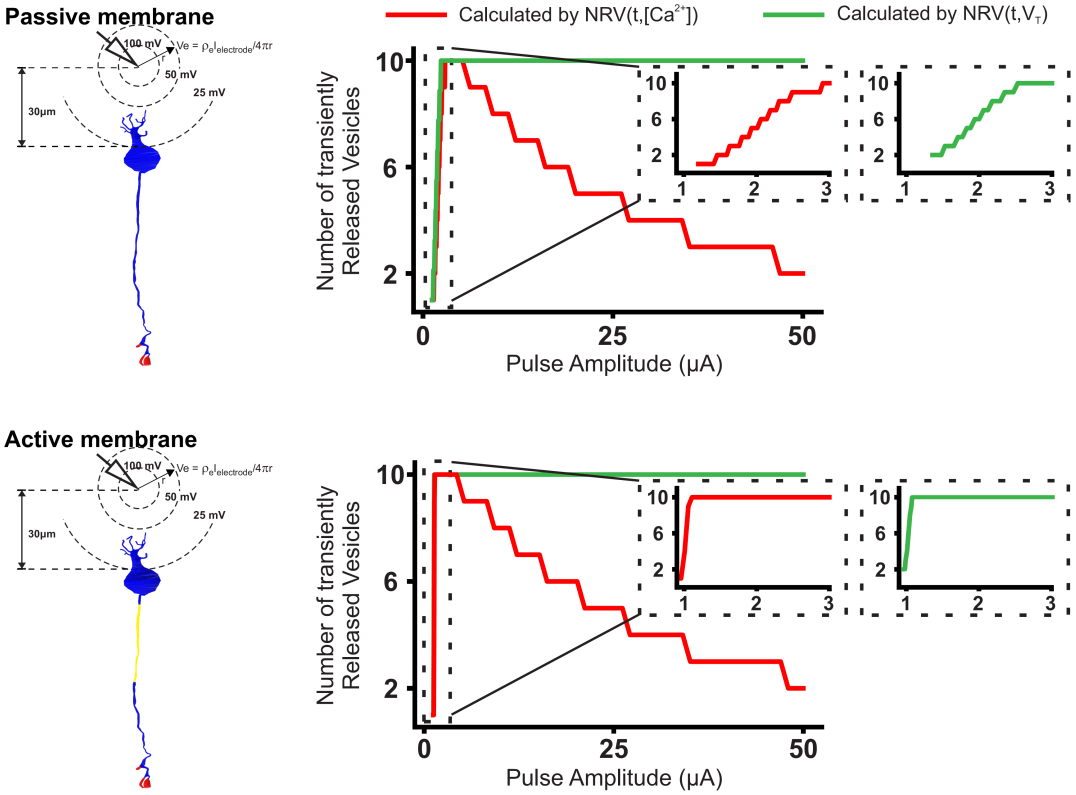

Figure 5.3: **Extracellular stimulation makes the RRP empty for small pulse amplitudes.** A microelectrode located 30 μm above the soma generates isopotential surfaces that scale inversely with distance r from the tip of the microelectrode, and the potentials are for anodic 1 μA pulse (left). The number of transiently released vesicles versus the pulse amplitude for the pulse duration of 10 ms (right). Bottom: the active cell membrane has a smaller stimulation window for the graded vesicle releases. The red (green) lines show the number of transiently released vesicles calculated by 2.95 (2.87).

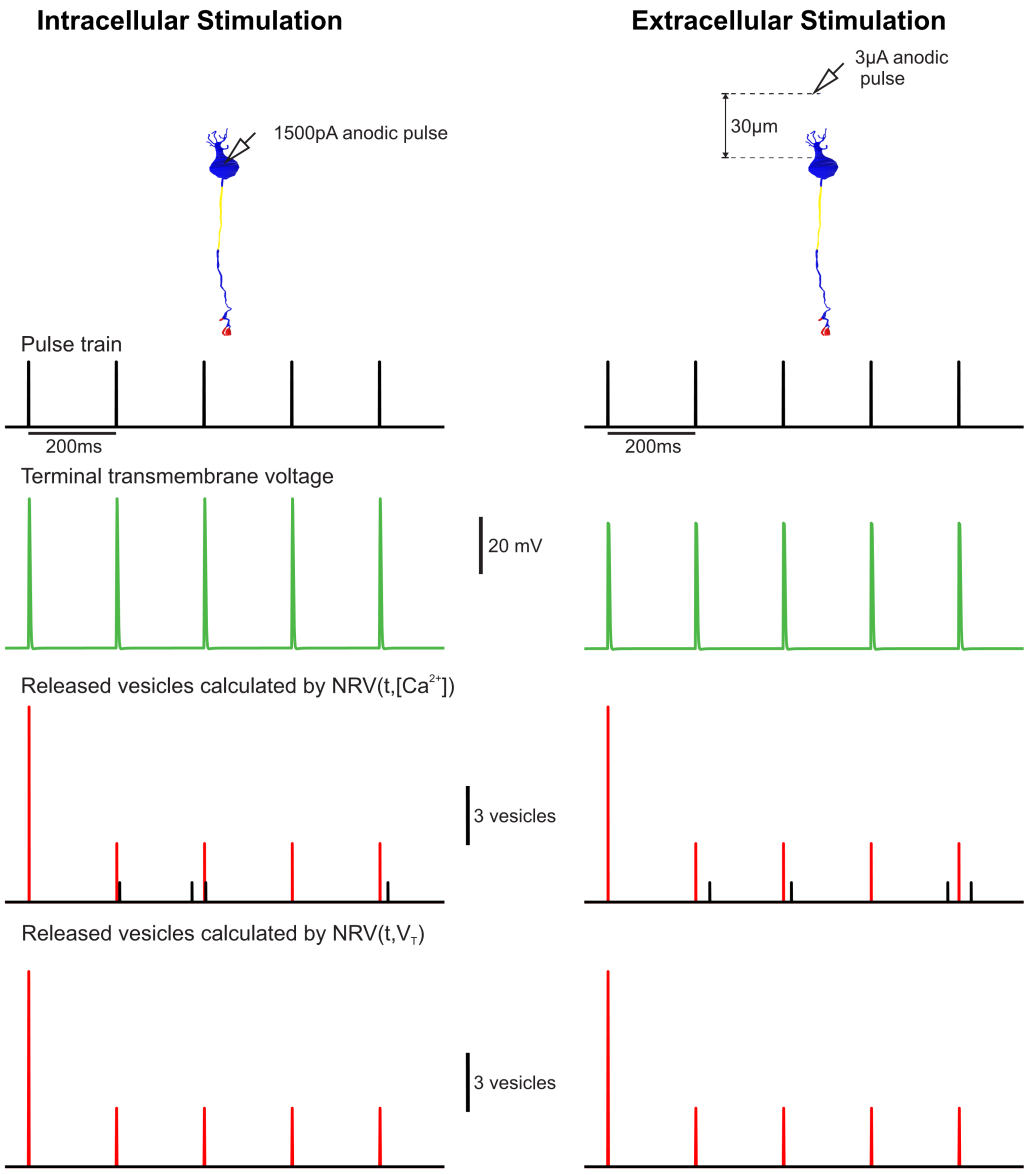

Figure 5.4: **The number of transiently released vesicles reaches a constant value in spiking BCs both for intra- (left) and extracellular stimulation (right) while using a periodic pulse with pulse amplitudes of 1500 and 3 μA, respectively.** The terminal transmembrane voltage reaches $-8\,mV$ for intracellular stimulation, while in extracellular stimulation, the terminal depolarizes up to $-15\,mV$, as shown in the green diagrams. The simulation of vesicle release both by 2.95 and 2.87 suggests that spike generation makes the RRP empty in both the intracellular and extracellular stimulations after the first pulse. When the RRP becomes empty, transient releases are also observed in the next stimulations because of recovery. The red lines represent transient releases and black lines show sustained releases.

5.5 Discussion

The available BC experimental data show that the largest variations are seen between fish and mammalians. In goldfish, the MB1 BC contains 50 synaptic ribbons (von Gersdorff and Matthews 1996; Neves and Lagnado 1999) in which around 110 vesicles are connected to each ribbon (Lagnado et al., 1996; von Gersdorff and Matthews 1996) and 22 of the 110 vesicles are readily releasable (von Gersdorff and Matthews 1996; Neves and Lagnado 1999). The average diameter of the vesicles in Mb1 is $36nm$ (Lagnado et al., 1996). Different recovery time constants have been reported for these cells ranging from $4\,s$ (Mennerick and Matthews 1996) to 11.8 s (Palmer et al., 2003). Rat RBC, which was the main object of this study, contains 36 synaptic ribbons (Singer et al., 2004), while each ribbon contains 22-48 vesicles according to a recent experiment (Graydon et al., 2014), which is in correspondence to the previous experiment showing 35 vesicles per ribbon (Singer and Diamond 2006). The vesicle diameter in the rat RBC is $38\,nm$ (Graydon et al., 2014) and is close to the vesicle diameter in Mb1. The size of the RRP in rat RBC has been reported as 7 (vesicles) using computational methods (Singer and Diamond 2006) and from 5.7 to 11.9 in experiments (Graydon et al., 2014). The reported recovery time constant in the rat RBC is $3.9\,s$ (Singer and Diamond 2006). Different numbers have been reported for the number of ribbons in the mouse RBC; the minimum number shows 23 ribbons (LoGiudice et al., 2008), while the maximum is 46 (Tsukamoto et al. 2001). Another reported value, 34, can be considered as an average (Wan et al., 2008). The average vesicle diameter in mouse RBC is $33\,nm$ (LoGiudice et al., 2009), although other numbers have been reported, such as 29 to $35\,nm$ (Spiwoks-Becker et al., 2001). The number of vesicles tethered to each ribbon in mouse RBC is 12-35 (Wan et al. 2008), while 8 (Wan et al., 2008) or 10 (Wan et al., 2010) vesicles make the RRP. The recovery time constant in mouse RBC is $417\,ms$ (Wan et al., 2008). Cb2 BC in ground squirrels has a time constant of $70-140\,ms$ (Light and DeVries 2007; Grabner et al., 2016), while this number for the Cb3 BC is $524-888\,ms$ (Light and DeVries 2007; Grabner et al., 2016) and

for the Cb1 is $482-734ms$ (Grabner et al., 2016). To our knowledge, the recovery time constant of BCs in rabbit and monkey have not yet been investigated.

The key data of the presented two models are based on experiments by Diamond and coworkers who estimated the transient and sustained release from the postsynaptic currents of rat RBC (Oesch and Diamond 2011, Singer and Diamond 2003). In modelV, the release and refill processes are directly related with the transmembrane voltage of the terminal, while in modelCa the intracellular calcium concentration of the terminal is the key variable. Furthermore, both models were combined with a multi-compartment model to demonstrate characteristic differences in vesicle release when spikes or graded potentials are the driving forces. Each model is made of four terms explaining the refill, recovery, transient release, and sustained release. The calcium ion channel gating in the presynaptic membrane causes ModelCa to respond with a time delay of $0.43\,ms$ for the transient release when the largest voltage steps are applied (Fig 5.1), while in modelV, this signal delay is missed. According to experiments by Singer and Diamond (2003, Fig 2), it takes around $2.3\,ms$ after stimulation of BCs to recording the EPSC in synaptically connected amacrine cells. In addition to the ion channel gating times of the pre- and postsynaptic membrane, the recorded $2.3\,ms$ delay includes several other time-consuming processes. Although other modeling works on the synaptic refill and release on BCs are available, (e.g., Jarsky et al., 2011, Sikora et al., 2005, Werginz and Rattay 2016), to our knowledge this is the first mathematical framework explaining transient and sustained releases together with a refill and recovery term.

To simulate vesicle release from a spiking BC, sodium and potassium ion channels were added to the axon, similar to those found in a Db4 BC in the macaque retina (Puthussery et al., 2013). The intracellular stimulation of both spiking and non-spiking BCs suggests that for small pulse amplitudes, only spiking BCs are releasing transient vesicles (Fig 5.2, Puthussery et al., 2013). Intracellular stimulation is similar to the natural situation in which BCs receive input from PRs. Here, BCs were also stimulated extracellularly, which is similar to the stimulation via electrodes of a subretinal implant (Chuang et al., 2014; Resatz

and Rattay, 2003; Werginz et al., 2015). The extracellular stimulation has some different features in proportion to the intracellular one in both passive and active membranes. The effect of extracellular stimulation generated by a single microelectrode on transient release almost suggests no difference between the responses of the spiking and non-spiking BCs in short pulses because the terminal membrane of the cells in both cases senses the same potentials originating from the microelectrode. However, spiking BCs release more transient vesicles compared to non-spiking BCs when stimulated with pulses long enough to profit from the amplification process of the spike. In addition to the signal delay, the other difference between modelCa and modelV is their number of transiently released vesicles; this decreases in modelCa for large pulse amplitudes but remains constant in the other model. This effect originates from exceeding the calcium reversal potential (Fig 5.3).

One of the deficiencies of retinal implants is the eventual reduction in contrast detection. We tested this issue by investigating the effect of extracellular periodic stimulation for inter-pulse intervals of 200 ms. For such pulse trains, only three transient vesicles are released from a single ribbon (Fig 5.4), which could explain the efficiency reduction of retinal implant types that stimulate primarily BCs and not the axons of retinal GCs. Thus, for subretinal implants, long pulses with low amplitudes may have several advantages. First, according to the intracellular simulations (which is closer to the natural situations), a passive BC is not able to release transient vesicles totally (Fig 5.2), and only some spiking BCs are the candidates to release transient vesicles in the retina. Second, we showed that extracellular stimulation has a direct effect on transient vesicle release independent of whether the cell is spiking or non-spiking, which originates from its direct effect on terminal voltage change. Finally, when the amplitude of a pulse decreases but its duration increases, a spike is generated in the cells.

Chapter 6

Conclusions

In summary, this thesis presents three computational frameworks for calculating the transmembrane voltage of two types of retinal BCs, DB4 cell in macaque's retina and rat rod BC, as well as a mathematical framework for simulation of a ribbon synapse.

6.1 Novelty of results

6.1.1 There are specific limitations in extracellular stimulation of BCs

Although few types of BCs in the primate retina are able to generate action potential, there are some especial features in these cell that make them unique among usual neurons. One of these features is the conditions under which action potential is generated during extracellular stimulation. A comparison of excitation characteristics between a DB4 BC of macaque's retina, a retinal GC, and a cortical pyramidal cell, explains the similarities and differences of conditions in extracellular stimulation. Apart from the polarity of the applied pulse in extracellular stimulation, moving a microelectrode parallel to the axon of a neuron usually causes spike generation for every position. However, for the BC this rule is not true and some positions need cathodic pulses and some positions need anodic pulses. This result maybe of interests in configuration of retinal implants.

6.1.2 Simple models can produce the same results as complex models in intracellular stimulation of BCs

The impact of the number of model compartments on simulation accuracy between single-, two-, four-, and multi-compartment models for simulation of BCs leaded to the following results:

- When a BC has a passive membrane, all of the SCM, TCM, FCM, and MCMs produce results with very small variation during intracellular stimulation. Thus, use of the simplest model, SCM in here, would be of more interests.

- For the spiking BCs (a cell with active membrane) stimulated intracellularly, FCM model can be used instead of time-consuming MCM except for the case of dendrite stimulation.

- For extracellular stimulation, only MCM should be taken into account.

6.1.3 Two different models for ribbon synapses

In subretinal implants, output of BCs play a vital role in restoring vision in the blind. The outputs of retinal bipolar cells are of two types; transient and sustained releases. Two models were presented for vesicle release from a ribbon synapse of a BC, one of the models is based on the terminal transmembrane voltage (modelV) and the other one is based on the intracellular calcium concentration of the terminal (modelCa). Each of the models explains the readily releasable pool occupancy and ignores the effected of cytoplasmic pool and ribbon. ModelV presents no delay for transient vesicle release when a stimulation is applied, while the intracellular calcium concentration has a delay of $0.43ms$ that is in agreement with experimental data. The main deficiency of the models is its time-consuming process originating from the large needed trials. Main results according to the models are:

- Both models predict that a spike makes all of the available vesicles release.

- For small stimulus amplitudes, both models produce comparable results for the number of transiently released vesicles. For extracellular stimulation using modelV, the number of transiently released vesicles increases with the pulse amplitude, while modelCa shows an opposite behavior for strong stimuli that cause calcium ion outflux when the terminal voltage exceeds the reversal potential for the Ca channels.
- Because the recovery time constant of the retinal BCs is rather large, the number of transiently released vesicles decreases during stimulation with pulse trains.

6.2 Final words

Although from the 1980s much progress has been made in retinal implants, restoration of vision using the implants still needs many research works since big parts of this field is still unknown. The presented study revealed some of these unknown phenomena and tried to bring some reasons and suggestions to deal with them. I hope I could be able to contribute to the development of future retinal neuroprostheses allowing the blind have a higher percentage of vision.

Refereces

Aradi I and Soltesz I. (2002) Modulation of network behaviour by changes in variance in interneuronal properties. J Physiol. 538:227-251.

Ayoub GS and Copenhagen DR. (1991) Application of a fluorometricmethod to measure glutamate release from single retinal photoreceptors. J. Neurosci. Methods. 37(1):7-14.

Baden T, Berens P, Bethge M, Euler T. (2013a) Spikes in mammalian bipolar cells support temporal layering of the inner retina. Curr. Biol. CB 23:48-52.

Baden T, Euler T, Weckström M, Lagnado L. (2013b) Spikes and ribbon synapses in early vision. Trends. Neurosci. 36:480-488.

Baden T, Esposti F, Nikolaev A, Lagnado L. (2011) Spikes in retinal bipolar cells phase-lock to visual stimuli with millisecond precision. Curr. Biol. 21:1859-1869.

Behrens C, Schubert T, Haverkamp S, Euler T, Berens P. (2016) Connectivity map of bipolar cells and photoreceptors in the mouse retina. Elife. 5:e20041.

Barela AJ, et al. (2006) An epilepsy mutation in the sodium channel SCN1A that decreases channel excitability. J. Neurosci. Of. J. Soc. Neurosci. 26:2714-2723.

Barnes N, Scott AF, Lieby P, et al. (2016) Vision function testing for a suprachoroidal retinal prosthesis: effects of image filtering. J. Neural. Eng. 13:036013.

Bassereh H and Rattay F. (2018a) Neurotransmitter Release from a Retinal Ribbon Synapse, a Modelling Study. MATHMOD: 9th Vienna Conference on Mathematical Modelling, Vienna, Austria, February 21-23.

Bassereh H and Rattay F. (2018b) Effect of extracellular stimulation on neurotransmitter release in a ribbon synapse. Conference Abstract: MEA Meeting 2018 — 11th International Meeting on Substrate Integrated Microelectrode Arrays. doi: 10.3389/conf.fncel.2018.38.00021.

Bassereh H and Rattay F. (2019) Two models for vesicle release from a ribbon synapse of electrically stimulated retinal bipolar cells. Submitted to Plos Computational Biology.

Benav H. (2012) Modelling effects of extracellular stimulation on retinal bipolar cells Dissertation Eberhard-Karls-Universitaet Tuebingen.

Blair E and Erlanger J. (1933) A comparison of the characteristics of axons through their individual electrical responses. Am. J. Physiol. 106:524-564 .

Boinagrov D, Pangratz-Fuehrer S, Goetz G, Palanker D. (2014) Selectivity of direct and network-mediated stimulation of the retinal ganglion cells with epi-, sub- and intraretinal electrodes. J. Neural. Eng. 11:26008.

Brindley GS and Lewin WS. (1968) The visual sensations produced by electrical stimulation of the medial occipital cortex. J. Physiol. (Lond.) 194:54-5.

Burrone J and Lagnado L. (1997) Electrical resonance and Ca^{2+} influx in the synaptic terminal of depolarizing bipolar cells from the goldfish retina. J. Physiol. 505:571-584.

Cao Y, Pahlberg J, Sarria I, Kamasawa N, Sampath AP, Martemyanov KA. (2012) Regulators of G protein signaling RGS7 and RGS11 determine the onset of the light response in ON bipolar neurons. Proc. Natl Acad. Sci. USA. 109:7905-7910.

Catterall WA, Perez-Reyes E, Snutch TP, Striessnig J. (2005) International Union of Pharmacology. XLVIII. Nomenclature and structure-function relationships of voltage-gated calcium channels. Pharmacol. Rev. 57:411-425.

Chader GJ and Michael Y. (2016) Preface: Sight restoration through stem cell therapy. Investig. Ophthalmol. Vis. Sci. 57, ORSFa1-ORSFa5.

Chen J, Shah HA, Herbert C, Loewenstein J, Rizzo JF. (2009) III Extraction of a chronically implanted, microfabricated, sub-retinal electrode array. Ophthalmic Res. 42:128-137.

Chuang AT, Margo CE, Greenberg PB. (2014) Retinal implants: a systematic re-

view Br. J. Ophthalmol. 98:852- 856.

Crank J and Nicolson P. (1947) A practical method for numerical evaluation of solutions of partial differential equations of the heat-conduction type. Proc. Camb. Phil. Soc. 43:50-67. 28.

da Cruz, Lyndon, et al. (2016) Five-year safety and performance results from the Argus II retinal prosthesis system clinical trial. Ophthalmology. 123.10:2248-2254.

Cui J and Pan ZH. (2008) Two types of cone bipolar cells express voltage-gated Na^+ channels in the rat retina. Vis. Neurosci. 25:635-645.

De Sevilla Müller LP, Liu J, Solomon A, Rodriguez A, Brecha NC. (2013) Expression of voltage-gated calcium channel $\alpha 2\delta 4$ subunits in the mouse and rat retina. J. Comp. Neurol. 521:2486-2501.

Deleuze C, et al. (2012) T-type calcium channels consolidate tonic action potential output of thalamic neurons to neocortex. J. Neurosci. Of. J. Soc. Neurosci. 32:12228-12236.

Demb JB, Singer JH. (2015) Functional circuitry of the retina. Annu. Rev. Vis. Sci. 1:263-289.

DeVries SH, Li W, Saszik S. (2006) Parallel processing in two transmitter microenvironments at the cone photoreceptor synapse. Neuron. 50:735-748.

tom Dieck S and Brandstaetter JH. (2006) Ribbon synapses of the retina. Cell. Tiss. Res. 326:339-346.

Dobelle WH and Mladejovsky MG. (1974) Phosphenes produced by electrical stimulation of human occipital cortex, and their application to the development of a prosthesis for the blind. J. Physio.l 243:553-576.

Dowling JE and Boycott BB. (1966) Organization of the primate retina: electron microscopy. Proc R Soc London B, Biol. Sci. 166:80-111.

Duebel J, Haverkamp S, Kuner T, Euler T. (2006) Two-photon imaging reveals somatodendritic chloride gradient in retinal ON-type bipolar cells expressing the biosensor

clomeleon. Neuron. 49:81-94.

Einstein A. (1905) Über die von der molekulartheoretischen Theorie der Wärme geforderte Bewegung von in ruhenden FlÃ¼ssigkeiten suspendierten Teilchen.Ann. Phys. Leipzig17,549.

Encke J, Benav H, Werginz P, Zrenner E, Rattay F. (2013) Investigating the influence of 3D cell morphology on neural response during electrical stimulation. Biomedizinische Technik, 58 (1A).

Euler T, Haverkamp S, Schubert T, Baden T. (2014) Retinal bipolar cells: elementary building blocks of vision. Nat. Rev. Neurosci. 15:507-519.

Famiglietti EV and Kolb H. (1975) A bistratified amacrine cell and synaptic circuitry in the inner plexiform layer of the retina. Brain. Res. 84:293-300.

Field GD and Rieke F. (2002) Nonlinear signal transfer from mouse rods to bipolar cells and implications for visual sensitivity. Neuron, 34(5):773-785.

FitzGibbon T. (2017) Retinal prosthesis that incorporates the organization of the nerve fbre layer. Clin. Experiment. Ophthalmol. 45:401-408.

Fohlmeister JF, Coleman PA, Miller RF. (1990) Modelling the repetitive firing of retinal ganglion cells. Brain. Res. 510:343-5.

Foerster O. (1929) Beitrage zur Pathophysiologie der Sehbahn und der Sehsphare. J. Psychol. Neurol. Lpz. 39:463.

Freeman DK, Jeng JS, Kelly SK, Hartveit E, Fried SI. (2011) Calcium channel dynamics limit synaptic release in response to prosthetic stimulation with sinusoidal waveforms. J. Neural. Eng. 8(4):046005.

Fried SI, Lasker ACW, Desai NJ, Eddington DK, Rizzo JF. (2009) Axonal sodium-channel bands shape the response to electric stimulation in retinal ganglion cells. J. Neurophysiol. 101:1972-1987.

Grabner CP, Ratliff CP, Light AC, DeVries SH. (2016) Mechanism of High-Frequency Signaling at a Depressing Ribbon Synapse. Neuron. 91:133-145.

Graydon CW, Zhang J, Oesch NW, Sousa AA, Leapman RD, Diamond JS. (2014) Passive diffusion as a mechanism underlying ribbon synapse vesicle release and resupply. J. Neurosci. 34(27):8948-62.

Greenberg, RJ, Velte TJ, Humayun MS, Scarlatis GN, e Juan E. (1999) A computational model of electrical stimulation of the retinal ganglion cell. IEEE Trans. Biomed. Eng. 46:505-514.

Greschner M, Field GD, Li PH, Schiff ML, Gauthier JL, Ahn D, Sher A, Litke AM, Chichilnisky EJ. (2014) A polyaxonal amacrine cell population in the primate retina. J. Neurosci. 34:3597-3606.

Guo T, Tsai D, Bai S, Morley JW, Suaning GJ, Lovell NH, Dokos S. (2014) Understanding the retina: A review of computational models of the retina from the single cell to the network level. Crit. Rev. Biomed. Eng. 42(5):419-436.

Gustafsson B and Jankowska E. (1976) Direct and indirect activation of nerve cells by electrical pulses applied extracellularly. J. Physiol. 258:33-61.

Hama K. (1965) Some observations on the fine structure of the lateral line organ of the Japanese sea eel Lyncozymba nystromi. J. Cell. Biol. 24:193-210.

Hartveit E. (1999) Reciprocal synaptic interactions between rod bipolar cells and amacrine cells in the rat retina. J Neurophysiol. 81:2923-2936.

Haverkamp S, Ghosh KK, Hirano AA, Wassle H. (2003) Immunocytochemical description of five bipolar cell types of the mouse retina. J. Comp. Neurol. 455(4):463-76.

Haverkamp S, Grünert U, WÃ¤ssle H. (2000) The cone pedicle, a complex synapse in the retina. Neuron. 27:85-95.

Haverkamp S, Grünert U, WÃ¤ssle H. (2001) Localization of kainate receptors at the cone pedicles of the primate retina. J. Comp. Neurol. 436:471-486.

Heidelberger R, Thoreson WB, Witkovsky P. (2005) Synaptic transmission at retinal ribbon synapses. Prog. Retin. Eye. Res. 24:682-720.

Helmholtz H. (1850) Messungen uber den zeitlichen Verlauf der Zuckung animalischer Muskeln und die Fortpflanzungsgeschwindigkeit der Reizung in den Nerven. Archiv für Anatomie, Physiologie und wissenschaftliche Medicin. 276:17

Hellmer CB, Zhou Y, Fyk-Kolodziej B, Hu Z, Ichinose T. (2016) Morphological and Physiological Analysis of Type-5 and Other Bipolar Cells in the Mouse Retina. Neurosci. 315:246-258.

Hirasawa H, Shiells R, Yamada M. (2002) A metabotropic glutamate receptor regulates transmitter release from cone presynaptic terminals in carp retinal slices. J. Gen. Physiol. 119(1):55-68.

Hodgkin AL and Huxley AF. (1952) A quantitative description of membrane current and its application to conduction and excitation in nerve. J. Physiol. 117:500-544.

Hu HJ and Pan ZH (2002) Differential expression of K^+ currents in mammalian retinal bipolar cells. Vis. Neurosci. 19:163-173.

Hu W, et al. (2009) Distinct contributions of Na(v)1.6 and Na(v)1.2 in action potential initiation and backpropagation. Nat. Neurosci. 12:996-1002.

Hu C, Bi A, Pan ZH. (2009) Differential expression of three T-type calcium channels in retinal bipolar cells in rats. Vis. Neurosci. 26:177-87.

Ichinose T, Fyk-Kolodziej B, Cohn J. (2014) Roles of on cone bipolar cell subtypes in temporal coding in the mouse retina. J. Neurosci. 34:8761-8771.

Isaacson W. (2003) Benjamin Franklin: An American Life. Simon and Schuster.

Ishihara A. (2017) Simulation Analysis of Temporal Coding by Ionotropic Glutamate Receptors of Retinal OFF-type Bipolar Cells. Sensors and Materials. 30(2):299-313.

Ishihara A, Kamiyama Y, Usui S. (1998) Analysis of light responses at the retinal bipolar cells based on ionic current model. In: Bower J (ed) Computational neuroscience: trends in research. Plenum Press, New York, 203-209.

Ishihara A, Kamiyama Y, Usui S. (2003) the role of ionic currents in shaping light

responses of retinal bipolar cell. In: Kaneko A. (eds) The neural basis of early vision. Keio University International Symposia for Life Sciences and Medicine, vol 11. Springer, Tokyo.

Ivanova E, Müller F. (2006) Retinal bipolar cell types differ in their inventory of ion channels. Vis. Neurosci. 23:143-154.

Jarsky T, Cembrowski M, Logan SM, Kath WL, Riecke H, Demb JB, Singer JH. (2011) A synaptic mechanism for retinal adaptation to luminance and contrast. J. Neurosci. 31:11003-11015.

Jeng J, Tang S, Molnar A, Desai, NJ, Fried SI. (2011) Te sodium channel band shapes the response to electric stimulation in retinal ganglion cells. J. Neural Eng. 8:36022.

Kaneko A, Pinto LH, Tachibana M. (1989) Transient calcium current of retinal bipolar cells of the mouse. Journal of physiology, 410(1):613-629.

Kandel ER. (2000) Principles of neural science (4th ed.). New York: McGraw-Hill, Health Professions Division.

Kasi H, et al. (2011) Direct localised measurement of electrical resistivity profle in rat and embryonic chick retinas using a microprobe. J. Electr. Bioimpedance 1, 84-92.

Katz PS, Kirk MD, Govind CK. (1993) Facilitation and depression at different branches of the same motor axon: evidence for presynaptic differences in release. J. Neurosci. 13:3075-89.

Kidd M. (1962) Electron microscopy of the inner plexiform layer of the retina in the cat and the pigeon. J. Anat. 96:179-87.

Klumpp DJ, Song EJ, Ito S, Sheng MH, Jan LY, Pinto LH. (1995) The Shaker-like potassium channels of the mouse rod bipolar cell and their contributions to the membrane current. J. Neurosci. 15:5004-5013.

Koike C, Numata T, Ueda H, Mori Y, Furukawa T. (2010) TRPM1: a vertebrate TRP channel responsible for retinal ON bipolar function. Cell Calcium. 48:95-101.

Kolb H and Nelson R. (1983) Rod pathways in the retina of the cat. Vision. Res. 23:301-312.

Kolb H, Nelson R, Mariani A. (1981) Amacrine cells, bipolar cells and ganglion cells of the cat retina: a Golgi study. Vision Res. 21:1081-1114.

Kosaka T and Ikeda K. (1983) Possible temperature-dependent blockage of synaptic vesicle recycling induced by a single gene mutation in Drosophila. J. Neurobiol. 14:207-25.

Kutta M. (1901) Beitrag zur näherungsweisen Integration totaler Differentialgleichungen. Zeitschrift für Mathematik und Physik. 46:435-453. 28.

Lagnado L, Gomis A, Job C. (1996) Continuous vesicle cycling in the synaptic terminal of retinal bipolar cells. Neuron. 17:957-967.

Lasater EM. (1988) Membrane currents of retinal bipolar cells in culture. Journal of Neurophysiology, 60(4):1460-1480.

Lee KS and Tsien RW. (1982) Reversal of current through calcium channels in dialysed single heart cells. Nat. 297:498-501.

Lewis, Philip M, Jeffrey V, Rosenfeld. (2016) Electrical stimulation of the brain and the development of cortical visual prostheses: an historical perspective. Brain. research. 1630:208-224.

Lane FJ, Nitsch K, Huyck M, Troyk P, Schug K. (2016) Perspectives of optic nerve prostheses. Disab. Rehabil. Assist. Technol. 11:301-309.

Le Roy C. (1755) Hist Acad Roy Sciences Memoires Math Phys. 60:87-95.

Li YN, Tsujimura T, Kawamura S, Dowling JE. (2012) Bipolar cell-photoreceptor connectivity in the zebrafish (Danio rerio) retina. J. Comp. Neurol. 520:3786-3802.

Light AC and DeVries SH. (2007) Light Responses in Ground Squirrel b2 and b3 Off Bipolar Cells, Inv Oph Vis Sci. 48: 5958.

Light AC, Zhu Y, Shi J, Saszik S, Lindstrom S, Davidson L, Li X, Chiodo VA,

Hauswirth WW, Li W, DeVries SH. (2012) Organizational motifs for ground squirrel cone bipolar cells. J. Comp. Neurol. 520:2864-2887.

LoGiudice L, Sterling P, Matthews G. (2008) Mobility and turnover of vesicles at the synaptic ribbon. J Neurosci. 28:3150-3158.

Logiudice L, Sterling P, Matthews G. (2009) Vesicle recycling at ribbon synapses in the finely branched axon terminals of mouse retinal bipolar neurons. Neurosci. 164:1546-1556.

Ma YP, Cui J, Hu HJ, Pan ZH. (2003) Mammalian retinal bipolar cells express inwardly rectifying K^+ currents (IKir) with a different distribution than that of Ih. J. Neurophysiol. 90:3479-3489.

Mainen ZF and Sejnowski TJ. (1996) Infuence of dendritic structure on fring pattern in model neocortical neurons. Nature. 382:363-366.

Masu M, et al. (1995) Specific deficit of the ON response in visual transmission by targeted disruption of the mGluR6 gene. Cell. 80:757-765.

Masland RH. (2012) The tasks of amacrine cells. Vis Neurosci. 29:3-9.

Matthews G and Fuchs P. (2010) The diverse roles of ribbon synapses in sensory neurotransmission. Nat. Rev. Neurosci. 11:812-822.

Maxeiner S, Luo F, Tan A, Schmitz F, Sudhof TC. (2016) How to make a synaptic ribbon: RIBEYE deletion abolishes ribbons in retinal synapses and disrupts neurotransmitter release. EMBO J. 35:1098-1114.

Mennerick S and Matthews G. (1996) Ultrafast exocytosis elicited by calcium current in synaptic terminals of retinal bipolar neurons. Neuron. 17:1241-1249.

Myatt DR, Hadlington T, Ascoli GA, Nasuto SJ. (2012) Neuromantic - from semi-manual to semi-automatic reconstruction of neuron morphology. Frontiers in neuroinformatics. 6(4).

Mennerick S, Zenisek D, Matthews G. (1997) Static and dynamic membrane properties of large-terminal bipolar cells from goldfish retina: experimental test of a com-

partment model. J. Neurophysiol 78:51- 62.

Müller F, Scholten A, Ivanova E, Haverkamp S, Kremmer E, Kaupp UB. (2003) HCN channels are expressed differentially in retinal bipolar cells and concentrated at synaptic terminals. Eur. J. Neurosci. 17:2084-2096.

Nelson R and Kolb H. (1985) A17: a broad-field amacrine cell in the rod system of the cat retina. J. Neurophysiol. 54:592-614.

Neves G and Lagnado L. (1999) The kinetics of exocytosis and endocytosis in the synaptic terminal of goldfish retinal bipolar cells. J. Physiol. 515:181-202.

Newkirk GS, Hoon M, Wong RO, Detwiler PB. (2013) Inhibitory inputs tune the light response properties of dopaminergic amacrine cells in mouse retina. J. Neurophysiol. 110:536-552.

Nguyen Hieu T, et al. (2016) Thalamic visual prosthesis. IEEE Trans. Biomed. Eng. 63.8:1573-1580.

Nowak LG and Bullier J. (1998) Axons, but not cell bodies, are activated by electrical stimulation in cortical gray matter. I. Evidence from chronaxie measurements. Exp. Brain Res. 118:477-488.

Oesch NW, Diamond JS. (2011) Ribbon synapses compute temporal contrast and encode luminance in retinal rod bipolar cells. Nat. Neurosci. 14(12):1555-61.

Oltedal L, Morkve SH, Veruki ML, Hartveit E. (2007) Patch-Clamp Investigations and Compartmental Modeling of Rod Bipolar Axon Terminals in an In Vitro Thin-Slice Preparation of the Mammalian Retina. J. Neurophysiol. 97:1171-1187.

Oltedal L, Veruki ML, Hartveit E. (2009) Passive membrane properties and electrotonic signal processing in retinal rod bipolar cells J. Physiol. 587:829-49.

Oltedal L, Veruki ML, Hartveit E. (2009) Passive membrane properties and electrotonic signal processing in retinal rod bipolar cells. J. Physiol. 587:829-849.

Osterberg G. (1935) Topography of the layer of rods and cones in the human retina. Acta Ophtalmol, 13:1-103.

Palmer MJ, Hull C, Vigh J, von Gersdorff H. (2003) Synaptic cleft acidification and modulation of short-term depression by exocytosed protons in retinal bipolar cells. J Neurosci. 23:11332-11341.

Pan ZH. (2000) Differential expression of high- and two types of low-voltage-activated calcium currents in rod and cone bipolar cells of the rat retina. J Neurophysiol. 83:513-527.

Pan ZH. (2001) Voltage-activated Ca^{2+} channels and ionotropic GABA receptors localized at axon terminals of mammalian retinal bipolar cells. Vis. Neurosci. 18:279 -288.

Panetsos F, Sanchez-Jimenez A, Cerio ED, Diaz-Guemes I, Sanchez FM. (2011) Consistent phosphenes generated by electrical microstimulation of the visual thalamus. An experimental approach for thalamic visual neuroprostheses. Front Neurosci. 5:84.

Pang JJ, Gao F, Wu SM. (2012) Ionotropic glutamate receptors mediate OFF responses in light-adapted ON bipolar cells. Vision. Res. 68:48-58.

Pearring JN, et al. (2011) A role for nyctalopin, a small leucine-rich repeat protein, in localizing the TRP melastatin 1 channel to retinal depolarizing bipolar cell dendrites. J. Neurosci. 31:10060-10066.

Polyak SL. The Retina. The University of Chicago Press (1941), Chicago.

Popova E. (2014) Ionotropic GABA receptors and distal retinal ON and OFF responses. Scientifica (Cairo) 149187.

Prochazka A, Mushahwar VK, McCreery BB. (2001) Neural prostheses. J. Physiol. 533:99-109.

Prokop A and Meinertzhagen IA. (2006) Development and structure of synaptic contacts in Drosophila. Semin. Cell. De.v Biol. 17:20-30.

Protti DA and Llano I. (1998) Calcium currents and calcium signaling in rod bipolar cells of rat retinal slices. J. Neurosci. 18:3715-3724.

Publio R, Oliveira RF, Roque AC. (2009) A computational study on the role of gap junctions and rod Ih conductance in the enhancement of the dynamic range of the retina. PloS One. 4(9):e6970.

Puthussery T, Venkataramani S, Gayet-Primo J, Smith RG, Taylor WR. (2013) NaV1. 1 channels in axon initial segments of bipolar cells augment input to magnocellular visual pathways in the primate retina. J. Neurosci. 33(41):16045-16059.

Quigley HA, Addicks EM, Green WR. (1982) Optic nerve damage in human glaucoma, III: quantitative correlation of nerve fiber loss and visual field defect in glaucoma, ischemic neuropathy, disc edema, and toxic neuropathy. Arch Ophthalmol. 100:135-146.

Rall W. (1964) Neural Theory and Modeling, chap. Theoretical significance of dendritic trees for neuronal input-output relations, 73-97. Stanford University Press. 17

Rampino MA and Nawy SA. (2011) Relief of Mg^{2+}-dependent inhibition of TRPM1 by PKCα at the rod bipolar cell synapse. J. Neurosci. 31:13596-13603.

Ramsden CM, et al. (2013) Stem cells in retinal regeneration: past, present and future. Development. 140:2576-2585.

Ranck JB. (1975) Which elements are excited in electrical stimulation of mammalian central nervous system: a review. Brain Res. 98:417-440.

Rattay F. (1986) Analysis of models for external stimulation of axons. IEEE Trans. Biomed. Eng. 33:974-977.

Rattay F. (1990) Electrical Nerve Stimulation. Springer.

Rattay F. (1999) The basic mechanism for the electrical stimulation of the nervous system. Neurosci. 89(2):335-46.

Rattay F. (2014) On the upper threshold phenomenon of extracellular neural stimulation. J. Neurophysiol. 112:2664-2665.

Rattay F, Bassereh H, Fellner A. (2017) Impact of electrode position on the elicitation of sodium spikes in retinal bipolar cells. Sci. Rep. 7:17590.

Rattay F, Bassereh H, Stiennon I. (2018) Compartment models for the electrical stimulation of retinal bipolar cells. PLoS ONE. 13(12):e0209123.

Rattay F., Greenberg RJ, Resatz S. (2002) Neuron modeling. In Handbook of Neuroprosthetic Methods. CRC Press.

Rattay F, Paredes LP, Leao RN. (2012) Strength-duration relationship for intra-versus extracellular stimulation with microelectrodes. Neuroscience, 214:1-13.

Rattay F, Resatz S, Lutter P, Minassian K, Jilge B, Dimitrijevic MR. (2003) Mechanisms of electrical stimulation with neural prostheses. Neuromodulation. 6:42-56.

Rattay F and Resatz S. (2004) Efective electrode confguration for selective stimulation with inner eye prostheses. IEEE Trans. Biomed. Eng. 51:1659-1664.

Rattay F and Wenger C. (2010) Which elements of the mammalian central nervous system are excited by low current stimulation with microelectrodes? Neuroscience 170:399-407.

Regus-Leidig H and Brandstatter JH. (2012) Structure and function of a complex sensory synapse. Acta. Physiol. 204:479-486.

Resatz S and Rattay F. (2003) Excitability of bipolar and ganglion cells with retinal prosthesis: a modeling study. In Proceedings of the 25th Annual International Conference of the IEEE Engineering in Medicine and Biology Society. IEEE 3:2039-2042.

Saszik S and DeVries SH. (2012) A mammalian retinal bipolar cell uses both graded changes in membrane voltage and all-or-nothing Na^+ spikes to encode light. J. Neurosci. 32:297-307.

Schmitz F. (2009) The making of synaptic ribbons: how they are built and what they do. Neuroscientist. 15:611-624.

Sekhar S, Jalligampala A, Zrenner E, Rathbun DL. (2016) Tickling the retina: integration of subthreshold electrical pulses can activate retinal neurons. J. Neural Eng. 13:46004.

Sekirnjak C. et al. (2008) High-resolution electrical stimulation of primate retina for epiretinal implant design. J. Neurosci. Of. J. Soc. Neurosci. 28:4446-4456.

Sheasby BW and Fohlmeister JF. (1999) Impulse encoding across the dendritic morphologies of retinal ganglion cells. J. Neurophysiol. 81:1685-1698.

Shepherd RK, Shivdasani MN, Nayagam DA, Williams CE, Blamey PJ. (2013) Visual prostheses for the blind. Trends Biotechnol. 31:562-571.

Sikora MA, Gottesman J, Miller RF. (2005) A computational model of the ribbon synapse. J. Neurosci. Methods 145:47-61.

Singer JH, Lassova L, Vardi N. Diamond JS. (2004) Coordinated multivesicular release at a mammalian ribbon synapse. Nat. Neurosci. 7:826-833.

Singer JH and Diamond JS. (2003) Sustained Ca^{2+} entry elicits transient postsynaptic currents at a retinal ribbon synapse. J. Neurosci. 23:10923-10933.

Singer JH and Diamond JS. (2006) Vesicle depletion and synaptic depression at a mammalian ribbon synapse. J. Neurophysiol. 95:3191-3198.

Sjostrand FS. (1953) The ultrastructure of the retinal rod synapses of the guinea pig eye. J. Appl. Phys. 24:1422.

Sjostrand FS. (1958) Ultrastructure of retinal rod synapses of the guinea pig eye as revealed by three-dimensional reconstructions from serial sections. J. Ultrastruct. Res. 2:122-70.

Smith CA and Sjostrand FS. (1961) Structure of the nerve endings on the external hair cells of the guinea pig cochlea as studied by serial sections. J. Ultrastruct. Res. 5:523-56.

Soto F, Bleckert A, Lewis R, Kang Y, Kerschensteiner D, Craig AM, Wong RO. (2011) Coordinated increase in inhibitory and excitatory synapses onto retinal ganglion cells during development. Neural Dev. 6:31.

Spampanato J, Aradi I, Soltesz I, Goldin AL. (2004) Increased neuronal fring in computer simulations of sodium channel mutations that cause generalized epilepsy with

febrile seizures plus. J. Neurophysiol. 91:2040-2050.

Spiwoks-Becker I, Vollrath L, Seeliger MW, Jaissle G, Eshkind LG, Leube RE. (2001) Synaptic vesicle alterations in rod photoreceptors of synaptophysin-deficient mice. Neurosci. 107:127-142.

Sterling P and Matthews G. (2005) Structure and function of ribbon synapses. Trends. Neurosci. 28:20-29.

Strettoi E, Novelli E, Mazzoni F, Barone I, Damiani D. (2010) Complexity of retinal cone bipolar cells. Prog. Retin. Eye. Res. 29:272-283.

Sterratt D, Graham B, Gillies A, Willshaw D. (2011) Principles of Computational Modelling in Neuroscience. Cambridge University Press.

Stuart GJ and Sakmann B. (1994) Active propagation of somatic action potentials into neocortical pyramidal cell dendrites. Nature 367:69-72.

Sulaiman P. Xu Y. Fina M.E. Tummala S.R. Ramakrishnan H. Dhingra A. Vardi N. (2013) Kir2.4 surface expression and basal current are affected by heterotrimeric G-proteins. J. Biol. Chem. 288:7420-7429.

Szule JA, Harlow ML, Jung JH, De-Miguel FF, Marshall RM, McMahan UJ. (2012) Regulation of synaptic vesicle docking by different classes of macromolecules in active zone material. PLoS ONE 7:e33333.

Tessier-Lavigne M. (2000) Phototransduction and information processing in the retina. Principles of Neural Science. E. Kandel. 3:400-416.

Tessier-Lavigne M, Attwell D, Mobbs P, Wilson M. (1988) Membrane currents in retinal bipolar cells of the axolotl. The Journal of general physiology, 91(1):49-72.

Tsukamoto Y, Morigiwa K, Ueda M, Sterling P. (2001) Microcircuits for night vision in mouse retina. J Neurosci. 21:8616-8623.

Tsukamoto Y and Omi N. (2015) OFF bipolar cells in macaque retina: type-specific connectivity in the outer and inner synaptic layers. Frontiers in neuroanatomy 9:122.

Tsukamoto Y and Omi N. (2016) ON bipolar cells in macaque retina: type-specific synaptic connectivity with special reference to off counterparts. Front. Neuroanat. 10:104.

Thomson W. (1854) On the theory of the electric telegraph. Proceedings of the Royal Society of London , 7:382-399.

Thoreson WB. (2000) Dihydropyridine-sensitive calcium currents in bipolar cells of salamander retina are inhibited by reductions in extracellular chloride. Neurosci. Lett. 280:155-8.

Usui S, Ishihara A, Kamiyama Y, Ishii H. (1996) Ionic current model of bipolar cells in the lower vertebrate retina. Vision Res 36:4069-4076.

Uzzell VJ and Chichilnisky EJ. (2004) Precision of Spike Trains in Primate Retinal Ganglion Cells. J Neurophysiol 92:780-789.

Veraart C, Raftopoulos C, Mortimer JT, Delbeke J, Pins D, et al. (1998) Visual sensations produced by optic nerve stimulation using an implanted self-sizing spiral cuff electrode. Brain Res. 813:181-86.

Veruki ML, Morkve SH, Hartveit E. (2006) Activation of a presynaptic glutamate transporter regulates synaptic transmission through electrical signaling. Nat. Neurosci. 9:1388-96.

Vielma AH and Schmachtenberg O. (2016) Electrophysiological fingerprints of OFF bipolar cells in rat retina. Sci. Rep. 6:30259.

Vollrath L and Huss H. (1973) The synaptic ribbons of the guinea-pig pineal gland under normal and experimental conditions. Z. Zellforsch. Mikrosk. Anat. 139:417-29.

Von Gersdorff H. (2001) Synaptic ribbons: versatile signal transducers. Neuron. 29:7-10.

von Gersdorff H and Matthews G. (1996) Calcium-dependent inactivation of calcium current in synaptic terminals of retinal bipolar neurons. J. Neurosci. 16:115-122.

Wan QF, Vila A, Zhou ZY, Heidelberger R. (2008) Synaptic vesicle dynamics in

mouse rod bipolar cells. Vis Neurosci. 25:523-533.

Wan QF, Zhou ZY, Thakur P, Vila A, Sherry DM, Janz R, Heidelberger R. (2010) SV2 Acts via Presynaptic Calcium to Regulate Neurotransmitter Release. Neuron. 66:884-895.

Wachtel AW and Szamier RB. (1966) Special cutaneous receptor organs of fish: the tuberous organs of Eigenmannia. J. Morphol. 119:51-80.

Walston ST, Chow RH, Weiland JD. (2015) Patch clamp recordings of retinal bipolar cells in response to extracellular electrical stimulation in wholemount mouse retina. Conf. Proc. Annu. Int. Conf. IEEE Eng. Med. Biol. Soc. IEEE Eng. Med. Biol. Soc. Annu. Conf. 3363-3366.

Weiland JD, Liu W, Humayun MS. (2005) Retinal prosthesis. Annu Rev Biomed Eng. 7:361-401.

Werginz P. (2016) Neuronal activation characteristics in the electrically stimulated retina : a model-based study. Thesis.

Werginz P, Benav H, Zrenner E, Rattay F. (2015) Modeling the response of ON and OFF retinal bipolar cells during electric stimulation Vis. Res. 111:170-81.

Werginz P and Rattay F. (2015) Past, present, future: a review on visual prostheses Minerva Med. 106:65-77.

Werginz P and Rattay F. (2016) The impact of calcium current reversal on neurotransmitter release in the electrically stimulated retina. J. Neural. Eng. 13(4):046013.

Werginz P, Fried SI, Rattay F. (2014) Influence of the sodium channel band on retinal ganglion cell excitation during electric stimulation-a modeling study. Neuroscience. 266:162-177.

Wersall J, Flock A, Lundquist PG. (1965) Structural basis for directional sensitivity in cochlear and vestibular sensory receptors. Cold Spring Harb Symp Quant Biol. 30:115-32.

Zhang H, Holden AV, Kodam I, Honjo H, Lei M, Varghese T, Boyett MR. (2000)

Mathematical models of action potentials in the periphery and center of the rabbit sinoatrial node. Am. J. Physiol. Heart Circ. Physiol. 279:H397-421.

Appendix A

Python programs samples

Python program for single compartment model with active membrane and surface are of 300 μm^2

```
from pylab import *
import numpy as np

V_rest=-65.  #mV
Surface=300*1e-8 #cm
Pulse_amplitude= 20*1e-6  #uA (20pA)


Cm  =   1.0
gbar_Na = 120.0  #m/cm2
gbar_K  =  36.0  #m/cm2
gbar_l  =   0.3  #m/cm2
E_Na =  50.0   #mV
E_K  = -77.0   #mV
E_l  = -54.387 #mV
Ra=0.1   #kohm.cm

T     = 100    # ms
dt    = 0.001 # ms
time  = np.arange(0,T+dt,dt)


def alpha_m( V):
        return 0.1*(V+40.0)/(1.0 - np.exp(-(V+40.0) / 10.0))
```

```
def beta_m( V):
        return 4.0*np.exp(-(V+65.0) / 18.0)
def m_inf(v) : return alpha_m(v)/(alpha_m(v) + beta_m(v))

def alpha_h( V):
        return 0.07*np.exp(-(V+65.0) / 20.0)

def beta_h( V):
        return 1.0/(1.0 + np.exp(-(V+35.0) / 10.0))

def h_inf(v) : return alpha_h(v)/(alpha_h(v) + beta_h(v))


def alpha_n( V):
        return 0.01*(V+55.0)/(1.0 - np.exp(-(V+55.0) / 10.0))

def beta_n( V):
        return 0.125*np.exp(-(V+65) / 80.0)

def n_inf(v) : return alpha_n(v)/(alpha_n(v) + beta_n(v))



############################################## i_stim ###################################
I = np.zeros(len(time))
for i, t in enumerate(time):
 if 10<=t<=80: I[i] = Pulse_amplitude/Surface # uA/cm2
#########################################################################################


Vm      = np.zeros(len(time))  # mV
Vm[0] = V_rest



m       = m_inf(V_rest)
h       = h_inf(V_rest)
n       = n_inf(V_rest)

for i in range(0,len(time)-1):
  g_Na  = gbar_Na*(m**3)*h
  g_K   = gbar_K*(n**4)
  g_l   = gbar_l
  m += dt*(alpha_m(Vm[i])*(1 - m) - beta_m(Vm[i])*m)
```

```
  h += dt*(alpha_h(Vm[i])*(1 - h) - beta_h(Vm[i])*h)
  #n += dt*(alpha_n(Vm[i])*(1 - n) - beta_n(Vm[i])*n)#forward euler method
  n = (n+dt*alpha_n(Vm[i]))/(1 + (alpha_n(Vm[i])+ beta_n(Vm[i]))*dt)#backward euler method
  dV = -(g_Na * (Vm[i] - E_Na)+ g_K  * (Vm[i] - E_K )+ g_l  * (Vm[i] - E_l )) +I[i]
#potansiele har element dar har zaman
  Vm[i+1] = Vm[i] + dt * dV / Cm


#ylim(-70,-60)
plot(time,Vm)
show()
```

Python program for the three compartment model presented at methods

```
import numpy as np
import networkx as nx
from pylab import *



pulse_amplitude=20*1e-6
T     =120.
dt    = 0.01
time  = np.arange(0,T+dt,dt)


t0_stim=10.  #pulse starts
t1_stim=70.  #pulse finishes


V_rest=-60.    #resting membrane
E_l=-60.
n_th=0                  # the compartment in which the current is injected
Cm      = 1.            # uF/cm^2
RA      = .1            # kOhm*cm
g_l=0.1                 # mS/cm^2


################################################
data=np.loadtxt('file.swc')
```

```
ID = data[:,0]
type_compartment=data[:,1]
x_cord=data[:,2]*1e-4#cm
y_cord=data[:,3]*1e-4#cm
z_cord=data[:,4]*1e-4#cm
radius=data[:,5]*1e-4#cm
partner = data[:,6]



NON=len(ID)  #NON==number of nodes

###################### lenght of each compartments    ##############
Lenghts=np.zeros(NON)  #we consider that the first elemet is soma type without lenght
for i in range(NON):
  if partner[i]==-1:
   l=0
  else:
   l=np.sqrt((x_cord[int(ID[i]-1)]-x_cord[int(partner[i]-1)])**2 +\
             (y_cord[int(ID[i]-1)]-y_cord[int(partner[i]-1)])**2 +\
             (z_cord[int(ID[i]-1)]-z_cord[int(partner[i]-1)])**2 )
  Lenghts[i]=l


#for i in range(NON):
# print round(Lenghts[i]*1e4,5)
##############   Midpoints ######################
x_mid=np.zeros(NON)
y_mid=np.zeros(NON)
z_mid=np.zeros(NON)

for i in range(NON):
  if partner[i]==-1:
   x_mid[int(ID[i]-1)]=0
   y_mid[int(ID[i]-1)]=0
   z_mid[int(ID[i]-1)]=0
  else:
   x_mid[int(ID[i]-1)]=(x_cord[int(ID[i]-1)]+x_cord[int(partner[i]-1)])/2.
   y_mid[int(ID[i]-1)]=(y_cord[int(ID[i]-1)]+y_cord[int(partner[i]-1)])/2.
   z_mid[int(ID[i]-1)]=(z_cord[int(ID[i]-1)]+z_cord[int(partner[i]-1)])/2.


#for i in range(NON):
# print x_mid[i],'\t',y_mid[i],'\t',z_mid[i]*1e4
################## elimination of the first elements ############################
```

```
ID=ID-1          #reducing one number from each node
partner=partner-1  #reducing one number from each partner
ID=ID[1:]
radius=radius[1:]
x_mid=x_mid[1:]
y_mid=y_mid[1:]
z_mid=z_mid[1:]
type_compartment=type_compartment[1:]
Lenghts=Lenghts[1:]
partner=partner[1:]

for i in range(len(partner)):
  if partner[i]==0:
   partner[i]=1


##################  resistance of each element    ####################################
Resistance=np.zeros(NON-1)
for i in range(NON-1):
   Resistance[i]=(RA*Lenghts[i])/(np.pi*radius[i]**2)
   #print Resistance[i]


################# Surface area of each element ######################################
Surface=np.zeros(NON-1)
for i in range(NON-1):
   Surface[i]=2.*np.pi*radius[i]*Lenghts[i] #in 10 ra baadan pak kon
   #print Surface[i]*1e8
###################  Making adjancy matrix   ####################################

ppz=[]
for i in range(NON-1): #NON-1=number of compartments
   ppz.append([int(ID[i]),int(partner[i])])
ppz=ppz[1:]
G = nx.Graph(ppz)


neibor_Mat= 1.*nx.adjacency_matrix(G)
#Con_Mat=np.asarray(neibor_Mat) #in some version of numpy, this should be used
Con_Mat=neibor_Mat.toarray()
#print neibor_Mat.todense()

#print Con_Mat

#################### makig g_L  vectors   ####################################
```

```
gbar_l_vec=np.ones(NON-1)*g_l #sourcesh Paul

################## making final axial matrix (M) ####################################


MM=np.zeros([NON-1,NON-1])
for i in range(NON-1):
  for j in range(NON-1):
      MM[i][j]=(-Con_Mat[i][j])/(Resistance[i]/2.+Resistance[j]/2.)


for i in range(NON-1):
 element_ij=0.
 for j in range(NON-1):
    if MM[i][j] !=0.:
       element_ij=element_ij+MM[i][j]
 MM[i][i]=-1.*(element_ij)



for i in range(NON-1):
  MM[i]=MM[i]/Surface[i]


#print MM
################# i_stim ###################################
curr_Am=pulse_amplitude/Surface[n_th]
III = np.zeros(len(time))
for i, t in enumerate(time): #in khato nabayad 'for i in range(len(I))' nevesht
  if t0_stim<=t<=t1_stim: III[i] =curr_Am
######################     Voltage calculation by Backward    #############
Vm      = np.zeros([NON-1,len(time)])  # mV
Vm[:,0] = V_rest
dV      = np.zeros(NON-1)              # mV


II=np.identity(NON-1)
II_MM=II+(MM*dt/Cm)
Inv_MM=np.linalg.inv(II_MM)



for i in range(0,len(time)-1):
  dV =-( gbar_l_vec*(Vm[:,i]-E_l))
  dV[n_th] = dV[n_th]+III[i+1]
```

```
  Vm[:,i+1] = np.dot(Inv_MM,(Vm[:,i] + dt * dV / Cm))

plot(time,Vm[0])#soma
#plot(time,Vm[1])#axon
#plot(time,Vm[2])#terminal
show()
```

Appendix B

Curriculum Vitae

Profile

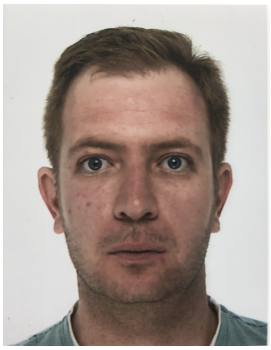

Hassan Bassereh

Email: Hassanbassereh@gmail.com

Date of Birth: 19.09.1989, Shahreza

Nationality: Iran

Education

6.2016 - present	Doctoral student (Dr. techn., PhD) - *Computational Neuroscience and Biomedical Engineering* Vienna University of Technology
2012 - 2015	Masters degree - *Physics* Isfahan University of Technology
2008 - 2015	Bachelors degree - *Physics* Shahrekord University

---

International experience

Maarten Kamermans's group, Amsterdam, Netherlands. 1th April - 1th May 2018

- Project: Oscillations in AII amacrine cells
- Summary: I extracted the model in the paper 'Intrinsic bursting of AII amacrine cells underlies oscillations in the rd1 mouse retina' and reproduced the figures. I will continue working in this project as soon as reciving new data from the group.

Thomas Euler's group, Tuebingen, Germany. 15th August - 15th September 2018
- Project: Visual receptive field in retinal ganglion cells
- Summary: I made a biophysical model for visual receptive fields worked theoretically well using real 3D morphology of a bipolar cell but as the morphology of ganlion cells were not available, we could not test it on gaanglion cells. I will continue this project as soon as I could find real morphology of mice ganglion cells.

Guenther Zeck's group, Tuebingen, Germany. 15th July - 15th August 2018
- Project: Simulation of extracellular potential from retinal bipolar cells
- Summary: As I was involved in preparing my Plos One paper, I could not do a big project while visiting. I just did a rudimentary simulation on recording extracellular potential of retinal bipolar cells.

Scholarships and funding

Marie Sklodowska-Curie fellowship for Ph.D, 2016-2019

Iranian national scholarship for master, 2012-2015

Iranian national scholarship for bachelor, 2008-2012

Supervision of master students

Marjam Mahmoudi

Isfahan University of Technology
Thesis title: Effect of geometry of soma on neuron computations
2019-present

Maria Bordeus
Vienna University of Technology
Thesis title: A computational model of the ribbon synapse of bipolar retinal cells
2016 – 2017

Sogand Sajedi
Vienna University of Technology
Thesis title: Intra- and extracellular stimulation of spiking bipolar cells on macaque's retina
2017 – 2018

Papers in peer-reviewed journals

H. Bassereh, F. Rattay.
'Two models for vesicle release from a ribbon synapse of electrically stimulated retinal bipolar cells'
Submitted.

F. Rattay, H. Bassereh, I. Burian.
'Compartment models for the electrical stimulation of retinal bipolar cells'
PLoS ONE 13(12): e0209123, 2018.

A. Jalalinejad, H. Bassereh, V. Salari,T. Ala-Nissila, A. Giacometti.
'Excitation Energy Transport with Noise and Disorder in a Harmonic Toy Model of Single Strand in the Selectivity Filter Backbone of an Ion Channel'
Journal of Physics: Condensed Matter 30 (41), 415101, 2018.

F. Rattay, H. Bassereh, A. Fellner.
'Impact of Electrode Position on the Elicitation of Sodium Spikes in Retinal Bipolar Cells'

Scientific Reports 7 (17590), 2017.

H. Bassereh,V. Salari, F. Shahbazi, T. Ala-Nissila.
'Perfect quantum excitation energy transport via single edge perturbation in a complete network'
The European Physical Journal B 90 (6), 111, 2017.

H. Bassereh, V. Salari, F. Shahbazi.
'Noise Assisted Excitation Energy Transfer in a Linear Toy Model of a Selectivity Filter Backbone Strand'
Journal of Physics: Condensed Matter 27 275102, 2015.

V. Salari, M. Sajadi, H. Bassereh, V. Rezania, M. Alaei, J.A. Tuszynski.
'On the classical vibrational coherence of carbonyl groups in the selectivity filter backbone of the KcsA ion channel'
Journal of integrative neuroscience 14, 195, 2015.

V. Salari, H. Valian, H. Bassereh, I. Bokkon, A. Barkhordari.
'Ultraweak Photon Emission in the Brain'
Journal of integrative neuroscience 14, 419, 2015.

Papers in conference proceedings

H. Bassereh, F. Rattay.
11th international meeting on substrate-integrated microelectrode arrays, July 4 – 6, 2018, Reutlingen, Germany.
'Effect of Extracellular Stimulation on Neurotransmitter Release in a Ribbon Synapse'
doi:10.3389/conf.fncel.2018.38.00021.

H. Bassereh, F. Rattay.
MATHMOD 2018 Extended Abstract Volume, 9th Vienna Conference on Mathematical Modelling, Vienna, Austria, February 21-23,

2018.
'Neurotransmitter Release from a Retinal Ribbon Synapse, a Modelling Study'
doi:10.11128/arep.55.a55256

Conference contributions / poster presentations

H. Bassereh, F. Rattay.
3th switchBoard annual meeting, September 20, 2018, Zuerich , Switzerland.
'Synaptic Exocytosis of Bipolar Cells; an ODE approach'

H. Bassereh, F. Rattay.
9th vienna international conference on mathematical modelling, February 21 – 23, 2018, Vienna, Austria.
'Neurotransmitter Release from a Retinal Ribbon Synapse, a Modeling Study'

H. Bassereh, F. Rattay.
2th switchBoard annual meeting, November 7, 2017, Bergen , Norway.
'Impact of Electrode Position on the Elicitation of Sodium Spikes in Retinal Bipolar Cells'

H. Bassereh, F. Rattay.
Vienna young science symposium, June 1 – 2, 2017, Vienna, Austria.
'Intra- and Extracellular Stimulation of Retinal Bipolar Cells'

H. Bassereh, P. Werginz, F. Rattay.
1th switchBoard annual meeting, October 7, 2016, Tuebingen, Germany.
'Simulation of the Synaptic Exocytosis of Bipolar Cells in the Electrically Stimulated Retina'

H. Bassereh, V. Salari, F. Shahbazi.
Hands on research in complex systems, *ICTP*,June 29 – July 10, 2015, Trieste, Italy.
'Effect of Disorder and Noise on Excitation Energy Transfer in Quantum Complex Networks'

H. Bassereh, V. Salari, F. Shahbazi.
4-th iran computational neuroscience workshop, August 26 – 29, 2014, Zanjan- Iran, IASBS.
'On the Possibility of Quantum Effects in KcsA Ion Channels'

Teaching

Basic Physics I and II Lab
Isfahan University of Technology
Sessional Lecturer
2012 – 2015